On the Nature and Behavior of Filaments in the Dielectric Barrier Discharge of Plasma Actuators

Über die Eigenschaften und das Verhalten von Filamenten in der dielektrischen Barriereentladung von Plasma-Aktuatoren

Master-Thesis of Sebastian Bürkle, B.Sc., B.Sc.

Mai 2013

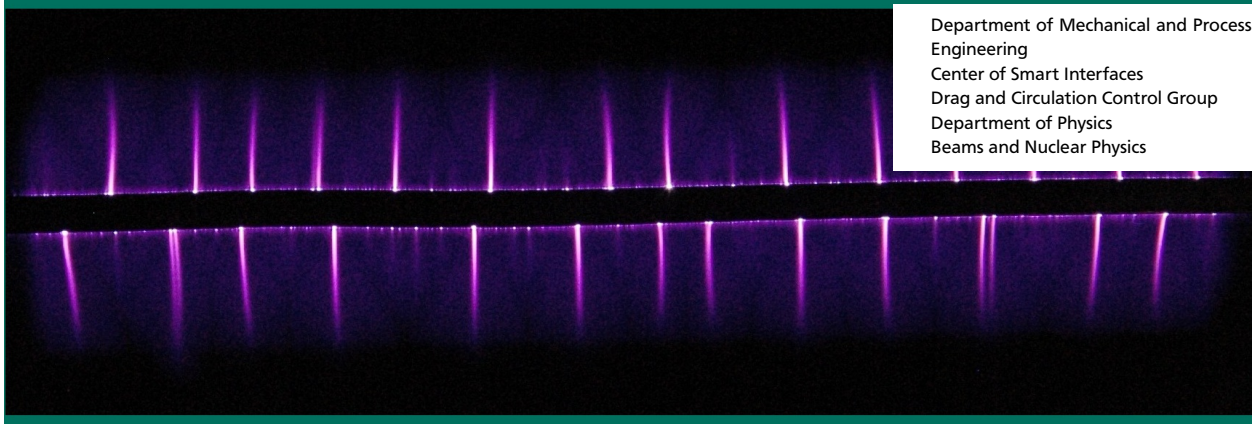

TECHNISCHE UNIVERSITÄT DARMSTADT

Department of Mechanical and Process Engineering
Center of Smart Interfaces
Drag and Circulation Control Group
Department of Physics
Beams and Nuclear Physics

Prof. Dr. Dr. h.c./RUS Dieter H.H. Hoffmann

Center of Smart Interfaces

On the Nature and Behavior of Filaments in the Dielectric Barrier Discharge of Plasma Actuators
Über die Eigenschaften und das Verhalten von Filamenten in der dielektrischen Barriereentladung von Plasma-Aktuatoren

Vorgelegte Master-Thesis von Sebastian Bürkle, B.Sc., B.Sc.

1. Gutachten: Prof. Dr. Dr. h.c./RUS Dieter H.H. Hoffmann
2. Gutachten: Dr. Serban Udrea

Tag der Einreichung:

Erklärung zur Master-Thesis

Hiermit versichere ich, die vorliegende Master-Thesis ohne Hilfe Dritter nur mit den angegebenen Quellen und Hilfsmitteln angefertigt zu haben. Alle Stellen, die aus Quellen entnommen wurden, sind als solche kenntlich gemacht. Diese Arbeit hat in gleicher oder ähnlicher Form noch keiner Prüfungsbehörde vorgelegen.

Darmstadt, den May 21, 2013

(Sebastian Bürkle)

Abstract

Plasma actuators based on dielectric barrier discharge (DBD) promise a bright future in aerodynamical applications. By creating a body force in the surrounding gas through plasma – gas interaction, plasma actuators operated in quiescent air induce a small flow above their surface with a velocity of typically 5-8 m/s, the so called *ionic wind*. The ionic wind can influence the boundary-layer of an externally applied flow surrounding the actuator. Unfortunately, the origin of the body force that lead to the ionic wind is not completely understood yet, since the physics of the underlying discharge is not clarified in detail. The aim of this master-thesis was to improve the understanding of the discharge. Particularly, the *micro-scale* as well as *large-scale filaments* observed in the discharge were studied systematically and the theory extended by the results of the performed investigations. Micro-scale filaments, i.e. discharges with a duration of a few nanoseconds, occur due to the dielectric barrier that prevents a continuous discharge and thus arcing.

In the present work, the theoretical models of the different discharge regimes that lead to micro-scale filaments have been unified. The DBD is proposed to operate in the streamer regime within the positive half-cycle and in the corona regime within the negative half-cycle of the voltage. Streak camera images of the discharge in both half-cycles are captured, supporting the models. Current measurements have been carried out with high performance oscilloscopes. The amplitude spectra of the current show, that the discharge duration is only dependent on the actuator setup and neither on the external voltage nor the half-cycle. This can be explained through the different time scales of the discharge duration and period of the external voltage. The discharge ceases as soon as the internal electric field that builts up due to the space charge of the barrier is sufficiently high to decrease the externally applied electric field to a level below break-down voltage. Since the discharge duration only depends on the surface charge necessary to decrease the field, it is dependent on the setup of the actuator only. In additional experiments it is shown that the amplitude of the discharge current, the number of discharges per half-cycle and the time from first to last discharge within a half-cycle are strongly dependent on half-cycle, voltage amplitude and frequency. It is also shown, that for high-voltage amplitudes, the mean time between two discharges has an asymptotical behavior for different voltage frequencies and half-cycles. This behavior is the same for all frequencies and both half-cycles. The same applies to the duty cycle of the current. The probability distribution of the current amplitudes shows an exponential behavior that is well explainable.

A new theoretical model of the origin and behavior of large-scale filaments is developed in the present thesis. According to this model, the filaments are thermal instabilities of the plasma that lead to a local increase in the gas temperature. The development of the instabilities can be described by a cyclic process. Experiments within this work show that the power-voltage characteristic of the discharge does not depend on the presence of filaments. This can be explained with reduced power consumption in the area between the filaments. This model is supported by images obtained with a thermo-camera. The images also confirm that the temperature in the fila-

ments is rising in accordance with the model. Measurements of the onset voltage for an unstable development under variation of the velocity of an externally applied flow have been carried out. It is shown, that the flow delays the formation of filaments. This is in good agreement with the model. Velocity measurements with a Pitot tube show an increase of the ionic wind velocity in the vicinity of the instabilities compared to the spacing between them. This effect may allow for an improvement of the flow control in future applications.

Kurzfassung

Plasma-Aktuatoren mit dielektrischer Barrierentladung verheißen eine viel versprechende Zukunft in der Aerodynamik. Durch die Erzeugung einer Volumenkraft im Gas aufgrund der Plasma-Gas Wechselwirkung können sie in ruhender Luft eine kleine Strömung von 5-8 m/s an ihrer Oberfläche erzeugen, den sogenannten ionischen Wind. Mithilfe dieses Windes lässt sich die Grenzschicht einer externen Strömung um den Aktuator beeinflussen. Allerdings konnte die Entstehung des ionischen Windes noch nicht vollständig geklärt werden, da die Physik der zugrunde liegenden Entladung noch nicht umfassend verstanden ist. Dies soll im Rahmen dieser Masterarbeit verbessert werden. Dazu sollen die *mikroskopischen* und *makroskopischen Filamente*, die in der Entladung beobachtet wurden, systematisch untersucht werden und das theoretische Modell um die daraus resultierenden Erkenntnisse erweitert werden.

In dieser Arbeit wurden theoretische Modelle zu den verschiedenen Entladungs- Regimen, die zu mikroskopischen Filamenten führen, vereinigt. Diese besagen, dass die Entladung im positiven Halbzyklus von Streamern und im negativen Halbzyklus von einer Korona-Entladung dominiert wird. Aufnahmen der Entladung in beiden Halbzyklen, die mit einer Streak Kamera durchgeführt wurden, unterstützen diese Modelle. Daneben wurden Strommessungen mithilfe von Oszilloskopen mit hoher Bandbreite durchgeführt. Die Amplituden-Spektren dieser Messungen zeigten, dass die Entladungsdauer nur vom Aufbau des Aktuators, nicht aber von der Betriebsspannung oder dem Halbzyklus abhängen. Dies konnte durch die unterschiedlichen Zeitskalen der Entladungsdauer und der Periode der Betriebsspannung erklärt werden. Die Entladung endet, sobald das elektrische Feld, das von der Oberflächenladung der Barriere aufgebaut wird, das elektrische Feld der Betriebsspannung unter die Durchbruchsspannung senkt. Da die Entladungsdauer nur von der zur Reduktion des elektrischen Feldes notwendigen Oberflächenladung abhängt, ist sie nur vom Aufbau des Aktuators abhängig. Weitere Experimente zeigen, dass die Amplitude des Stromes während der Entladung, die Anzahl der Entladungen pro Halbzyklus und die Zeit von erster bis letzter Entladung in einem Halbzyklus stark von der Amplitude und Frequenz der Spannung und vom Halbzyklus abhängen. Ausserdem konnte gezeigt werden, dass sowohl die durchschnittliche Zeit zwischen zwei Entladungen als auch der relative Betriebszyklus mit Entladungen für hohe Spannungen auf eine für alle Spannungsfrequenzen und beide Halbzyklen gemeinsame Asymptote zugehen.

Daneben wird in der vorliegenden Arbeit ein neues Modell zur Entstehung und den Eigenschaften der makroskopischen Filamente in der Entladung entwickelt. Die Theorie geht davon aus, dass es sich bei den Filamenten um thermische Instabilitäten im Plasma handelt, die zu einem lokalen Anwachsen der Temperatur führen. Anhand eines Prozess-Zyklus werden die einzelnen Schritte

der instabilen Schritte aufgezeigt. Davon ausgehend wird ein Kriterium für die Entstehungsbedingungen für die Entstehung eines instabilen Prozesses berechnet. Die Experimente dieser Arbeit zeigen die Unabhängigkeit des Leistungsverbrauchs der Plasma Aktuatoren vom Auftreten der Instabilitäten. Dies lässt sich durch einen reduzierten Leistungsverbrauch im Gebiet zwischen den Filamenten erklären, was durch Aufnahmen mithilfe einer Thermokamera bestätigt wird. Die Bilder zeigen außerdem ein Anwachsen der Temperatur in den Filamenten, was im Einklang mit dem Modell ist. In der Arbeit wird zudem auch die Abhängigkeit der Mindestspannung für eine instabile Entwicklung von der Geschwindigkeit eines externen Windes am Aktuator untersucht. Es lässt sich zeigen, dass die Strömung eine instabile Entwicklung verzögert. Dies ist in guter Übereinstimmung mit dem Modell. Geschwindigkeitsmessungen des ionischen Windes mithilfe eines Pitotrohrs zeigten eine erhöhte Geschwindigkeit in der Umgebung der Instabilitäten verglichen mit dem Bereich dazwischen. Dieser Effekt lässt sich zukünftig eventuell für eine verbesserte Strömungskontrolle nutzen.

TECHNISCHE UNIVERSITÄT DARMSTADT

Center of Smart Interfaces

On the Nature and Behavior of Filaments in the Dielectric Barrier Discharge of Plasma Actuators

Über die Eigenschaften und das Verhalten von Filamenten in dielektrischer Barriereentladung von Plasma - Aktuatoren

for Sebastian Bürkle, B. Sc. B. Sc.
degree program M.Sc. Physics
Supervisors: Prof. Dr. Dr. h.c./RUSS D. H.H. Hoffmann
Dr. Serban Udrea

September, 6th 2012

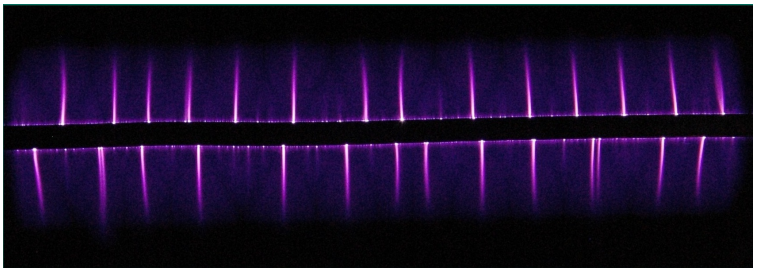

Large-Scale Filaments in an DBD plasma actuator

Objectives:

In recent years, plasma actuators have become a promising device for aerodynamic flow control applications. The ionic wind induced by the plasma actuator is used to influence the boundary layer of the flow. The Dielectric Barrier Discharge (DBD), that induces the ionic wind of plasma actuators, is not completely understood yet. Further understanding of the discharge is crucial for a better comprehension of the ionic wind as well as for optimization of the actuator.
Preliminary studies showed that the glow discharge is composed out of micro-scale filaments with a repetition-period of a few microseconds and a width of a few hundred micrometer. The first objective of the work is to study these filaments experimentally.

Within the glow discharge, large-scale filaments of large lifetime and a width of several millimeter can occur. Since these filaments seriously damage the dielectric barrier through electro erosion, a further understanding and a theory on their nature and behavior is necessary. Accord-

ingly, the second objective of the thesis is to study the large-scale filaments experimentally. Based on these studies, the third objective is to develop a new theory of the filaments.

Work plan and experiments:
The following table describes all objectives and experiments planned in order to achieve them.

Field of study	Objective	Technique
Micro-scale filaments	spatial structure of discharge	Streak camera
		Voltage parameters variation (quiescent air)
		Variation of the environmental parameters (TVM150)
	Temporal structure	Current measurements with oscilloscope
		Voltage parameters variation (quiescent air)
Large-scale filaments	Development of a new theory	Literature
	Experiments of onset conditions	Measurements on voltage, flow velocity and temperature
	Power consumption dependency	Charge measurements with oscilloscope
	Heat generation of filaments	Infrared camera
	Ionic wind velocity	Pitot tube

Darmstadt, September, 6th, 2012

Prof. Dr. Dr. h.c./RUSS D. H.H. Hoffmann

Contents

List of Figures

List of Tables

Nomenclature

α	Degree of ionization
λ_D	Debye length
T_i	Ion temperature
T_e	Electron temperature
T_e	Gas temperature
n_e	Number density of electrons
n_i	Number density of ions
n_n	Number density of neutrals
μ_e	Electron mobility
μ_i	Ion mobility
ν_e	Collision frequency of electrons with neutrals
ν_i	Collision frequency of ions with neutrals
$\tilde{\nu}_i$	Ionization frequency
γ_i	Secondary electron emission coefficient
α_i	Ionization coefficient
E_{ext}	External electric field in the plasma actuator
E_{sc}	Electric field built up by space charge
N_{crit}	Critical number of ions or electrons to create an electric field that exceeds the external field
E/N	Reduced electric field
ν_h	Frequency of heating
ν^*	Logarithmic sensitivity

1 Introduction

1.1 Motivation

A high voltage between two electrodes can partially ionize a surrounding gas and form a domain of thin non-thermal plasma. The displacement of the charged particles in the plasma by the electric field can produce a net body force due to momentum transfer between the charged particles and surrounding neutral molecules and atoms. Depending on the arrangement of the electrodes, the body force can produce a local flow, the so called *electric* or *ionic wind*. Since the ionic wind is a direct conversion of electric to kinetic energy, it is of special interest for aerodynamic research, especially in flow control.

The investigation of ionic wind in such applications has a long tradition. The electrode arrangement that had been most widely studied in the past is the so called *volume discharge*, where a DC high voltage is applied between a needle and a grounded object, like a plate, a wire or a bulk body. The voltage on the needle can either be positive or negative, to form a negative or positive glow plasma, depending on the desired effects and shape of the discharge zone. Fomin et al. [1], for instance, studied the influence of a longitudinal glow discharge on the supersonic flow around a bulk cone. They reported that the ionic wind can clearly modify the sonic shock system formed around the cone.

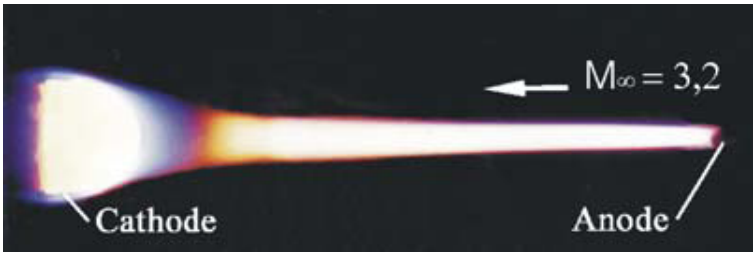

Figure 1.1: Visual appearance of a discharge [1]

The DC volume glow discharge has several disadvantages that limit its usage in aerodynamic flow control, especially in flow control of external flows: First of all, the power of those actuators is limited due to arcing. The higher the gas pressure, the more easily the plasma becomes unstable and an arc is forming. Secondly, the ionic wind in quiescent air as well as in an external flow is three-dimensional and is difficult to predict. Most importantly, the high-voltage needle is a unavoidable disturbance in the flow.

J. R. Roth [2] in 1997 first studied the influence of the ionic wind of a *Dieletric Barrier Discharge* (DBD) plasma actuator in an aerodynamic application, specifically boundary layer control (Roth called it "“one atmosphere uniform glow discharge surface plasma", OAUGDSP). In contrast to an DC volume discharge plasma, the DBD plasma is an AC *surface discharge* plasma.

(a) (b)

Figure 1.2: High speed flow control experiment with a volume DC glow discharge operated in a M_∞=3.2 air flow from Fomin et al. [1]. Images are Schlieren visualizations of the flow with (a) the discharge off and (b) the discharge on.

The arrangement of the electrodes in a DBD plasma actuator is quite different from the DC volume discharge, but not new. It has been widely used in ozone generation applications before, as in Kogelschatz *et al.* [4].
The actuator consists of two electrodes, separated by a dielectric barrier that prevents the actuator from arcing. One electrode, the *lower electrode*, is grounded and encapsulated by the dielectric material (Kapton, Al_2O_3 etc.). The other electrode, usually called *exposed* or *upper electrode*, is exposed to a surrounding gas. A high AC voltage of sinusoidal, square, saw tooth or triangle wave type is applied to this electrode.

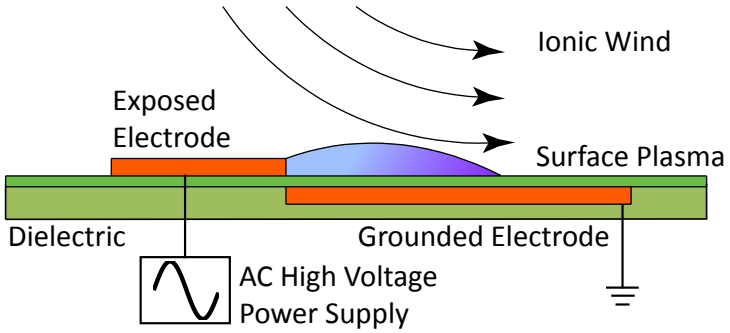

Figure 1.3: Design of a typical DBD plasma actuator

The electric field generates a discharge above the dielectric barrier resulting in a plasma. The ionic wind of this plasma creates a wall jet sheet along the exposed electrode with a momentum flow from the upper to the lower electrode and a velocity of typically 5-8 m/s. As Roth showed in [3], the wall jet can be used for flow control applications, such as separation control, by influencing the boundary layer of the flow around the actuator.

The advantages of DBD plasma actuators in flow control applications compared to DC volume discharge actuators are:

- no mechanical parts in the flow, thus less disturbances

(a) (b)

Figure 1.4: Low-speed separation control on a wing profile with a DBD plasma actuator operated in an external airflow, according to Roth [3]. Image (a) shows the flow with the plasma actuator off and (b) with plasma actuator on. Without an actuator the flow separates from the wing and a recirculation zone occurs.

- higher possible input of electrical power into the flow, due to the dielectric barrier that prevents the plasma from arcing
- the induced flow is two-dimensional
- the discharge can create a wall jet for boundary layer control

It is expected that DBD plasma actuators can improve the performance (higher angles of attack) [3], reduce the broadband noise [5] and minimize the consumption (suppression of laminar-turbulence transition) [6] of future aircrafts.
Unfortunately, the occurrence of the body force that leads to the ionic wind is still not completely understood, since the physics of the underlying discharge is not clarified in detail. The understanding of the underlying physics is essential for the characterization of the performance and behavior of a DBD plasma actuator. This is also necessary for understanding the influence of different electric parameters, like voltage amplitude, frequency and gradients as well as environmental conditions, such as pressure, temperature and flow speed, on the performance.

1.2 Aim of this work

Recent papers, Pavon *et al.* [15], Benard *et al.* [16] and Korolev *et al.* [18], as well as preliminary studies show that the discharge is made out of filaments, more precisely, out of two different kinds of filaments, micro-scale and large-scale. The discharge, occurring as a steadily glowing zone to the unaided eye, consists in fact out of multiple discharge filaments, with a repetition period of some microseconds, a duration of a few nanoseconds and a width of several hundred micrometers. Within this steadily glowing zone, large-scale filaments can occur, depending on the applied voltage. The filaments are visible even to the unaided eye and have a width of about one millimeter and a length of a few millimeters. These filaments vanish only when the voltage is turned off. Since these two types have different properties and scales, they are likely to be independent of each other. Nevertheless, they are often confused with each other in literature and thus need to be studied systematically.

The first objective of this work is to investigate the micro-scale filaments involved in the discharge, their dependence on electric and environmental parameters and to improve the theory where necessary. With the help of this knowledge it should be possible to find optimization strategies for the actuators as well as fully understand the formation of the ionic wind in future works.
The second objective is to study the large-scale filaments, their dependency on power consumption and flow velocity and consequently develop a theoretical model on their formation. This is necessary, since no model of the large-scale filaments exists in literature. These filaments seem to seriously damage the plasma actuators through electro erosion of the dielectric barrier. Thus, a strategy for their prevention needs to be found as well.

2 Theory of discharge filaments

The next sections describe the theoretical models of the filaments in the discharge of a DBD plasma actuator. The first section gives an overview of the present knowledge of the physical background of plasmas produced by gas discharges. In the second section, the discharge regimes occurring within a plasma actuator as micro-scale filaments are discussed, namely the *corona* and *streamer* discharge. In the last section of chapter two, the newly developed theoretical model of large-scale filaments is described.

2.1 Physical background

In physics and chemistry, a plasma describes a mixture of partly or fully ionized atoms or molecules and electrons. The plasma state is commonly known as the fourth state of matter.
Plasmas span a wide range of temperatures and densities of charged particles with different physical and chemical properties and regimes. Thus plasmas can be found in various experiments, industrial applications and are subjects to a wide range of research projects. In order to provide a better insight into the discharges in DBD plasma actuators, a further distinction and classification of the DBD plasma is necessary and will be done in the next subsection.
In the following subsection the DC volume discharge will be explained, since, in contrast to the DBD surface discharges, many of the effects that occur in DC volume discharges are already fully understood and described in literature. The effects are similar to the ones occurring in dielectric barrier discharges.

2.1.1 Classification of the dielectric barrier discharge plasmas

At macroscopic scales, the concentrations of negative and positive charges in a plasma are approximately equal, thus the plasma is quasi-neutral. At microscopic scales, this is not necessarily the case. Space charges can form up, for example due to newly injected ions or electrons, externally applied electric or magnetic fields, or compression waves. The space charges attract either electrons or ions, since the plasma itself consists out of charges. Thus the space charge is compensated by the plasma macroscopically, and its electric field is shielded. According to [7] the potential of the space charge can be described as

$$\Phi(\mathbf{r}) = \frac{q}{r} e^{(-r/\lambda_D)} \tag{2.1}$$

i.e. the potential decays exponentially for distances greater than λ_D. λ_D is the *Debye-length*, that defines the spatial range of the plasma, which can comprise a charge imbalance and characterizes

the thickness of the sheath formed by the plasma around electrodes or walls. It is given by

$$\lambda_D = \sqrt{\frac{kT}{4\pi n_e e^2}} \tag{2.2}$$

with T the plasma temperature (or electron temperature in non-equilibrium plasmas) and n_e the electron density. For non-thermal plasmas, the Debye length ranges from 10^{-4} m to a few cm.

The DBD plasma is a non-equilibrium plasma, the ion temperature is significantly different from the electron temperature. The electron temperature, on one hand, ranges from one to ten eV, where inelastic collision are relevant. The temperature of the ions, on the other hand, is in in the order of the gas temperature and thus in the order of the ambient temperature, $T_i \approx T_g \approx 300$K. The charge number density n defines the number of charges per volume and ranges from 10^5 to 10^{13} cm^{-3}, according to [8]

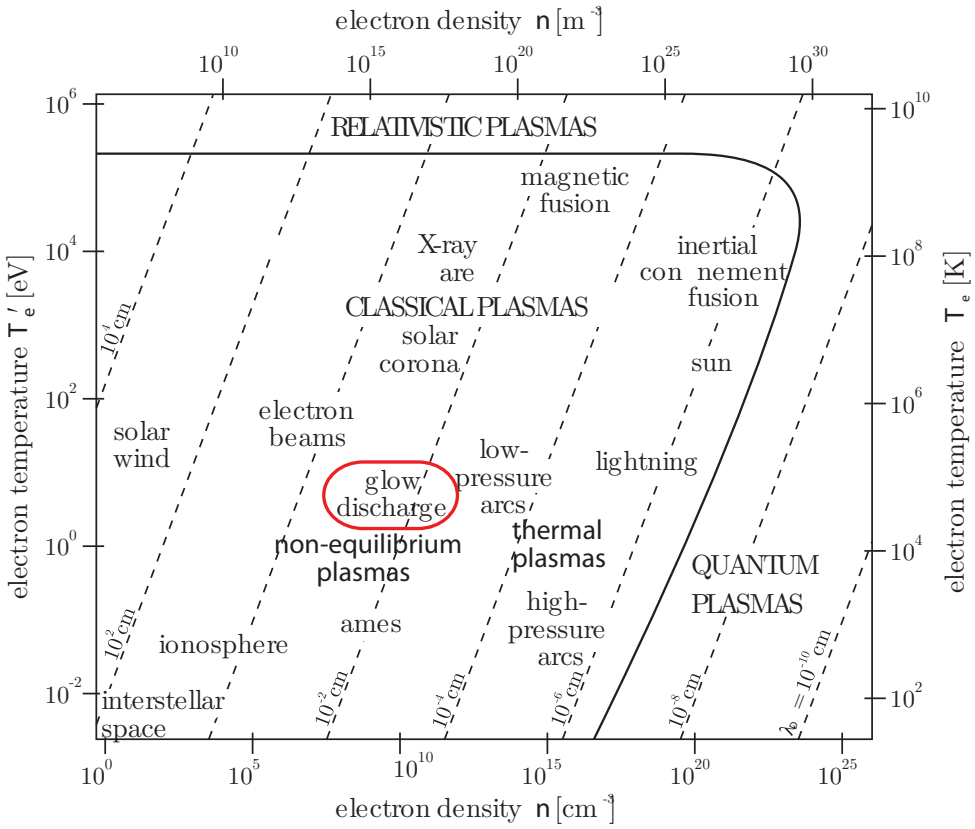

Figure 2.1: Two-dimensional classification of the glow plasma in comparison to others, characterized by electron number density n and electron temperature T_e, analog to Kriegseis [8].

Another parameter of interest in plasmas is the degree of ionization

$$\alpha = \frac{n_i}{n_i + n_n} \tag{2.3}$$

Since a surface DBD plasma is has a very low degree of ionization (α=10^{-4}...10^{-3}«1) it can be assumed that the momentum transfer mainly occurs between charged and neutral particles and

that momentum transfer between charged particles can be neglected. The mass of the electrons is significantly less than that of ions and neutrals, thus the contribution of electrons to ionic wind can be neglected.
The charged particles drift along the direction of the electric field $\vec{E}$. In the drift movement, the charges are accelerated due to the electric field, superimposed with a random movement due to the collisions with neutrals [9]. The momentum transfer in the collisions slows the particles down. Thus the particles, on average, have a limited velocity $\vec{v}$ given by the strength of the electric field and their mobility μ

$$\mu_{e,i} = \frac{Ze}{m_{e,i}\nu_{e,i}} \tag{2.4}$$

with the charge number Z and ν, the collision frequency of charges with gas particles. Since the plasma is very thin, double ionization can be assumed to be nigligible and thus Z is unity. For this reason it is usually left out in literature. The average drift velocity is then

$$\vec{v}_{e,i} = \begin{cases} \mu_i \vec{E} & \text{for positively charged ions} \\ -\mu_{i,e}\vec{E}, & \text{for electrons and negatively charged ions} \end{cases} \tag{2.5}$$

The kinetic energy of the ions is transferred to the neutral molecules during the collision and is responsible for the ionic wind.
The mass m_e of electrons is significantly smaller than the mass of ions and neutral molecules ($m_e/m_p = 1836$ for ionic hydrogen, mass ratios of 10^4 are typical for gas or ions). Thus collisions of electrons with neutrals produce almost no momentum transfer. The mass of the ions, m_i, on the other hand, is in the order of the mass of the neutrals. Large amount of momentum can be transferred from the ions to the neutrals through elastic collision. Thus the ion movement is the main reason of the ionic wind. Since the ions loose most of their kinetic energy hereby, their temperature is in the order of the neutral gas temperature.
Since the mass m_e of electrons is significantly smaller than the mass of ions, the mobility and thus the average velocity of electrons are much higher than that of ions. This fact will be of interest in the next subsection.

2.1.2 Electrical breakdown in DC volume gas discharges

The physical arrangement of a DC volume discharge is quite different from a surface dielectric barrier discharge, since there is no barrier to limit the discharge, the actuator design is usually symmetric and the applied voltage signal is DC instead of radio frequency AC. Nevertheless, the volume discharge is an adequate simplification for some effects in a single dielectric barrier surface discharge. For this reason we will discuss its major aspects in this and the following subsection.

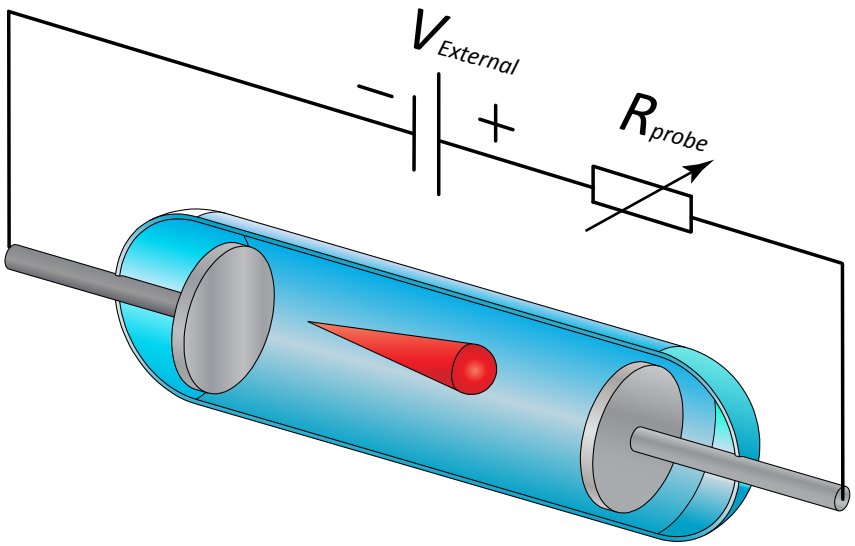

Figure 2.2: Principle of a drift tube with Townsend- (avalanche-) discharge

A very simple way to create a DC volume discharge is a *drift tube*, consisting out of a low pressure gas and a high voltage between two conducting plates. Inside the gap, free electrons are produced due to background ionization. For small voltages, the electrons in the gas drift from the cathode to the anode as described in chap. 2.1.1. The movement can be detected by a small current at the electrodes. At very low voltage, not all electrons reach the anode before they recombine with ions. Thus the current is dependent on the applied voltage. As the voltage is increased, the velocity rises until all electrons reach the anode before recombination. From this point on the drift current is independent of the applied voltage.

Paschen [10] in 1889 first described a breakdown of this independency in various gases. As he increased the voltage further, he observed a rise of current in the drift tube at significantly higher voltages. This increase results from the production of secondary electrons due to electron detachment. Since the mass m_e of electrons is significantly smaller than the mass of ions, the mobility and thus the average velocity of electrons is much higher than that of ions. Due to the fact that the masses of bound and free electrons are equal, large amounts of momentum can be transfered through inelastic collision. When the kinetic energy of the free electrons is in the order of the ionization energy of the gas molecules, they detach electrons from the gas molecules. These knocked-out electrons are accelerated towards the anode in the external electric field and in-

crease the current. This leads to an exponentially increasing number of electrons, called *avalanche* or *Townsend discharge*. The current in the Townsend discharge also raises exponentially when the applied voltage is increased. Each electron from the background ionization induces an electron avalanche with the total charge increasing on the path towards the anode. This fact can be described by

$$n_e(x) = n_0 \exp(\alpha_i x) \tag{2.6}$$

with α_i being the *ionization coefficient*, i.e. the rate of ionization frequency to drift velocity $\alpha = \tilde{\nu}_i / v_d$, and x the distance from the onset of discharge.
Despite this rise in current with increasing voltage, the discharge is not self-sustaining, since there needs to be a free electron of the background ionization to start the avalanche.

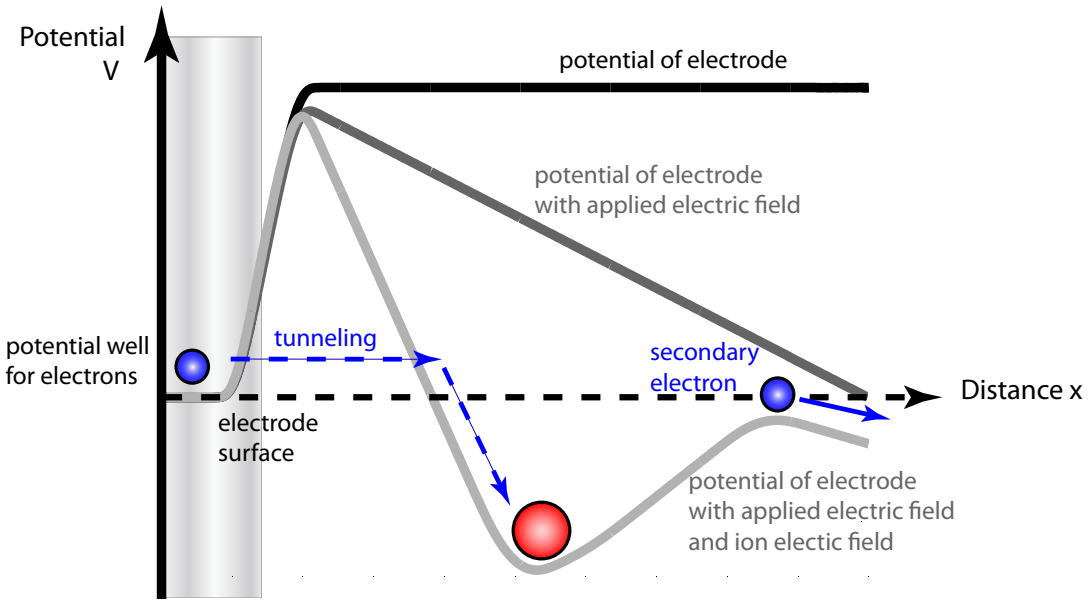

Figure 2.3: Mechanism of secondary electron emission from the surface: The external electric field and the electric field of the ion change the potential well of the electrode surface. Electrons can tunnel through the developing potential barrier and neutralize the positively charged ion. The energy released hereby can be spend on the ejection of a valence electron from the ion.

A self-sustaining discharge can be established at higher voltages by the *secondary electron emission* of ions: the ions that drift towards the cathode change the potential well on the surface within a width of the order of a few nanometer into a potential barrier. Since the potential barrier is low and narrow, electrons can tunnel from the electrode towards the ion and neutralize it. When the energy released hereby is high enough, it can be spent on the ejection of another electron, according to Penning [11]. The *secondary electron emission coefficient* γ_i describes the number of secondary electrons emitted per incident of a positive ion.

At a certain voltage the production of ions from the avalanche is high enough to maintain a self-sustaining discharge, since these ions eject enough initial electrons from the surface for new

avalanches. The self-sustainment of the discharge results in a sharp rise in current for the given voltage. Paschen showed that the voltage V_b, necessary for this breakdown, is depended on the factor pd, the product of gas pressure and gap width. He measured this dependency for various gases. The measurements yield the so called *Paschen curve* in Fig. 2.4.

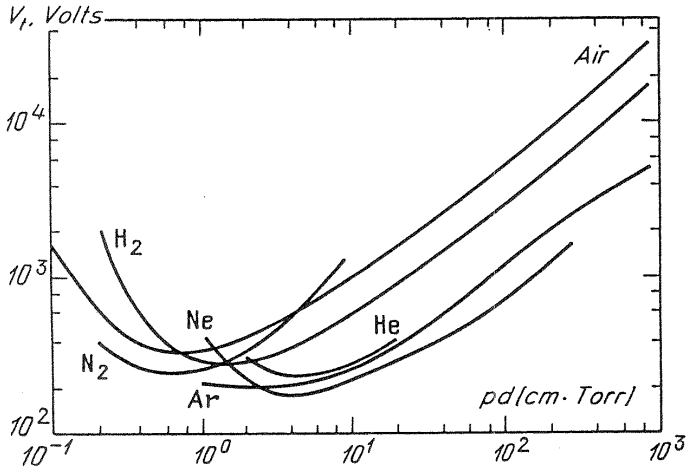

Figure 2.4: Breakdown voltages in various gases over a wide range of pd values, from [9]

2.1.3 Current-voltage characteristics in volume gas discharges

The power supply of the drift tube can be idealized by $u + i\Omega = \Pi$ =constant for a given power level, i.e. a straight line in current-voltage diagram. The intersection of this line with the nonlinear voltage-current characteristics of the drift tube gives the operating point of the system.
The characteristics of a drift tube are complex, since many different types of discharges can occur. We will discuss these different discharge regimes in this section, following Roth [12].

Background ionization regime: As described in subsection 2.1.2, very low voltages lead to a drift of the electrons produced by background radiation and a nonlinear rise in the current (A-B). The current is in the *saturation regime* (B-C) once all charges reach the electrodes before recombination.

Townsend regime: (C-E) Once the kinetic energy of the primary electrons is sufficient for secondary electrons knock-out, avalanches (Townsend discharges) occur and an exponential increase in current can be observed, as described in section 2.1.2.
Depending on the design of the electrodes, the avalanches concentrate around areas of higher electric field strength, such as sharp edges or tips in the electrodes. In this *corona discharge regime* (D-E), a sub regime of the Townsend discharge, most of the avalanches concentrate in a disruptive area around the tips, since the voltage is not sufficient for neutralization of ions by secondary electron emission. The ions create a large space charge, shielding most of the electrode. Thus the electric field in between the electrode and the space charge is enhanced, whereas it is significantly reduced in between the space charge and the second electrode. The result is a small visible area of discharges in the area of high gradients, either around the anode (positive corona) or the cathode (negative corona). This regime is the first one that emits visible light. The discharge area is fol-

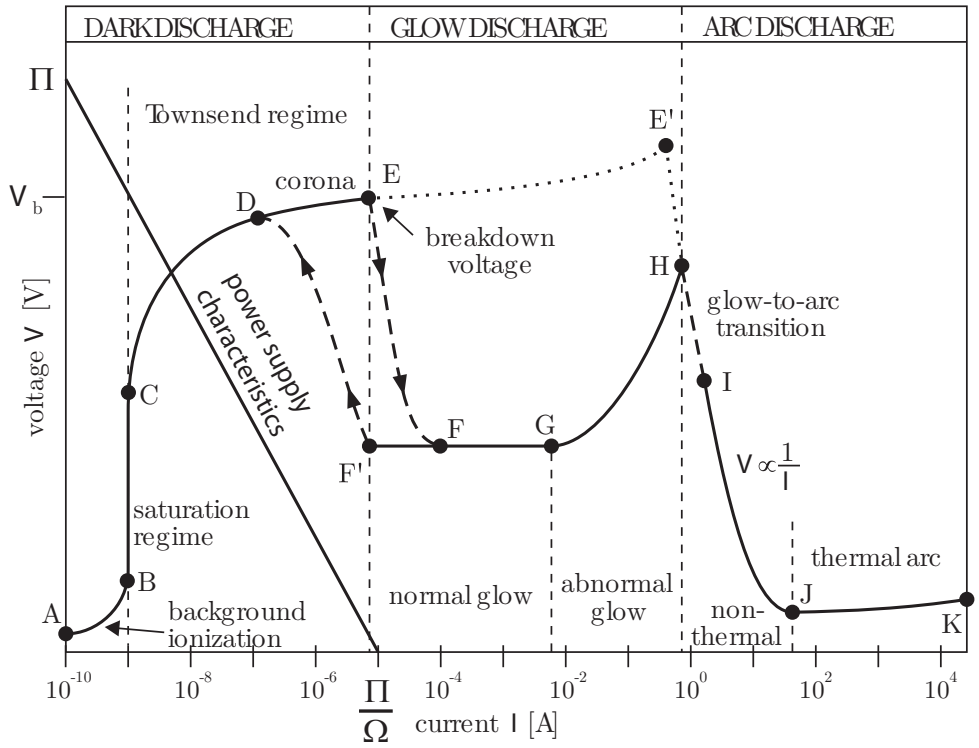

Figure 2.5: Drift tube and power supply characteristic voltage-current curve, according to [8] and [9]

lowed by a large drift zone, where either positive (positive corona) or negative (negative corona) ions slowly move towards the second electrode.

Once the voltage for secondary electron emission is reached, the discharge is self-sustaining. Thus a breakdown in voltage and a transition (E-F) to the *glow discharge regime* occurs. In this regime the current is significantly increased over several orders of magnitude. The plasma becomes visible due to the high current, and starts to cover the cathode until the latter is fully covered at point G. The *abnormal glow discharge* starts just beyond that point: Since the cathode is fully covered, a strong increase in voltage is necessary to create higher currents. Due to the high dissipated power, the plasma is very bright and the electrodes are strongly heated.

At even higher power levels (H-I) the *glow to arc transition* occurs, caused by thermionic emission of electrons from the highly heated electrodes. These extra electrons strongly decrease the voltage necessary to maintain the discharge. Due to instabilities, the plasma forms in the shape of a hot and bright arc. The plasma is first *non-thermal* (I-J), since the gas temperature is still not as high as the electron temperature. At higher power levels, the dissipated energy is high enough to heat the gas towards a *thermal arc* at point J and a thermal equilibrium at point K.

The current-voltage characteristic shows a hysteresis when the voltage is reduced from the glow regime. The system directly transits from glow to Townsend-discharge regime due to the accumu-

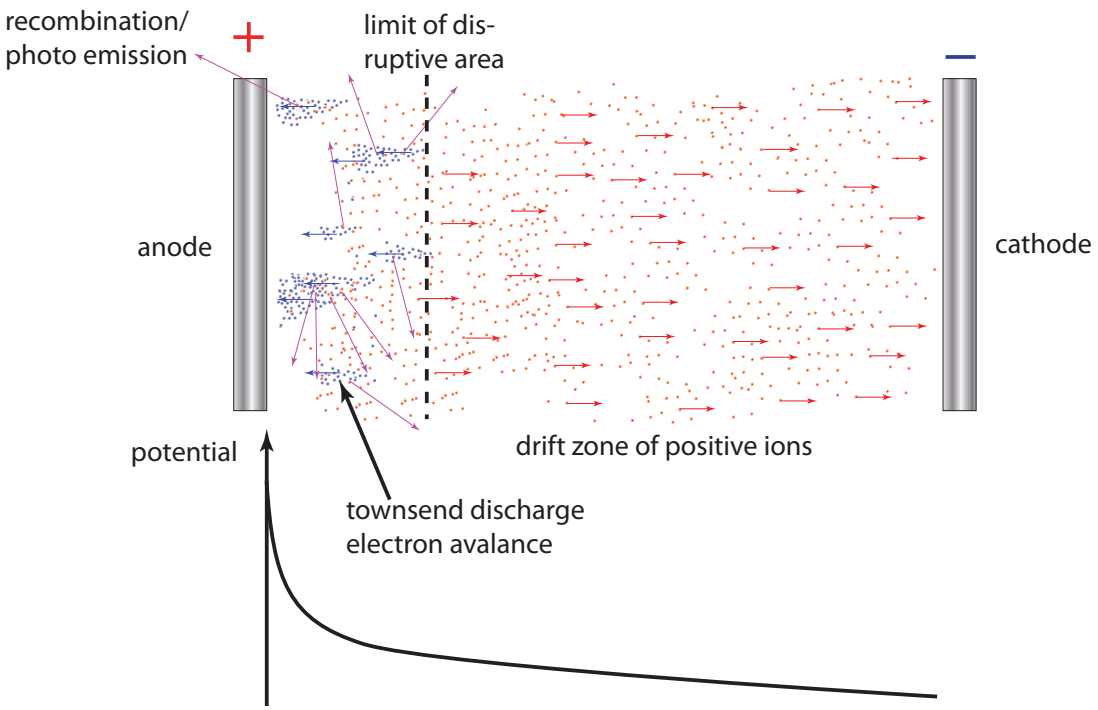

Figure 2.6: Positive corona discharge in a drift tube. Townsend-avalanches occur in the area of high voltage gradients close to the anode, leaving positively charged ions behind. The negative ions shield the anode and enhance the electric field in between. The ions slowly drift towards the cathode. When an electron and an ion inside the area of disrupted electric field recombine, photo emission occurs, leading to a visible glow of the plasma.

lation of ions and the hereby reduced breakdown voltage.

All the facts mentioned above mainly describe discharges at low gas pressures. For pressure in the order of milibar and higher, the discharge directly transits from the Townsend to the arc regime (E-E'-J), or show a streamer discharge instead of a glow discharge, according to Becker [13] and Meek [14]. It is very difficult to maintain a stable glow discharge in a drift tube under these conditions. The streamer discharge will be discussed in subsection 2.2.2.
In the next section we will discuss which of these regimes occur in a DBD Plasma Actuator under atmospheric conditions.

2.2 Theory of micro-scale filaments

As mentioned in subsection 2.1.3, it is difficult to maintain a DC plasma under atmospheric conditions without arcing. Since an arc discharge consumes high power and induces high temperatures in the gas and electrodes, it is not suitable for flow control.
Roth's [2] approach was to use a barrier surface discharge instead of a free discharge. The barrier prevents the gas discharge from arcing. The charges produced in the discharge accumulate on the surface of the dielectric barrier and built up an electric field that reduces the voltage between

exposed electrode and barrier. Thus the discharge is self-limiting when the applied voltage is DC. An increasing or decreasing voltage is necessary for maintaining a periodic discharge.
A continuously rising voltage would soon lead to infinitely high voltages, thus of no practical use. A set of alternating voltage ramps, like a saw tooth, triangle or sine wave, are more suitable. The surface charge produced by the discharge in the positive slope must be neutralized by the negative slope discharge and vice versa. Thus a AC voltage is a good way to maintain a steady plasma discharge.

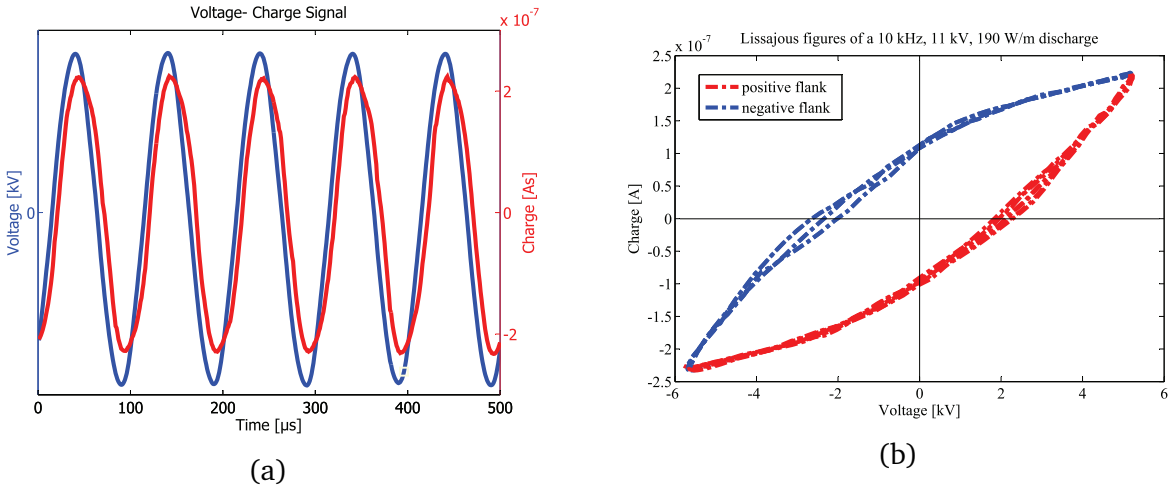

Figure 2.7: (a) Sinusoidal voltage signal, charge signal for a 10 kHz, 11 kV DB plasma discharge; (b) charge and voltage measurements plotted in a Q(t)-V(t) diagram. The trace of charge-voltage characteristics gives the corresponding so called Lissajous-figure of the discharge. The Lissajous-figure has an almond shape for surface discharges.

Kriegseis [8], who studied the charge-voltage characteristics of DB plasma discharges with the help of Lissajous-figures (see figure 2.7), found only minor differences in the discharge behavior of positive and negative slope. Thus he treated them identically. Nevertheless, there must be a significant difference in the discharge of the two slopes, otherwise no net body force would be produced. All force produced in one half-cycle of the periodic voltage would be reversed by the other half-cycle. In surface DBDs, it seems that positive and negative half-cycles have different types of discharges, but it is still not completely understood what type they are and how they work in detail.

2.2.1 Discharge regimes in a plasma actuator

As can be seen in figure 2.8, the discharge within a plasma actuator occurs only when the applied voltage increases or decreases, otherwise the potential of the surface charge built-up by the current ceases the discharge. After the voltage extremes, a dead-time without discharge follows, since there needs to be a minimal potential difference for a new, reversed breakdown, as it is the case in a Paschen-breakdown.
Wu [23] observed a transition between a continuous glow and a discontinuous, filamentary discharge at very low pressures of 6 kPa. Choi [25] confirmed Wu's experiments with the help of spectral analysis of the ions (identifying the transition point at 6.6 kPa instead of 6 kPa). At higher pressure levels the current showed large peaks followed by a period without a discharge. The discharge obviously ends after a short time and restarts after a short pause. It is thus evident, that the discharge in a DBD plasma actuator consists out of multiple single peaks for atmospheric pressures. These peaks are presumably formed out of micro-scale filaments, corresponding to current literature. According to Benard *et al.* [26], the discharge in a DBD is composed out of two different regimes, dependent on the sign of the voltage gradient applied to the actuator. For the negative half-cycle, i.e. the time from maximal to minimal voltage, Soloviev *et al.* [24] assumed the discharge to occur in a corona mode. Pavon *et al.* [15], Benard *et al.* [16] and Orlov *et al.* [17] proposed, that the discharge in the positive half-cycle, i.e. the time from minimum to maximum, is made out of streamers.

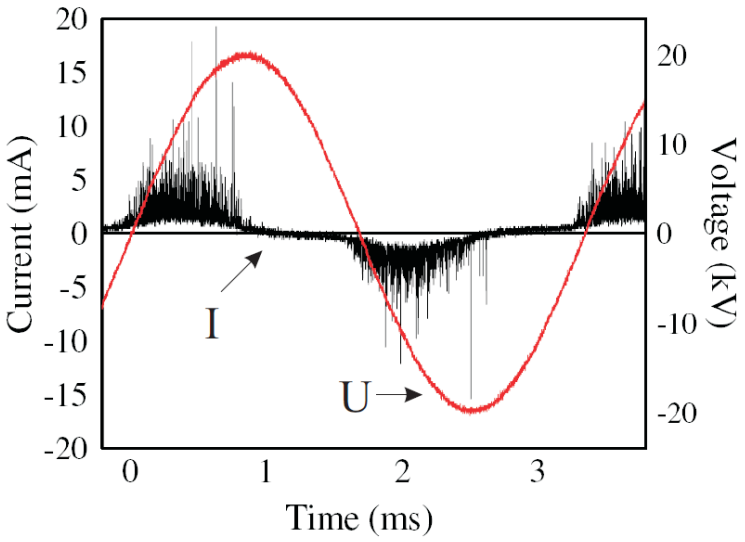

Figure 2.8: Voltage (red) and current (black) through the actuator for one discharge cycle, according to Pavon [20]. The current consists out of multiple peaks within a discharge cycle. The repetition period of these peaks is significantly less than a microsecond.

In the next subsections we will discuss the physics and properties of streamers and corona-discharge as they are described in the literature mentioned above and by Raizer [9].

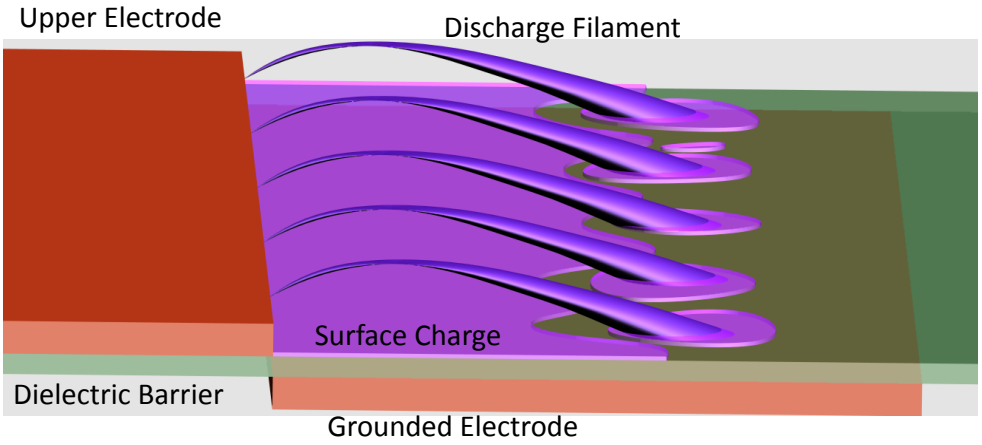

Figure 2.9: Principle sketch of a plasma actuator with micro-discharges charging the dielectric barrier surface in discharge filaments.

2.2.2 Positive micro-scale filaments

In a DC volume discharge, not only the regimes mentioned in subsection 2.1.3 can take place. Depending on the factor pd and the overvoltage $\frac{\Delta V}{V_b} = \frac{V-V_b}{V_b}$, the breakdown does not necessarily have to be of Townsend, corona or glow type, but can occur as a streamer breakdown (see fig. 2.10).

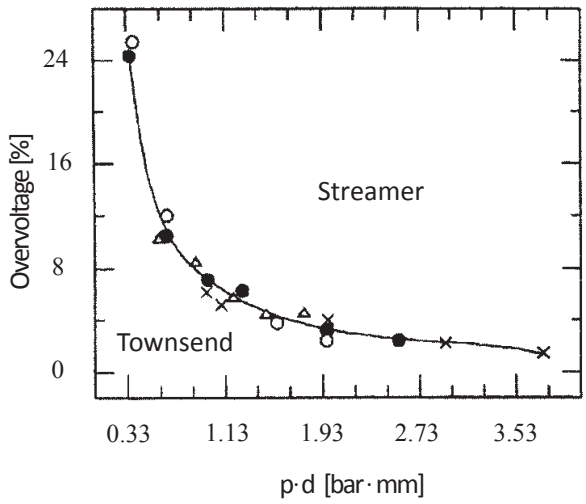

Figure 2.10: Limit between Townsend and streamer breakdown regime for DC glow discharge, according to Korolev [18].

The physics of the streamer mode is usually described in an DC volume discharge, as in Pavon [20] or Raizer [9]. It will be discussed for an AD surface discharge in this work.
During the positive half-cycle, the exposed electrode is the anode. Electrons from the background ionization are pulled towards the anode by the electric field and start an avalanche. When the electric field of the avalanche is too small to significantly distort the applied electric field before reaching the anode, the discharge remains in the Townsend regime. When the space charge ex-

ceeds a critical value, photo-ionization becomes dominant and the transition to a streamer occurs. This value corresponds to $e^{\alpha_i d} \geq N_{crit} \approx 10^{-8}$, according to Meek's criterion [14]. When the space charge exceeds that value, a steamer develops with the following steps:

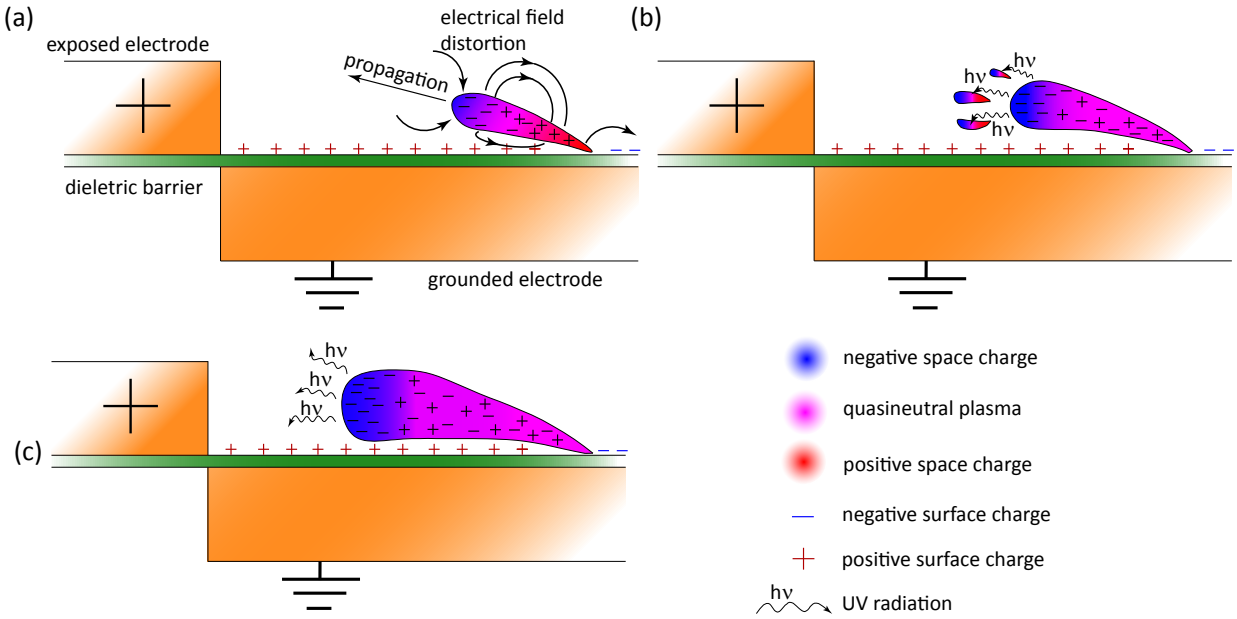

Figure 2.11: Development of anode-directed streamers. (a) initial Townsend-avalanche at t_1 (b) streamer transition through photo-ionization and creation of miniature-avalanches at $t_2 > t_1$ (c) streamer and creation of new miniature avalanches at $t_3 > t_2$

- Primary avalanche:
  A streamer first starts with an anode-directed avalanche by multiplication of primary electrons, growing rapidly from the barrier towards the anode. When the applied electric field is sufficiently strong or the discharge long enough, the space charge of the avalanche dipole – electrons at the head, ions at the tail – becomes large enough to create an electric field that is in the order of the applied electric field. The effective electric field becomes a superposition of the external and the dipole field, seriously enhancing the field between the head and the anode while reducing the field between the head and the barrier (fig. 2.11a).
  UV-radiation, emitted by the avalanche-head through recombination and relaxation of excited states, can randomly ionize the gas ahead of the discharge through photo-ionization. The knocked-out electrons lead to smaller Townsend avalanches, growing towards the anode (electrons) and towards the main-avalanche head (ions) simultaneously (fig. 2.11b). This is the transition to a streamer.

- Growth of *anode-directed streamers*:
  When the miniature avalanches spread to the avalanche head, the ions of the miniature avalanche tail mix with the electrons of the main discharge head, leading to a quasi-neutral plasma. The head of the miniature avalanche becomes part of the "new" head of the avalanche. The main growth mechanism of the discharge changes from avalanche to radiation of UV-light, photoionization and growth of miniature avalanches. The discharge is now of streamer type. Since the miniature avalanches appear at stochastic positions due to

the random nature of the photo-ionization, the streamers branch out into the direction of the miniature avalanches.

According to Moreau *et al.* [19], the growth velocity of the avalanches is about 10^4 m/s. Since the main processes in streamers are photo-ionization and propagation of UV-radiation, the growth velocity is limited by their speed and the time needed for the photo-ionization process. The UV-radiation propagates with the speed of light, and the photo-ionization is a rather rapid process, thus the streamer growth velocity is in the order of 10^6 m/s, according to Pavon [20]. This is much faster than the avalanche discharges, and the growth of a streamer occurs within one to a few nanoseconds.

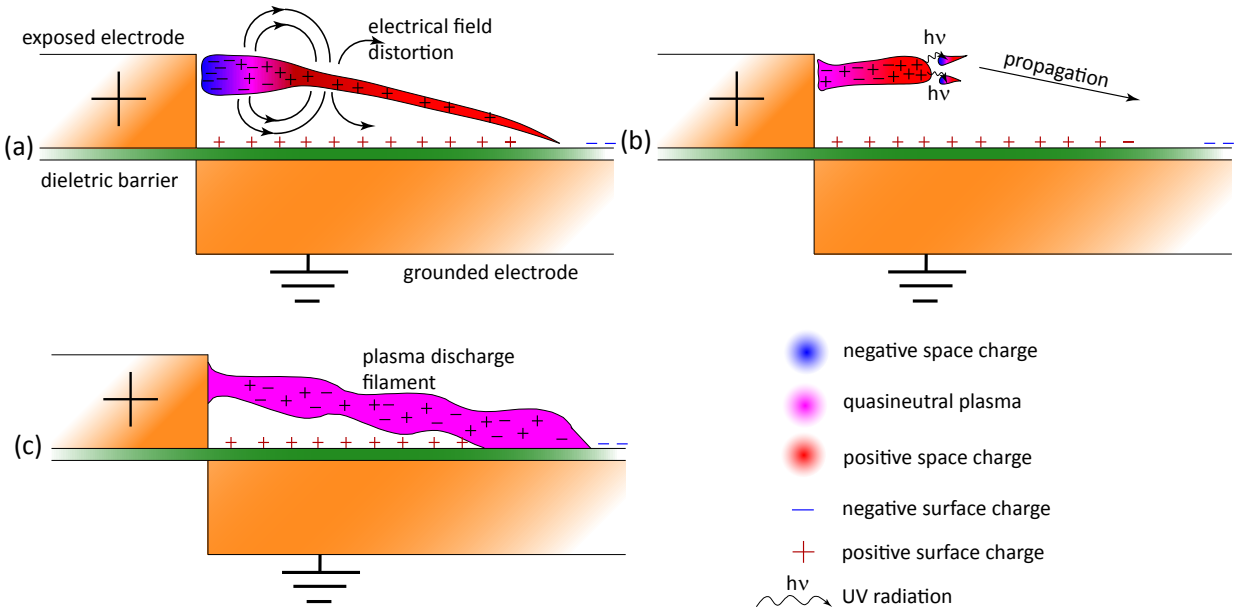

Figure 2.12: Process steps of cathode-directed streamers and discharge filament. (a) end of a Townsend-avalanche on the anode at t_1 (b) streamer transition through photo-ionization and creation of miniature-avalanches in the distorted electric field in front of the ion space charge at $t_2 > t_1$. (c) Filament discharge after (anode- or cathode-directed) streamer breakdown.

- Growth of *cathode-directed streamers*: For moderate gaps and moderate voltages, the avalanche-to-streamer transition takes place only when the primary avalanche has reached the anode. The avalanche has not grown strong enough and the space charge field is not sufficient to create miniature-avalanches before the avalanche has reached the anode [20]. When the avalanche reaches the anode, the ions in the tail of the avalanche remain in the gap, due to their slow drift motion ((a) in fig. 2.12). The space charge of the positive ions can significantly distort the applied electric field, as it was the case for anode-directed streamers. The strong field in connection with the UV-radiation triggers micro-avalanches by accelerating electrons ahead of the ion head towards the streamer (b). In this case the streamer is *cathode-directed*

- Filament discharge phase:
  Once the streamer (anode- or cathode-directed) spreads through the gas gap, the breakdown

phase is finished and the discharge phase along the original streamer path begins. The ions remaining in the gap form a thin filament made out of weakly ionized plasma ((c) in fig. 2.12). In the DBD, the dielectric barrier prevents the transition from the filament to an arc due to the built up of a surface charge on the barrier. Thus the lifetime of the filament is limited to a few tens of nanoseconds. Afterwards most of the ions move to the barrier, getting neutralized by electrons from the surface. The discharge ends and can only be restarted by increasing the externally applied electric field.

Since both, the avalanche and the streamers, underlie stochastic processes, discharge filaments can appear independently at several positions of the actuator. The repetition period of the discharge is significantly less than a microsecond, as can be seen in fig. 2.8, and in the order of a few megahertz. Thus the discharge seems as an homogeneous glow to the unaided eye.

2.2.3 Negative micro-scale filaments

According to the semi-analytical analysis of Soloviev, the discharge in the negative slope is made out of a pseudo-glow/corona discharge. The theory is supported by high-speed images taken by Bernhard [26] and Orlov [17] and by force measurements by Forte [27] and Leonov [28].

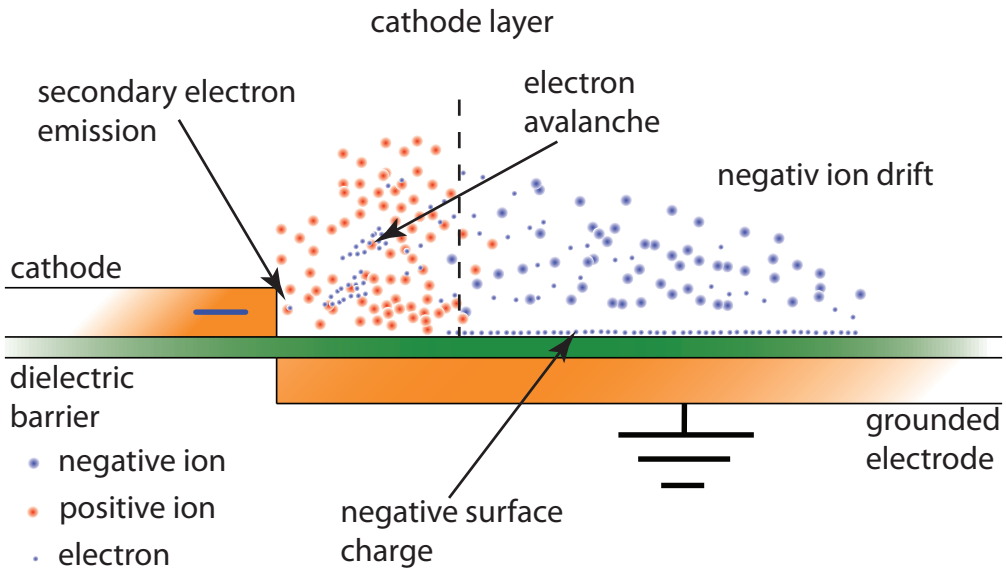

Figure 2.13: Corona discharge in a plasma actuator as described by Soloviev [24]. The streamwise extension of the cathode layer is strongly disproportionate, usually its streamwise extension is in the order of a few μm.

According to Soloviev, the ionization mainly occurs in a small zone between the upper electrode and a *virtual anode*, composed out of positive ions. This zone is called the *cathode layer*. Inside the cathode layer electron avalanches ionize neutral gas molecules. The electric field within the layer is intensified, whereas weakened in the region between the virtual anode and the point of lowest potential, the end of the lower electrode. Within the layer, the positive ions (mainly N_2^+) drift

towards the cathode and knock out electrons from the surface through secondary electron emission and simultaneously become neutralized. The electrons are accelerated within the intensified field. Subsequently, they knock out electrons from neutral gas molecules and create an avalanche discharge. After they crossed the virtual anode, they drift along the dielectric barrier towards the end of the grounded electrode, until they reach the end of the negative surface charge. On their path through the weakened electric field they can create negative ions out of neutral molecules due to electron attachment. The negative ions, mainly O^- ions, drift within the weakened electric field behind the virtual anode and contribute to the ionic wind. Important to mention besides the O^- ions are O_2^- ions, produced out of oxygen by the three body process $e + 2O_2 \rightarrow O_2^- + O_2$. O^-. O_2^- can further react to O_3^-, ionic ozone, in the relaxation phase.

The electrons at the dielectric barrier built up an weakening electric field, contrary to the externally applied electric field. Thus the discharge ends when enough charge is transferred from cathode to the dielectric barrier to reduce the effective field to zero. The remaining ions recombine or drift out of the discharge zone. The downstream drift of the negative ions is the main source of the ionic wind. The positive ions reduce the ionic wind, since they drift upstream. Nevertheless, since the cathode layer containing the positive ions is very thin, its contribution to the wind is negligible.

The discharge is very similar to a negative DC corona discharge. The difference is in its transient nature: Since the surface charge on top of the barrier and the shielding positive ions built up an electric field opposed to the external one, the discharge ceases within a short time. To restart the discharge, the voltage difference has to exceed the breakdown voltage again. It is expected that the velocity of a single corona-pulse is one order of magnitude lower than that of a single streamer.

All in all it can be said, the discharge in a plasma actuator is made out of single micro-scale filaments with a very short duration, and not out of a continuous discharge as in a drift-tube. According to current research, the discharge is dominated by streamers in the positive half-cycle and by a corona-discharge in the negative half-cycle.

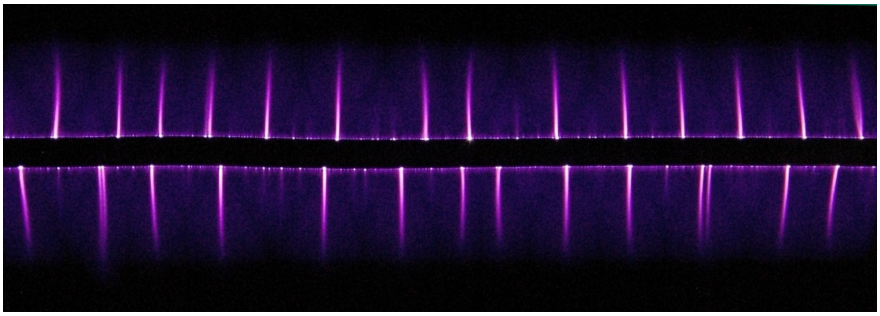

Figure 2.14: Image of large-scale filaments in the glow discharge of a two sided symmetric DBD plasma actuator.

Several researchers, like Pavon *et al.* [15] and Brauer *et al.* [29], directly observed large, long-lasting filamentary structures in the otherwise homogeneously glowing plasma for certain environmental conditions and applied voltages. Such filaments must be different from the micro-scale filaments, since micro-scale filaments have a duration of only fractions of microseconds and a spatial extension of a few hundred μm in width. They would thus not be visible for the unaided eye. The filaments are of technical interest, since they significantly damage the actuators due to massive heating and electro erosion of the dielectric barrier. Also, they seem to induce a three-dimensional flow. These facts, on one hand, show the necessity to prevent the filaments. On the other hand, it seems that the velocity of the ionic wind behind the large-scale filaments is significantly greater than in between the filaments. Thus the filaments might be of practical use for flow control, for example in boundary layer control using vortices of the three-dimensional flow.
Different workgroups tried different approaches to explain these filaments, like assuming them to be streamers or avalanche discharges. Brauer *et al.* [29] simulated the glow discharge for high voltages in the streamer regime, and observed filamentary structures of large-scales. Nevertheless, they did not take the photo-ionization by UV-radiation into account, which is shown to be the main mechanism for streamer formation. Also, the properties gained from the simulation, such as the lifetime of the filaments, were different from those observed in the experiments of this work. Streamers, for instance, are much smaller and have a significantly shorter lifetime than the large-scale filaments. Also, the streamers ramify along their path due to the random nature of the photo-effect, but the large-scale filaments are straight. Thus, the theory of Brauer *et al.* [29] does not explain the filaments sufficiently.

The following sections describe these filaments introducing a newly developed, physically more founded model. Within this theory, the filaments are assumed to be produced by thermal instabilities in the plasma. The model is supported by experiments, where the environmental impact on the instabilities is studied and compared with the model.

2.3.1 Theory of glow discharge instabilities

Instabilities (i.e. a catastrophic increase of initially small perturbations) grow in a non-steady process. The system either comes to a new, more stable state, or a steady state is never achieved, so that a periodically changing process is established.
Instabilities can be described through a chain of casual links of various processes. Two types of instabilities in plasma are given in literature of volume discharges, longitudinal and transverse instabilities with respect to the electric field vector. The longitudinal instabilities, so called striations, are manifests of ionization oscillations and waves. A striated discharge may be caused by stepwise ionization, the maxwellization of the electron distribution function, and by any agent causing enhancement in longitudinal inhomogenities [9]. Since striations have only been observed in volume discharges and not in dielectric barrier discharges, we will focus on transverse glow discharge instabilities, caused by thermal instabilities.

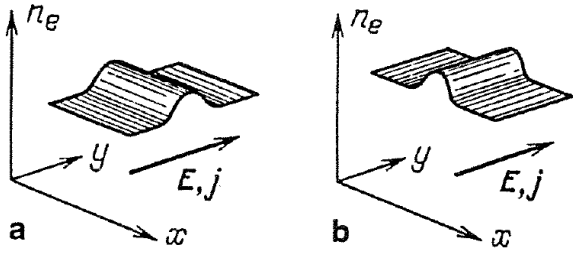

Figure 2.15: Longitudinal (a) and transverse (b) plasma instabilities with respect to the electric field vector, according to Raizer [9]

2.3.2 Description of the transverse thermal instability theory

The most common type of instability in a gas discharge plasma under atmospheric pressure is the so called thermal instability. Since they arise at high power levels, they limit the power of the active medium of CO_2 lasers. The topic of thermal instabilities for DC and RF discharges was thus subject to considerable research effort in the past, for instance by Velikhov [31], Chirokov [32] and Raizer [9]. Velikhov [31] and Chirokov [32] developed theoretical models of the transition from a stable glow discharge to the filaments in a volume discharge. Starting from that model, a model of the instabilities in surface dielectric barrier discharges can be developed, as will be described in the following.

A stable glow discharge is never fully homogeneous. Geometrical imperfections of the setup, such as sharp points in the electrodes or scratches in the dielectric barrier cause a slightly enhanced electric field in some areas of the discharge compared to others. Those inhomogeneities trigger a chain of processes, that lead to thermal instability when the electric field is sufficiently high. These processes are:

1. Imperfections in the actuator setup lead to a slightly increased electric field strength $\delta E \uparrow$.

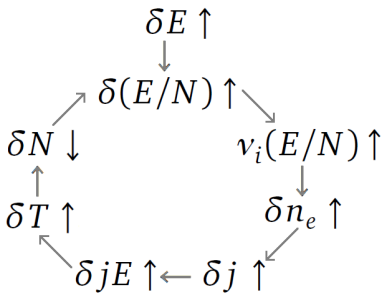

Figure 2.16: Instability built-up process cycle in the glow discharge

2. An increase in the electric field obviously increases the reduced electric field $\delta(E/N) \uparrow$ (i.e. electric field over gas density)

3. An increase in the reduced electric field leads to a higher ionization coefficient α_i, since, according to Lagmich [33], α_i is a strictly monotonic increasing function of the reduced electric field. Higher ionization coefficients lead to an increase in the ion production rate $\tilde{\nu}_i(E/N) = \alpha(E/N)/v_d$ (see section 2.1.2), and thus to an increased production rate of electrons. With a higher production rate of electrons the electron density δn_e increases.

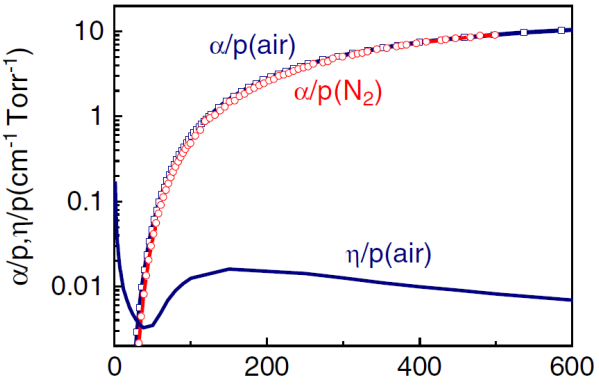

Figure 2.17: Reduced ionization α/p and attachment ν/p coefficients as function of the reduced electric field, according to [33]. The reduction was made with the pressure p instead of the gas density N, but p and N are linearly dependent through the ideal gas equation p=NkT.

4. Since the electric current density $j = nE$ in the discharge is mostly due to electron drift, an increase in the electron density n_e causes the current density to rise $\delta j \uparrow$. This happens only if the electric field E does not decrease simultaniously due to the higher consumed power, thus for highly stable external power supplies.

5. The higher electric current density leads to an increase in the dissipated power in the plasma $\delta jE \uparrow$.

6. Since most of the power consumption in a DBD plasma actuator is dissipated into heat (see Roth [3]), an increase in the power consumption obviously increases the gas temperature $\delta T \uparrow$.

7. With increasing temperature of the gas under constant pressure, the gas density $\delta N \downarrow$ decreases simultaneously, according to the ideal gas law p=NkT.

8. When the gas density decreases, the reduced electric field $\delta(E/N) \uparrow$ increases. The chain continues with the third step.

Imperfections in the actuator are not necessarily the origin of the instability, also fluctuations in temperature and density are possible triggers. Therefore the chain does not need to start with the first step.

The fourth and fifth steps of the chain exhibit the origin of an upper limit, where instable development ceases: when the power dissipated in the filaments exceeds the power delivered by the external circuit, the heating process comes to an end. The development can be prevented by decreasing the electric field strength at the onset of instabilities.

2.3.3 Equation of the thermal balance of plasmas

In order to prevent instabilities and the complications associated with them, it is necessary to understand under which conditions the process is triggered to instability. In order to develop a stability criterion, the following assumptions can be made:

- A DBD is considered to be created in an external airflow, as it is the case for common plasma actuator applications. The electric field within the actuator is assumed to be homogeneous. This is not necessarily the case, but can be assumed locally in a good approximation.
- The pressure is constant within the gas volume.
- All electrical energy is dissipated into heat within the gas volume. This approximation is valid, since only a small fraction of the input power (typically of the order of 0.1%, see [3]) is converted into kinetic motion of the gas.

The energy balance between the heat transfer (second term on the right side) and the dissipated electrical power (first term on the right side) can be written as:

$$c_p \rho \frac{dT}{dt} = j \cdot E - c_p \rho (T - T_0) \cdot \nu_{dc} \tag{2.7}$$

where T_0 is the temperature of the surrounding gas flow, c_p the heat capacity of the gas at constant pressure and ν_{dc} denoting the heat removal-frequency. The term on the left side describes the heating of the neutral gas. The heat-removal frequency ν_{dc}, a factor that describes how quickly heat is removed out of the volume, is:

$$\nu_{dc} = \frac{\chi}{\Lambda_T^2} + \frac{2 \cdot u}{\Delta x} \tag{2.8}$$

The first term in equation 2.8 is the heat removal due to diffusion, the second term the heat transfer due to convection along the actuator. In the convective term, Δx is the plasma extension and u the velocity of the surrounding airflow. Since the released heat, on average, is transferred only half of the plasma length (due to molecular movement), the length has to be divided by two.
The diffusive term is the ratio of he thermionic conductivity $\chi = \frac{\lambda}{N c_p}$ and a form factor Λ_T. The form factor has the dimension of a length and has to be calculated numerically for a DBD actuator geometry. Most importantly, it is constant for a given actuator geometry and can thus be assumed to be constant here.
A steady-state temperature is reached when

$$j \cdot E = c_p \rho (T - T_0) \cdot \nu_{dc} \tag{2.9}$$

Eqn. 2.7 can be rewritten in a simpler form:

$$\frac{dT}{dt} = T \cdot \nu_h - (T - T_0) \cdot \nu_{dc} \tag{2.10}$$

with the help of the frequency of heating ν_h, a factor that describes how quickly heat is dissipated into the gas by the external power supply:

$$\nu_h = \frac{\gamma - 1}{\gamma} \cdot \frac{j \cdot E}{p} \tag{2.11}$$

with γ being the adiabatic constant index. Thus, the frequency of heating is just dependent on the input-power of the system and the pressure.

The second equation necessary for the determination of a stability criterion is the electron-density balance-equation:

$$n_e = \frac{\nu_i(E/N) - \nu_a(E/N)}{k_r} \tag{2.12}$$

with the coefficients for ionization and electron attachment ν_i and ν_a respectively, and the recombination rate k_r. The coefficients are only dependent on the reduced electric field E/N (see Lagmich [33]).
The variation of the logarithm of this function yields

$$\frac{\delta n_e}{n_e} = \frac{\ln(\nu_i(E/N) - \nu_a(E/N))}{\ln(E/N)} \cdot \left(\frac{\delta E}{E} - \frac{\delta N}{N} \right) \tag{2.13}$$

The factor

$$\nu^* = \frac{\ln(\nu_i(E/N) - \nu_a(E/N))}{\ln(E/N)}$$

is called logarithmic sensitivity and describes the sensitivity of the production rate under variation of the reduced electric field.

The third important law is the ideal gas law p=NkT. The variation of the law with the assumption of constant pressure yields

$$\delta p = k(T\delta N + N\delta T) = 0 \Rightarrow \frac{\delta N}{N} = -\frac{\delta T}{T} \tag{2.14}$$

The last equation necessary for a full description of the system is the variation of the rate of heat removal frequency with respect to variation of the electron density and electric field strength. The variation of eqn. 2.11 yields

$$\frac{\delta \nu_h}{\nu_h} = \frac{\delta(jE)}{jE} = \frac{\delta(n_e E^2)}{n_e E^2} = \frac{E^2\delta n_e + 2n_e E\delta E}{n_e E^2} = \frac{\delta n_e}{n_e} + 2\frac{\delta E}{E} \tag{2.15}$$

$$\Rightarrow \frac{\delta \nu_h}{\nu_h} = \frac{\delta n_e}{n_e} + 2\frac{\delta E}{E} \tag{2.16}$$

The second equality in eqn. 2.15 is not self-evident and has to be discussed in detail. The current in a plasma can be written as $j = en_e\mu_e E$ under the given assumptions. With the help of eqn. 2.4, the formula can be rewritten as $jE = e^2 n_e E^2/(m_e\nu_e)$. The second equality in eqn. 2.15 directly results from $jE = e^2 n_e E^2/(m_e\nu_e)$ under the assumption that the collision frequency ν_e is approximately constant under variation of temperature. The assumption is valid, since the variation of factors in the varied product $\nu_e(T) = N(T)v(T)\sigma_{tr}$ have opposite signs and mostly cancel each other out, according to Raizer [9] (with v being the velocity of random motion and σ_{tr} the cross section of elastic collision).

Combining equations 2.13, 2.14 and 2.16 with equation 2.7 finally produces the equation for thermal fluctuations:

$$\frac{d\delta T}{dt} = \delta T(\nu_h\nu^* + \nu_h - \nu_{dc}) + \nu_h(\nu^* + 2)T\frac{\delta E}{E} \tag{2.17}$$

Assuming the drop of the electric field strength across the plasma column to be fixed ($\Rightarrow \delta$ E = 0), an exponential Ansatz of $\delta T \propto \exp(\Omega\ t)$ solves the differential equation. This yields

$$\Omega = \nu_h\nu^* + \nu_h - \nu_{dc} \tag{2.18}$$

Even if $\delta E \neq 0$, the same result for Ω is achieved, if $\delta E/E$ can be assumed constant.
If the exponent Ω is greater than zero, $\Omega > 0$, the function grows exponentially and thus leads to instabilities. Therefore the system becomes instable for

$$\begin{aligned} \Omega = \nu_h\nu^* + \nu_h - \nu_{dc} &> 0 \\ \Rightarrow \nu_h = \frac{\gamma - 1}{\gamma}\cdot\frac{n_e\cdot E^2}{p} &> \nu_{dc}/(1+\nu^*) \end{aligned}$$

$$\Rightarrow n_e E^2 > \nu_{dc}/(1+\nu^*)\cdot p\cdot\frac{\gamma}{\gamma - 1} \tag{2.19}$$

or, with the help of the ideal gas law

$$n_e E^2 > \nu_{dc}/(1+\nu^*) N c_p T. \tag{2.20}$$

Since ν_{dc} is not dependent on temperature, an increase of the cooling rate stabilizes the process. This can be performed through a higher flow rate of the surrounding medium or a lower temperature.
The logarithmic sensitivity usually takes values of $\nu^* \approx$ 4-9. Combining eqn. 2.20 with 2.9 yields instability for

$$\begin{aligned} T - T_0 > 1/(1+\nu^*)T = (0.1-0.2)T \\ \Rightarrow \frac{T}{T_0} > (1.1-1.2) \end{aligned}$$

Therefore a temperature rise of 10% - 20% is able to trigger a transition from a stable glow discharge to instable filaments.

3 Experimental setup

In the following sections, the experimental setup is described. At first,setup of the plasma actuator, such as the high-voltage power supply and the plasma actuator geometry are explained. Secondly, the experimental setup of the experiments on micro-scale filaments is characterized. The experiments on large-scale filaments are described in the third section.

3.1 Plasma actuator setup

In the following two subsections, the high-voltage power supply and the plasma actuator geometry are explained in detail.

3.1.1 High-voltage generation

The plasma actuators need a supply of high voltage with alternating amplitude of 3-20 kV peak-peak and 1-20 kHz in order to create a discharge. The high-voltage power supply used in the high-speed streak camera image experiments was the *MiniPuls 2.1*. For the current measurements the *MiniPuls 6* and the *MiniPuls 2.1* were used. Both *MiniPuls* devices are from *GBS Elektronik GmbH* and have the same principle of operation. The principle will be explained on the example of *MiniPuls* 6 since it is able to produce higher voltage amplitudes and output power levels than *MiniPuls 2.1*. Also the range of output voltage frequencies as well as achievable resonance frequencies exceeds that of *MiniPuls 2.1*. *MiniPuls 6* consists out of a *bridge* and a *transformer cascade*. In

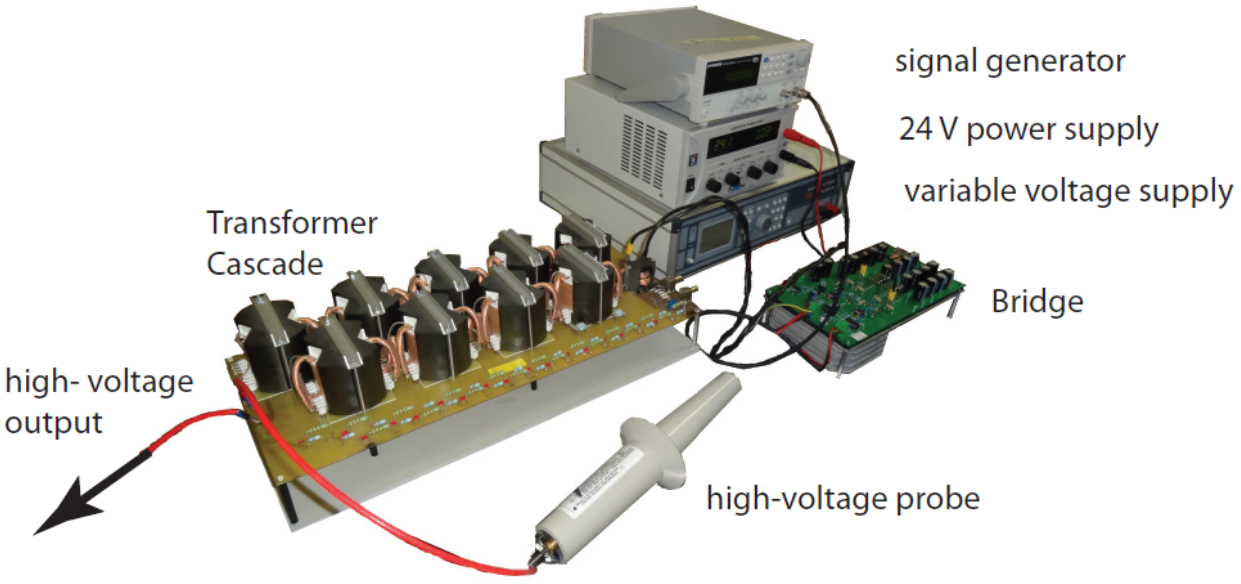

Figure 3.1: Setup of the high-voltage generator *MiniPuls 6*.

order to achieve a voltage of radio frequency AC, the bridge is connected to a GW Instek SFG-2004 signal generator that delivers a ± 5 V rectangle signal. The modulation frequency of the signal must be the desired voltage frequency of the high-voltage.
The input voltage for the bridge of the *MiniPuls* is produced by a 24 V DC laboratory power supply unit. Within the bridge, this voltage becomes modulated with the signal-generator frequency through an oscillating circuit made out of several capacitors and coils. Thus the signal is alternating with the frequency given by the signal generators when leaving the bridge. It is of low voltage and high current. The exit-voltage amplitude of that signal can be amplified between 0% and 100% by another voltage signal, produced by an ELV SPS-9540 M switch DC power supply.
The voltage on the exit of the bridge is fed into the transformer cascade. The Cascade consists out of multiple coils. The number of coils can be adjusted in order to meet the load impedance, with a maximal number of eight coils. Each of the coils increases the signal voltage by maximally 8.5 kV while hereby decreasing the current. The voltage at the Cascade exit can thus ideally reach up to 68 kV.
The impedance of the plasma actuator and the voltage supply have to be matched carefully, otherwise no clean sinusoidal signal can be produced and the achievable voltage amplitude is decreased. This frequency adjustment to the resonance frequency can be done by adding or removing coils from the system.

3.1.2 Plasma actuator geometry

The plasma actuator consists out of two copper electrodes made out of self adhesive copper tape, separated by a 0.33 mm dielectric *Kapton* layer. The dielectric barrier was created by attaching two sheets of Kapton tape over another. The thickness of the electrodes is 35 μm. The upper electrode has a width of 10 mm, the lower electrode one of 20 mm. The length of the electrodes is 100 mm. The actuator was attaced on top of an acrylic glass plate. We will refer to this geometry as *asymmetric actuator*. unless otherwise mentioned, this configuration is used in all experiments.

3.2 Experimental setup of experiments on micro-scale filaments

In order to understand the properties and mechanisms of the discharge on small time scales, the discharge is investigated in two different kinds of experiments. The first one was to take images of the plasma with the help of a streak camera. These images show the discharge develops over time. The electric current produced by the discharge was measured in a second set of experiments in order to evaluate behavior of the discharge in the positive and negative slope under variation of voltage frequency and amplitude. Both experiments are explained in the following subsections. For the current measurements, necessary post-processing steps are explained in a third subsection.

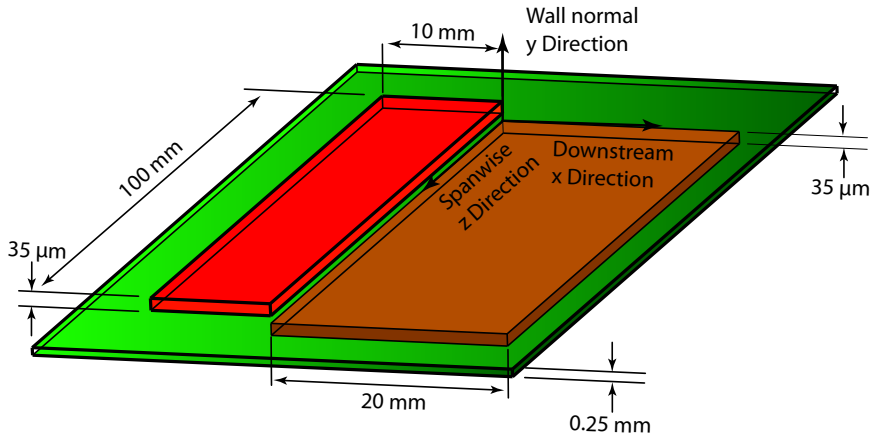

Figure 3.2: Geometry of the *asymmetric actuator* configuration and used coordinate system. The coordinate origin is on top of the dielectric, at the contact line of upper and lower electrode.

3.2.1 High-speed streak camera images

The high-speed visualizations of the discharge are performed with a *C2830 Hamamatsu Streak Unit*, with a *C4742-95 camera for C2830 Hamamatsu* CCD attached. The used objective lens of the camera is a *Nikon F-mount*, with 20 mm focal length and an focal ratio of D=1.1. It is supported by an extension tube of 20 mm and an adapter to the C-mount connection of the camera. The trigger that has been used to start the measurement is a *DG-535* delay/pulse generator from *Stanford Research*. The generator is connected to a Tectronix DTS 2004B oscilloscope that simultaneously measures the voltage and charge signal of the plasma actuator. The high-voltage probe that is used for this purpose is a *TestTec HVP-15HF*, the low voltage probe for the current signal is a *Tectronix P2220*. The pulse generator sends two trigger signals with a short delay time. The first pulse opens the gate in the slow-speed sweep unit (SSSU). The second pulse is split into two identical signals. One activates the SSSU and the camera to capture a streak-image of the plasma actuator. Simultaneously, the other triggers the oscilloscope to record the voltage and charge signal of the plasma actuator within a given time interval. A streak camera consists out of a conventional camera and a SSSU. An incident light pulse first passes through a slit in the SSSU, extracting a one-dimensional time-dependent line out of the two-dimensional image. The photons of the light pulse knock out electrons from a photocathode. These electrons are accelerated and multiplied in an electric field of a MCP inside of the SSSU. After the accelerating field is a second high-voltage electric field, orthogonal to both, the flight direction and to the slit-like transversal electron distribution. The field strength is increased by time, thus the electrons are deflected depending on their time of arrival. The one dimensional line is therefore swept into a two dimensional image, where the second dimension shows the schanges of the slit illumination with time. Finally, the electrons are stopped at a (phosphor) screen, which creates a visible image. This image is captured by the conventional camera and recorded on a computer.
The streak time (duration of image recording) can be adjusted between 10 ms and 1 ns. Also, the signal amplification in the MCP can be adjusted. Since luminosity of the discharge is small and

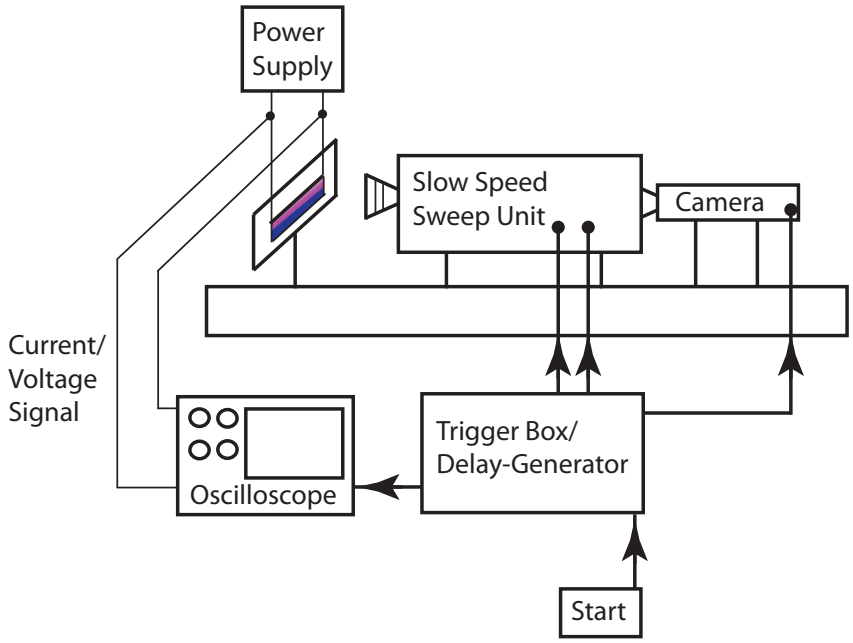

Figure 3.3: Experimental setup of the high speed measurements.

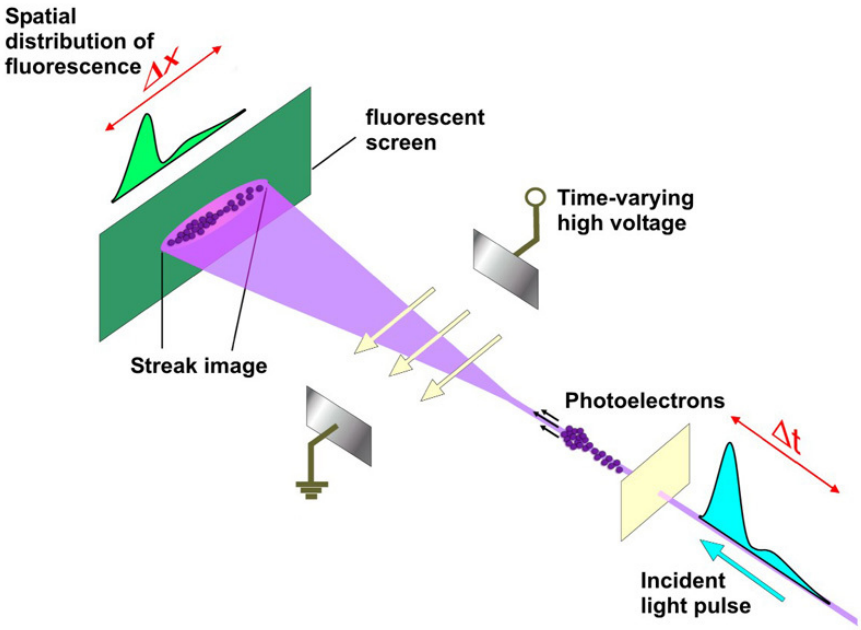

Figure 3.4: Schematic diagram of a conventional streak camera, according to [21].

the streak time short, the contrast of the images is close to zero. Thus the brightness gain of the images has to be raised to maximum in order to be able to record the discharge.

Relevant actuator voltages that are used for the high-speed images experiments and for other experiments in this work are 14, 15 and 16.5 kV, corresponding to an electrical power consumption of 380, 440 and 500 Watt per meter actuator length, respectively. The electrical power consumption is determined with the help of a probe capacitor in the circuit. Measuring the voltage drop across the

capacitor gives the voltage-charge characteristics. The integration of the resulting Lissajous-figures over K cycles gives the consumed power.

$$P_A = \frac{f}{K} \sum_{k=1}^{K} \oint_k Q(t) dV \tag{3.1}$$

For further information on the calculation of power consumption see appendix 5. The power levels of 440 and 500 W/m lead to a filamentary (unstable, see chap. 2.3) discharge for the asymetric actuator configuration. The power levels are chosen since their bright discharges lead to images with sufficient contrast for small streak times. The discharge produced by a 500 W power level significantly heats the actuator, thus the actuator can only be operated for a very short time under these conditions without an electric break-through in the dielectric or delaminating of the Kapton layers. Nevertheless, the power level is useful when the actuator is operated in an external airflow and thus cooled, since it still leads to instabilities under such conditions.
The actuator was driven by the *Minipulse 6* generator at a frequency of 10 kHz, thus the period was 100 μs. The streak time of the captured images were 50, 100 and 200 μs, respectively, corresponding to one half, one or two periods. Due to internal effects of the camera, not the complete streak time can be captured.

3.2.2 Current measurements

As described in the appendix 5, the power consumption of a DBD plasma actuator is usually determined by measuring the voltage drop over a capacitor in series with the actuator, yielding the charge that passed the actuator at a given time. This is done since the discharge duration is too low and the repetiton rate to high to measure the current without an expensive oscilloscope. Nevertheless, the direct measurement gives a better insight into the physics of the discharge, since

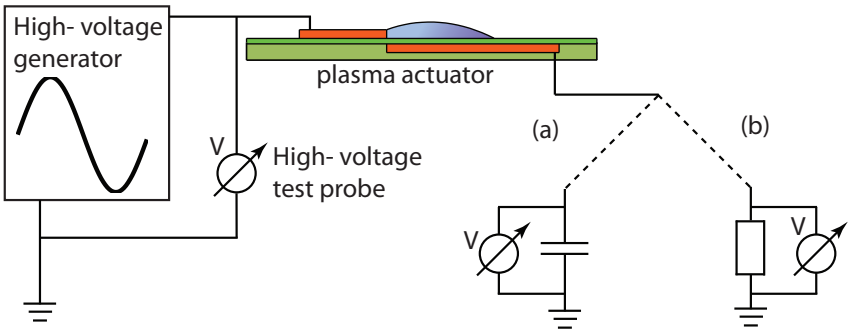

Figure 3.5: Circuit diagram of the plasma actuator with (a) measuring the charge flowing through the actuator in a capacitor or (b) measuring the current through the actuator with a test resistor.

it shows the current transferred in single discharges instead of the integration over multiple discharges. The duration of the discharge can give rise to the regime.
A *LeCroy WaveJet 354* with a bandwidth of 500 MHz and record rate of 2 Gigasamples/second is

used for these measurements, sufficiently to resolve discharges with a duration of 2 ns or more. The low-voltage probe used is a LeCroy test probe with 500 MHz bandwidth, measuring the voltage drop across a 15.42 Ω power resistor. The resistance is chosen to be small enough to be nigligible compared to the actuator-resistance, but also to be sufficient to produce a clear signal. A Tectronix 6015A high-voltage probe is used to measure the voltage from *MiniPuls 6*. The actuator design chosen is that of the asymetric actuator.

3.2.3 Post-processing and filtering

For both, the camera images and the current measurements, post processing steps are necessary and will be described in the following two subsections.

High speed streak camera images

It is important to match the electric signal of the discharge with the image taken by the streak camera. Due to unknown delays in the connecting wires and the camera, there is an unknown delay between the start of the voltage measurement in the oscilloscope and the start of the exposure in the camera. In order to determine the delay, measurements and images are taken over multiple voltage periods for different frequencies. From the different positions of the dark zone (zone of no discharge, see figure 4.1) in the images, multiple candidates of the vague delay can be derived, corresponding to the extremes of the voltage amplitude. By lowering the frequency, all false delay times can be excluded by comparing the images with the voltage measurement. The determined delay times corresponding to the different exposure times can be seen in table 3.1.

.

streak- time	delay
20 μs	54 ($\pm$2) μs
50 μs	77 ($\pm$3) μs
100 μs	164 ($\pm$5) μs
200 μs	404 ($\pm$8) μs

Table 3.1: Delay times corresponding to different streak times.

Current measurements

The current measurements require significant post-processing of the data, since the current is made of multiple single peaks with subsequent oscillations, as can be seen in figure 3.6. The position and amplitude of individual peaks are highly random. Multiple discharge cycles have thus to be recorded in order to get clear signals.
The oscillations after the current peak are probably due to reflections in the wires and the *MiniPuls*,

since the damping rate is increased when the wires are shortened. Nevertheless, they cannot be eliminated since the amplification coils inside the *MiniPuls* always create an oscillating circuit. Experiments dealing with current measurements of other works, like [26] and [20], reveal no oscillations, most likely since they used a *Trek Amplifier* instead of a *MiniPuls* as a voltage generator. The *Trek Amplifier* uses a different amplification technology. Furthermore, there is no physical reason for the oscillations, since the current in the discharge is suspected to flow in the direction of the voltage gradient and not reversely within one half-cycle of the applied high-voltage. This is the case for all first peaks before the oscillations in both the positive and negative half-cycle, but not for the adjacent oscillations. Thus a filtering method has to be developed in order to isolate the

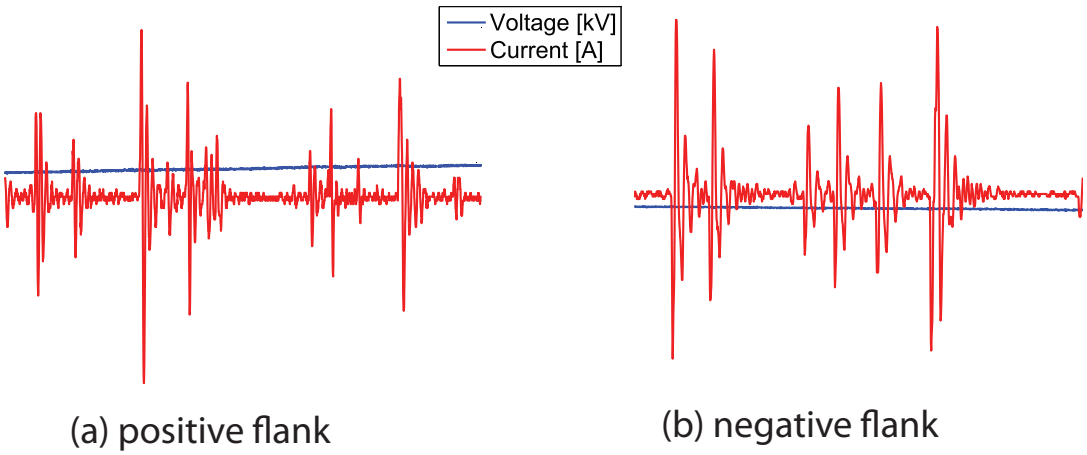

Figure 3.6: Oscillations in the current measurements of the discharge.

current peaks of the discharge from the reflections. First, the typical duration of the oscillations is identified with the help of a Fourier-transformation. Then, all local maxima and minima are determined by comparing the sign of the gradient between different measurement values. For all extremes it is checked whether there is another extreme with a greater absolute value within half of the duration or not. If there is none, the extreme is counted as a discharge. Otherwise, the greater extreme is picked and checked itself. Values within the maximal noise level are excluded by adding a threshold of minimal extreme amplitude. The noise level can be determined from regions without discharges under the assumption that the noise does not increase with the occurrence of discharges. An exemplary result is given in figure 3.7. In a final step, the extreme corresponding to a discharge (maxima for positive half-cycle, minima for negative half-cycle) have to be separated from those resulting from oscillations. For the positive half-cycle, each maximum is analyzed and characterized as a discharge if

(a) the time interval to the previous extreme, no matter maximum or minimum, is longer than three periods of the oscillation. That condition identifies all discharges that occurred after the oscillations of the previous discharge are damped below the threshold value. If condition (a) does not hold, an extreme is still counted as a discharge if

(b) the previous maximum is at least 25% smaller than the current one. That condition identifies all discharges that occur before the oscillations of the previous discharge are damped below threshold value. 25% was found to be a good value, since it was less than the reduction due to

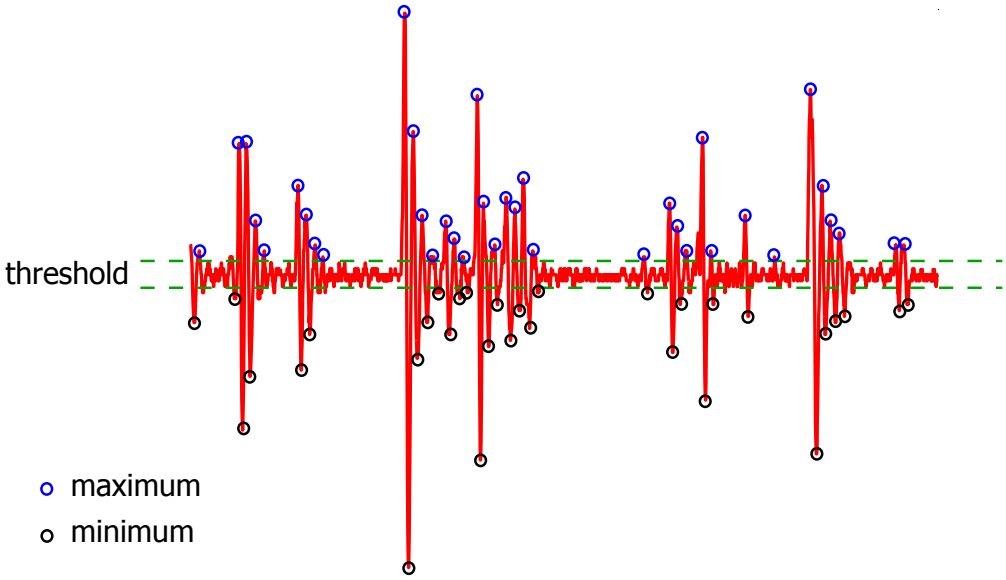

Figure 3.7: Identification of local maxima and minima for discharges in the positive half-cycle.

damping but also sufficient to avoid double-counting of oscillations with a low damping rate superimposed with high noise.

For the discharge in the negative half-cycle, the conditions are the same, provided maxima and minima are exchanged. From the location and amplitude of the discharges identified by the filter,

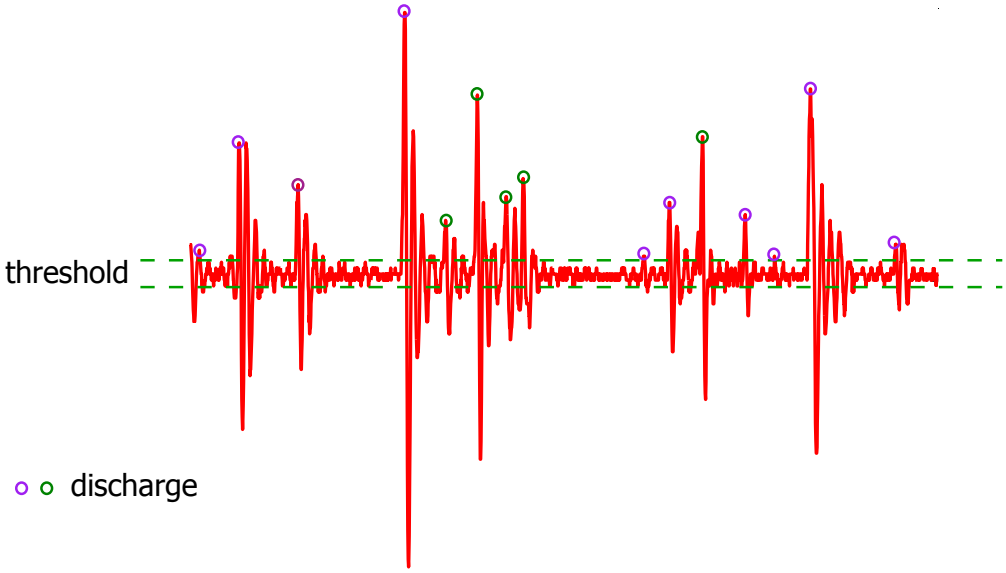

Figure 3.8: Current peaks identified by the filter for discharges in the positive half-cycle. Discharges identified by condition (a) are purple, those identified by condition (b) are green.

parameters such as mean amplitude, mean elapsed time between two discharges and mean number of discharges per half-cycle can be derived. The source code of the filter can be found in appendix 5

3.3 Experimental setup of experiments on large-scale filaments

The following subsections describe the setup of the experiments on the nature and behavior of large-scale filaments. The first describes the measurement of the plasma temperature, the second the experimental setup of experiments with an actuator in an external flow and the last the setup of measurement of the velocity of the ionic wind inside and outside of large-scale filaments.

3.3.1 Experiments on filament temperature

One important experiment regarding the properties of large-scale filaments is to measure the spatial temperature distribution of the plasma in different operating conditions. The temperature distribution can be easily measured with an infrared thermo camera. The camera used in the temperature experiments is the *Optris PI160* by *Optris Infrared Thermometers GmbH*. The systematical error of the camera is $\pm$2K or $\pm$2%. It is fixed at 30 cm above the plasma actuator in all experiments. For some operating conditions it is impossible to operate the plasma actuator long enough to reach steady state temperature. This is due to the fact, that the discharge causes ablation of the dielectric layers before the steady-state is reached. In that case the steady state temperature is extrapolated from the temperature sequence. Since the error in the extrapolation exceeds the systematical error, it is used as the dominant error for those cases.

Figure 3.9: Optris PI160 infrared thermo-camera

3.3.2 Experiments on actuators in flow

In order to measure the influence of an external flow on the instabilities, the plasma actuator is placed into the *Small Eiffel Wind Tunnel* of the TU Darmstadt. The tunnel is able to deliver airflow with a free-stream velocity between 0 and 30 m/s. The test section cross section is 240 x 180 mm with a length of 800 mm. The test section is designed for maximum optical accessibility from three sides. The turbulence intensity of the flow inside the test section is estimated to be approximately

0.7%. The actuator is mounted on one wind-tunnel wall, parallel to a window. It can thus be easily seen when the actuator has reached instable conditions.

Figure 3.10: Small Eiffel Wind Tunnel

3.3.3 Experiments on the velocity of the ionic wind

The velocity of the ionic wind is measured with the help of a Pitot tube and a *Setra Static Pressure Probe, Model 267*. The pitot tube is made out of a glass to ensure electric insulation from the plasma discharge and has an inner diameter of 2 mm. The tube and the probe are connected with a 0.5m rubber pipe. The velocity can be determined by measuring the stagnation pressure p_t of the flow with the tube and the static pressure p_s away from the flow. The Setra probe can measure pressures differences up to 250 Pa. For subsonic flows, the stagnation pressure is

$$p_t = p_s + \left(\frac{\rho u^2}{2}\right) \tag{3.2}$$

The flow velocity thus corresponds to

$$u = \sqrt{\frac{2(p_t - p_s)}{\rho}} \tag{3.3}$$

The stagnation pressure of the ionic wind is measured downstream of the upper electrode in x-direction at different streamwise positions, both behind large-scale filaments and in areas without the filaments. The measurement was repeated for different downstream positions in order to find the maximum flow velocity of both areas.

4 Results

The following two sections describe the experiments for the investigations on the nature of both micro-scale and large-scale filaments and the results of those.

4.1 Results of experiments on micro-scale filaments

In a first set of experiments, images of the discharge are captured with the help of a streak camera. The current through the actuator and its dependence on electric parameters are investigated in a second set of experiments. The results of the measurements with the streak camera and that of the current measurement are discussed in separate subsections, since the high-speed images mainly describe the spatial composition of the discharge and its evolution over time within a few hundred μs, whereas the current measurements describe the temporal evolution within some hundred nanoseconds and the behavior of the discharge under different voltages and frequencies.
It is not possible to investigate the voltage and frequency dependency of the spatial composition with the available experimental setup, since the luminosity of the plasma at low voltages or frequencies far away from resonance frequency is too low to be captured by the streak camera. For an objective with D=1.1 the input power of the plasma actuator has to be raised to very high levels in order to get a clear image of the discharge.

4.1.1 High-speed streak camera images

The slit of the streak camera is first mounted spanwise, focusing the upstream edge of the lower electrode. This is where the discharge is brightest, leading to images with high contrast, even at small streak times. Thus, the images show where the discharge occurs along the electrode, its development and shape. An image with 200 μs exposure time can be seen in figure 4.1. Due to limitations of the screen and the objective, only 140 μs are visible on the image, even though the overall streak time was 200 μs. On the right side, the corresponding voltage can be seen. Four different regimes within one cycle can be identified:

- A dark region, starting when the voltage is maximal around t=0 μs. Its duration is about 15-20 μs. The change in the voltage amplitude in this stage is very small.
- A region of small spots, homogeneously distributed, with bright lines in it. It starts around t=15 μs and lasts around 35-40 μs. The bright lines are presumably instabilities (see section 2.3). The stage of a spotted discharge starts at the same time everywhere along the electrode, but the spots do not occur simultaneously. The instabilities need a few μs to develop and

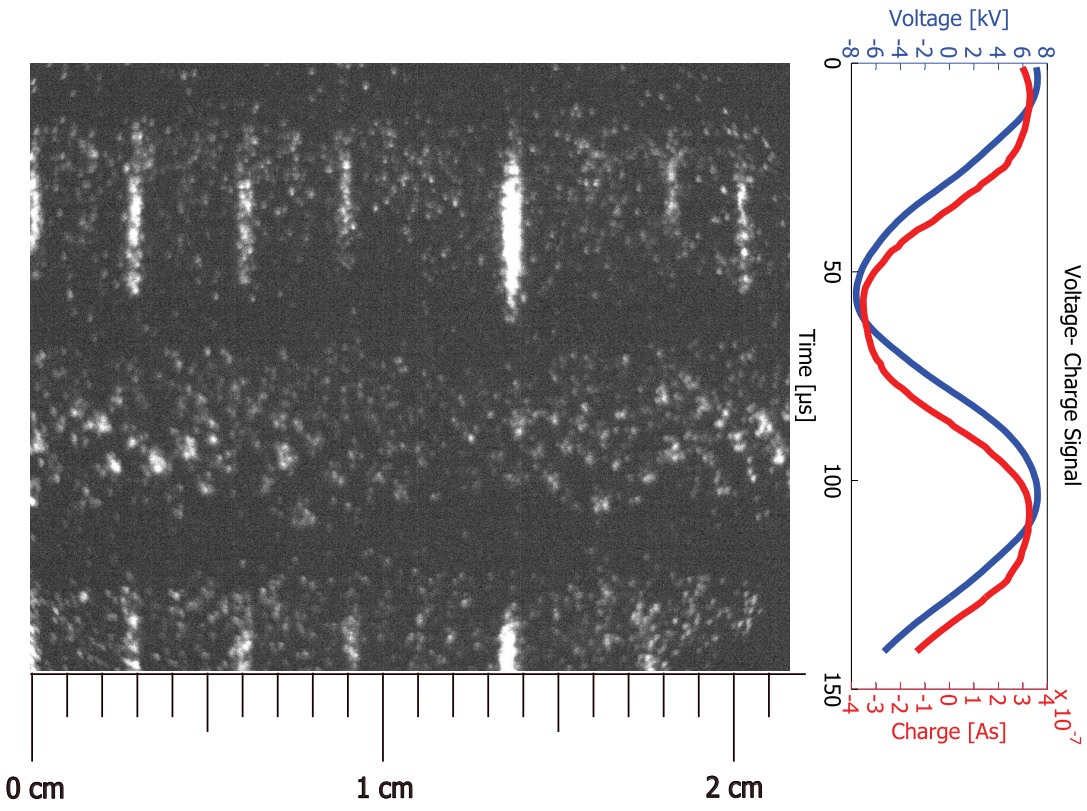

Figure 4.1: Streak camera image of the discharge, slit spanwise. The frequency is 10 kHz, the power consumption 440 Watt. The streak time is 200 μs.

disappear before the spotted area ends. The gradient of the voltage amplitude is strongly negative during that stage.

- A second dark region after the spotted area of again 15-20 μs duration, starting roughly at t=50 μs. As in the first dark region, the change in the voltage amplitude during this stage is very small, since it is in the minimum of the sinusoidal voltage.
- A region of big spots, homogeneously distributed. There are less spots, but with higher brightness and greater diameter than in the stage of the decreasing voltage amplitude. In contrast to that stage, no instabilities are visible. The voltage amplitude is strongly increasing.

The four stages restart after the last one has ended and a new voltage cycle begins. The first dark region and the stage of negative discharge of the second cycle can be seen in the figure as well.

In a second experiment, the input power of the plasma actuator was increased from 440 W/m to 500 W/m. An image of the corresponding discharge can be seen in figure 4.2. The exposition of that image starts roughly 50 μs after the voltage amplitude was maximal. Since the cycle duration is 100 μs, the voltage is minimal. All four discharge stages are visible again. The duration of both spotted areas has increased by a few μs and those areas covers the edge of the electrode around

75% of the total discharge time. The duration of dark stages is thus decreased by a few μs. There are more spots in each stage compared to the first experiment and they are brighter. Again, the instabilities occur when the voltage amplitude is decreasing. It is obvious that the bright spots

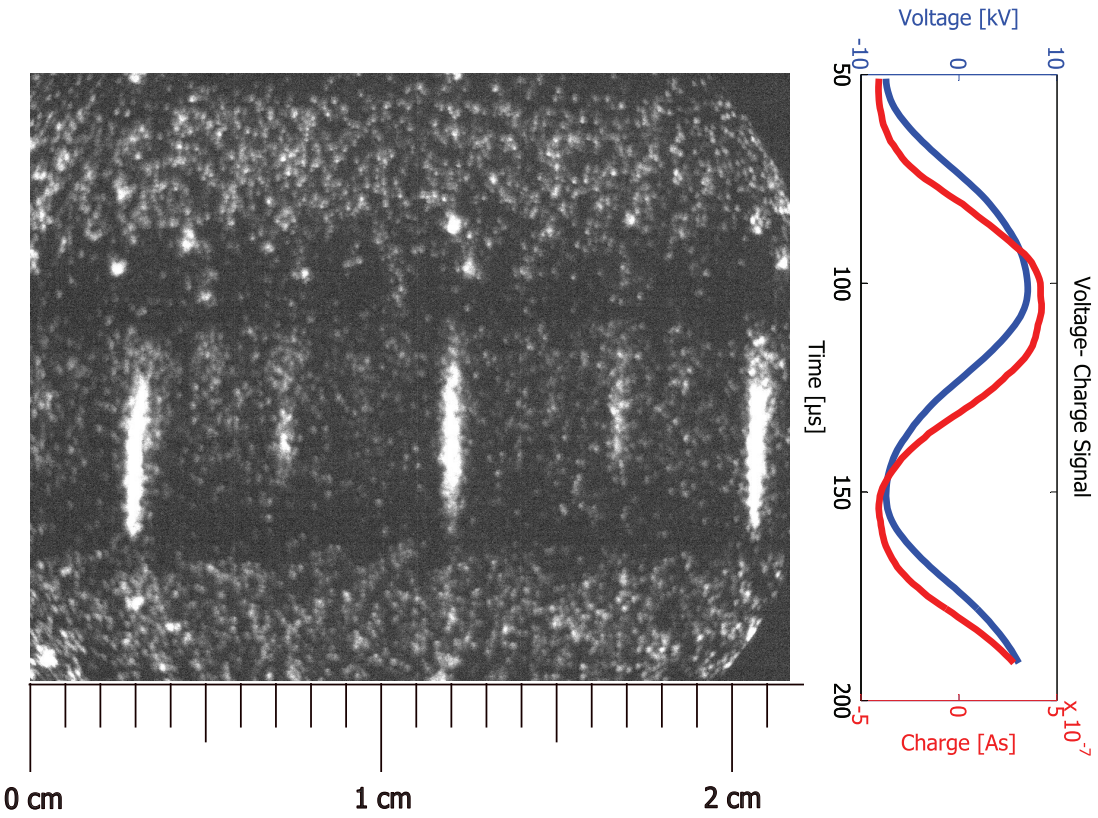

Figure 4.2: Streak camera image of the discharge, slit spanwise. The frequency is 10 kHz, the power consumption 500 Watt. The streak time is 200 μs.

correspond to discharge filaments that span from the edge of the upper electrode downstream towards the lower electrode. Since their duration is significantly smaller than the temporal resolution of the streak camera, they appear as bright spots in the temporal dimension.
There are two limiting factors for the temporal resolution of fact processes, the resolution of the CCD camera and the width of the slit in front of the SSSU. The CCD camera has a resolution of 1280x 1024 pixels. With an effective streak time of 140 μs, each pixel and thus the resolution corresponds to 140 μs/1024 pixel $\approx$ 0.13 μs. The width of the slit is roughly 10 pixels and thus smears the images. Hence, the effective minimal resolution and the upper limit of the discharge duration is roughly 10x 0.13 μs = 1.3 μs. The real duration is most likely significantly less.
It is obvious that the discharge during the positive half-cycle is different from that in the negative half-cycle. The spots are bigger, larger in number and no instabilities occur. This behavior is independent of input power.
Figure 4.3 shows the negative half-cycle of a discharge with a significantly smaller streak time of 50 μs but other-wisely identical parameters. Due to the limitations mentioned above, the screen

only visualizes roughly 35 μs. The spots are clearly visible again, homogeneously distributed in between the instabilities. The spots accumulate within the instabilities and are brighter. The spatial extension of a single instability is roughly 0.75 mm, thus three times the spot width. The spots are as small as the temporal resolution, thus an estimation of the upper limit of the discharge duration can be given to roughly 300 ns. It is clearly visible in the image that the number and density of the

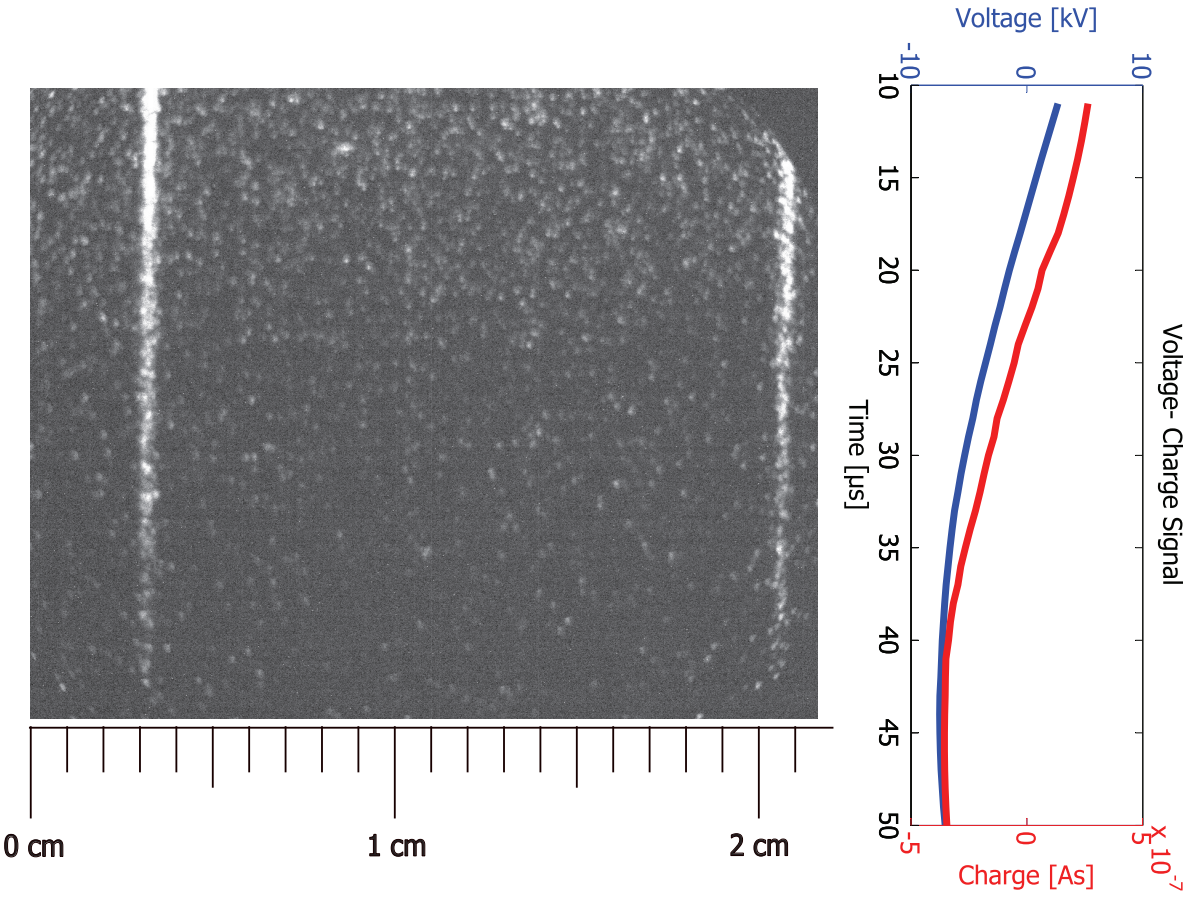

Figure 4.3: Streak camera image of the negative half-cycle of the discharge, slit spanwise. The frequency is 10 kHz, the power consumption 440 Watt. The streak time is 50 μs.

spot varies by time. At high temporal voltage gradients (around t=15 μs), the density significantly exceeds that of low gradients at t=40 μs. Since the number of spots most likely corresponds to the number of discharges and their strength, the overall current transfer during that time is also higher. This is confirmed with the charge development visible on the right side of figure 4.3.
According to the theory, the discharge in the negative half-cycle occurs in the corona regime, as described in section 2.2.3. The duration of a single discharge should be in the order of 100 ns. That is less than the upper limit identified from the images. Thus theory and experiment are in agreement. The image does not yield information about the streamwise structure of the discharge filaments. Those should be made out of the thin cathode layer and a glow-type discharge with a long extension towards the lower electrode. Streamwise images of the discharge will be shown later.

Figure 4.4 shows the image of the discharge in the positive half-cycle. The discharge appears

as being of glow type first (from t = 165 μs to t = 175 μs), with a large number of small spots that are homogeneously distributed. In contrast to the negative half-cycle, no instabilities are visible. Later (from t = 175 μs to t = 200 μs), the number of spots is decreased, but increased in their brightness. The spatial extension of those discharges is roughly 1 mm and hence bigger than those of the negative half-cycle with roughly 0.25 mm. Also, the distance in between them is significantly larger, about 3-5 mm compared to 0.3-1 mm for the negative half-cycle. Obviously, the type of discharge is different from that of the negative half-cycle and changes over time. According to

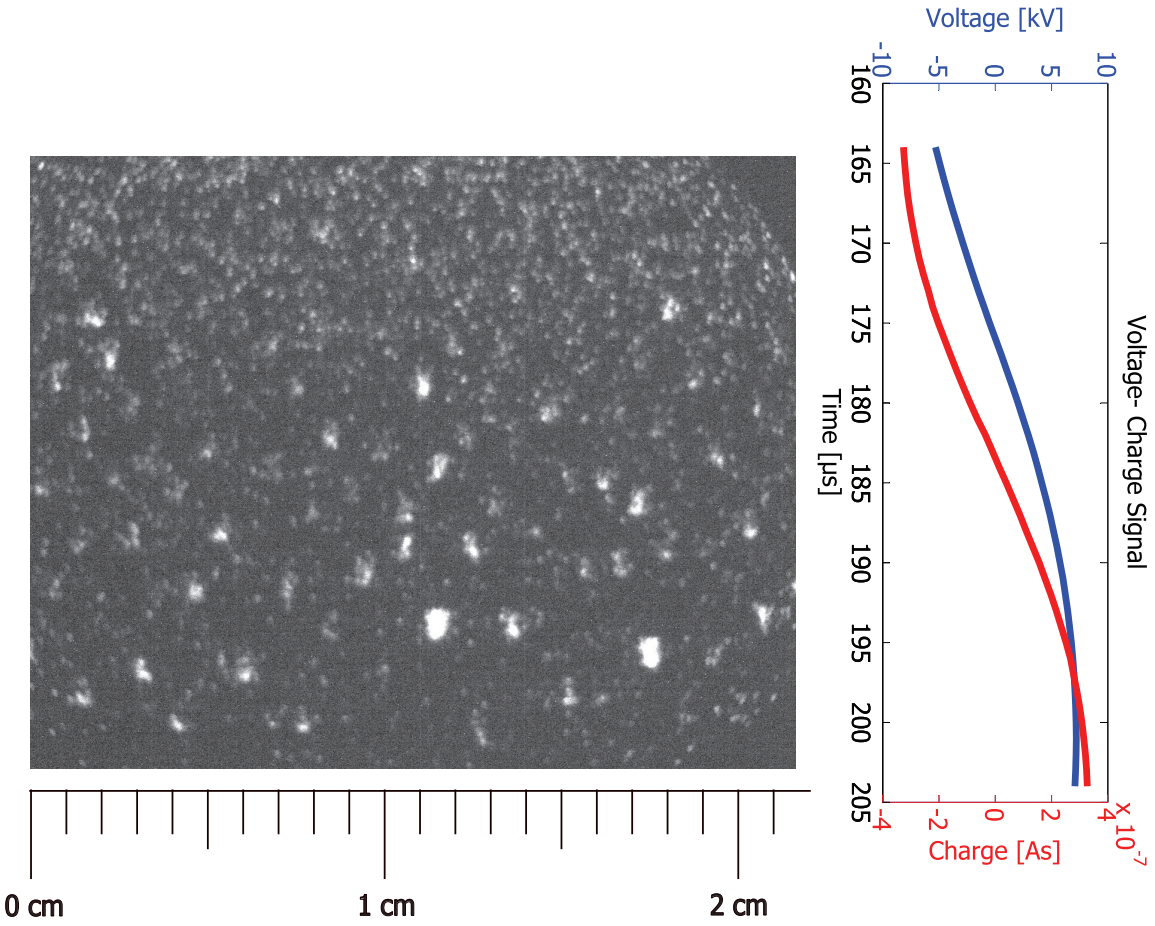

Figure 4.4: Streak camera image of the positive flank' discharge, slit spanwise. The frequency is 10 kHz, the power consumption 440 Watt. The streak time is 50 μs.

the theory of the positive half-cycle, the discharge is supposed to occur in a streamer mode. The discharge duration is supposed to be within a few dozed nanoseconds and is thus in agreement with the estimation of the upper limit determined from the images. Nevertheless, the duration is significantly smaller than the upper limit. Thus, the images yield no information on the temporal composition of a single discharge. The luminosity of the discharge was too small to capture streak camera images at lower streak times.

Due to the random nature of the photo-effect that drives streamers, they should branch out. This is not visible in the images, since the streak camera only shows a line of the image. A two dimensional high-speed camera would be required instead. It can thus not be said whether the discharge in the positive half-cycle is branched or not.

In a second experiment, the slit of the streak camera was mounted orthogonal to the upper electrode. Instead of recording the temporal development of filaments at the upper electrode, the streak camera now shows the growth of the filament length in stremwise direction.. The re-

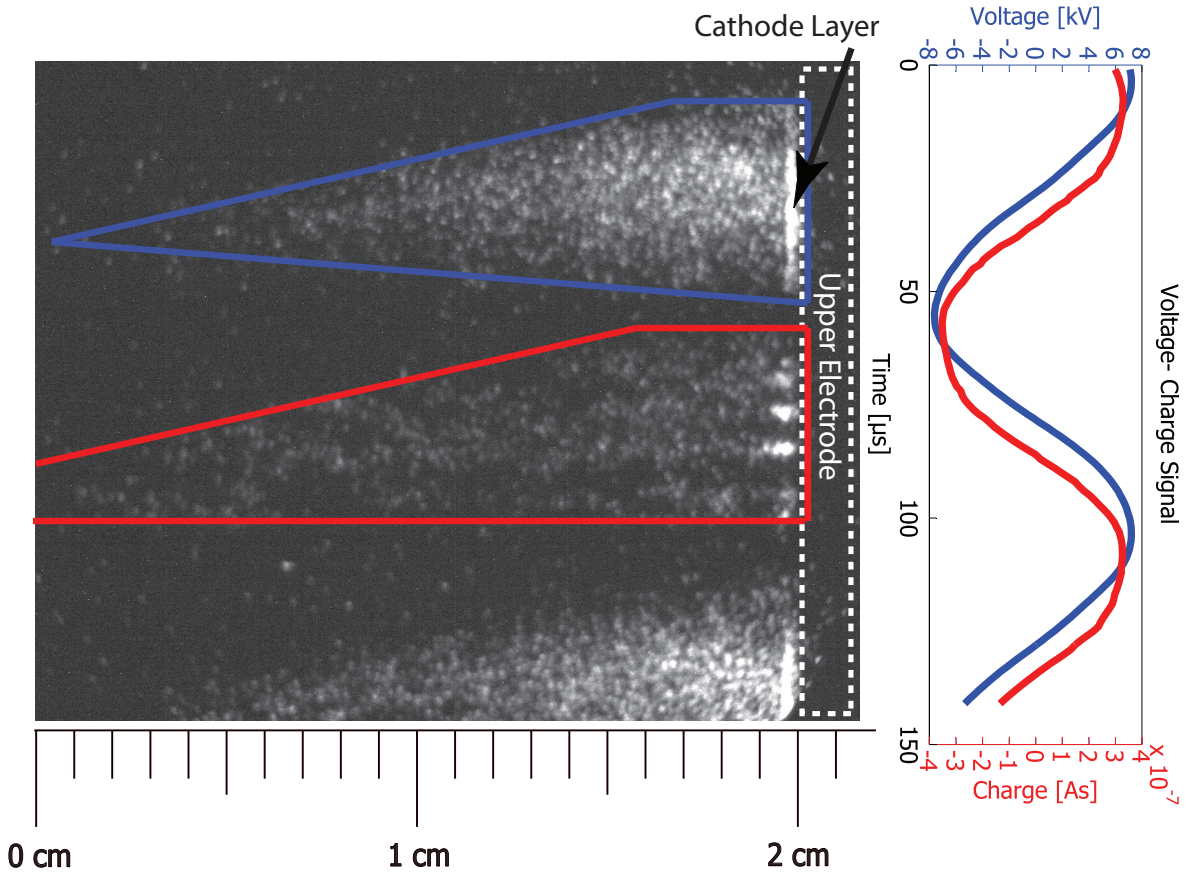

Figure 4.5: Streak camera image of the discharge, slit streamwise. The frequency was 10 kHz, the power consumption 440 W/m. The streak time is 200 μs. The polygons indicate the ranges of the area of discharges for positive (red) and negative (blue) half-cycle.

sults for 200 μs streak time can be seen in figure 4.5. Two negative and one positive half-cycles of the discharge are visible. The polygons indicate the ranges of the discharge zones.

Obviously, the negative discharge is a more homogeneous than the positive and almost continuous, as it was in the first set of experiments. The negative discharge starts when the voltage gradient reaches a critical negative value. The discharge has a minimal discharge length of roughly 3 mm during the first breakdown, as indicated by the blue horizontal line in the image. Afterwards, the discharge length is strictly increasing with a linear growth rate of roughly 0.5 mm/μs. As soon as the voltage growth rate decreases, the growth of the discharge length ends at a maximal extension of 19 mm. Afterwards, the discharge length quickly decreases with a shrinking rate of 2 mm/μs and the discharge ends soon. The cathode layer close to the end of the upper electrode is clearly visible during the negative discharge, as proposed by the theory.

The positive discharge starts as soon as the voltage gradient reaches a critical positive value. Similar to the negative discharge, it has a minimal streamwise length at breakdown voltage.

The minimal length is 4 mm for the positive discharge. It linearly grows with a growth rate of roughly 0.7 mm/μs. Its maximal length is greater than the streak camera slit length. Nevertheless, it can be extrapolated to be roughly 24 mm. When the growth of the voltage amplitude ends, the discharge ends abruptly. In contrast to the negative discharge, the positive discharge seems to be made out of a few (roughly 6 - 10), strong discharges. Close to the upper electrode, they are bright and dense. The luminosity decreases further downstream.
The same observations are made when the steak-time is decreased to 100 μs (effective streak time 70 μs) and the discharges are recorded separately. The resulting images can be seen in the appendix 5.

In summary it can be said, that the high-speed images support the theory presented in chapter 2. A discharge occurs only when the voltage amplitude is strongly increasing or decreasing. When the voltage is minimal or maximal, a dark time without discharges occurs due to the low changes in the voltage amplitude. At high power levels, the discharge is visible in roughly 75% of the cycle period. The discharge in the negative half-cycle is made out of multiple small discharges. The first discharges start with a minimal length of 3 mm from the cathode layer and grow downstream along the lower electrode. The later discharges are longer, thus the discharge zone grows with a rate of 0.5 mm/μs up to a maximal length of 19 mm. Afterwards, the discharge length decreases rapidly. Instabilities occur only in this half-cycle, by the concentration of filaments within a small area.
The discharge in the positive half-cycle also matches the theory quite well. It is made out of few bright filaments, as it is proposed for streamers. The minimal length of the discharge and the growth rate slightly exceed those of the negative discharge. Since the expected discharge duration in both cases is this significantly smaller than the temporal resolution, the experiments are not very meaningful for the temporal behavior of a single discharge. Thus, direct current measurements are necessary and will be described in the next section.

4.1.2 Current measurements

In the following section measurements of the current in a plasma actuator are analyzed with the help of Fourier-transformations in order to get amplitude and power density spectra of the discharge. The spectra help to understand the temporal structure of a single discharge. In the section thereafter, the dependency of the start-time, current amplitude and number of the discharges per half cycle on electric parameters are analyzed. This creates a better understanding of the temporal composition of the discharges for different voltage amplitudes and frequencies.

Amplitude spectrum and power spectral density

The current in the plasma actuator is recorded over 20 cycles. 20 cycles were found to be sufficiently high to get a constant standard deviation and thus reliable results, as will be described

in section 4.1.2. The data is split into the data of negative and positive half-cycle and evaluated separately for all current experiments. First, the maxima and minima of the voltage signal are identified by an algorithm. Then, the current signal of the corresponding positive (from minimum to maximum) and negative (from maximum to minimum) half-cycle were stored in different vectors.
The mean duration of the discharge and its dependency on frequency and voltage gradient are of special interest, since theory demands that the durations are different for streamer and corona discharge, as described in section 2.2.1.

For this purpose, a *Fast-Fourier-Transformation* of the current in a plasma actuator driven with a voltage of 10 kHz frequency is recorded for different voltage amplitudes. The corresponding *single-sided amplitude spectra* were derived for both half-cycles separately (see figure 4.6). The voltage generator used for this measurement was the *MiniPuls 6*. The amplitude spectrum of both half-cycles show distinct peaks for all voltage amplitudes around 38 MHz and 87 MHz. In between the peaks is a broad frequency band. The amplitude spectrum between 100 MHz and 500 MHz shows noise only, independently of the voltage amplitude or frequency. Thus no frequencies greater than 100 MHz occur within the current signal. For that reason the amplitude spectra of all experiments are only shown up to 100 MHz, even though the bandwidth of the experimental setup was 500 MHz.
For low voltage amplitudes, only broadband noise without peaks occurs in the amplitude spectra of both half-cycles. This is due to the fact that the voltage amplitude is too small to produce discharges. When the voltage amplitude is increased, the distinct peaks at 38 MHz and 87 MHz, respectively, occur. This is the case for amplitudes above 4.5 kV in the positive half-cycle and 4 kV in the negative half-cycle. The discharge thus starts earlier in the positive half-cycle than in the negative one. The amplitude spectra are self-similar and show peaks at the same position for different voltage amplitudes. Only the magnitude is increasing with increased voltage. This is probably due to a growing number and amplitude of discharges. The same dependencies can be seen in the corresponding *power spectral density diagrams*(PSD), as in figure 4.7. The magnitude of the PSD goes asymptotically to an upper limit. This limit is approximately given by the diagram of the 10 kV voltage amplitude in the negative half-cycle. All discharges at higher voltage amplitude have an identical PSD. The only exceptions are those of 13 and 13.5 kV. In these cases, the maximum at 87 MHz is shifted to slightly lower frequencies. It could not be clarified yet weather that effect is due to measurement inaccuracies or to a change in the physics at higher voltage amplitudes.
A minor difference in between the PSDs of both half-cycles is that the PSD of the positive flank reaches the asymptotic limit earlier than that of the negative flank, already at 6.5 kV compared to 10 kV. Also, as already mentioned in the amplitudespectrum, the transition of the plasma actuator from a passive element to an active element with discharges starts earlier in the positive half-cycle.

It is to be clarified whether the peaks in the PSD diagram arise due to effects in the discharge or from system response of the experimental setup, such as the *MiniPuls* or the oscilloscope. In order to determine the influence of the voltage generator, the *MiniPuls 6* is replaced by a *MiniPuls 2.1*. The PSD of the discharge in both half-cycles can be seen in figure 4.8.

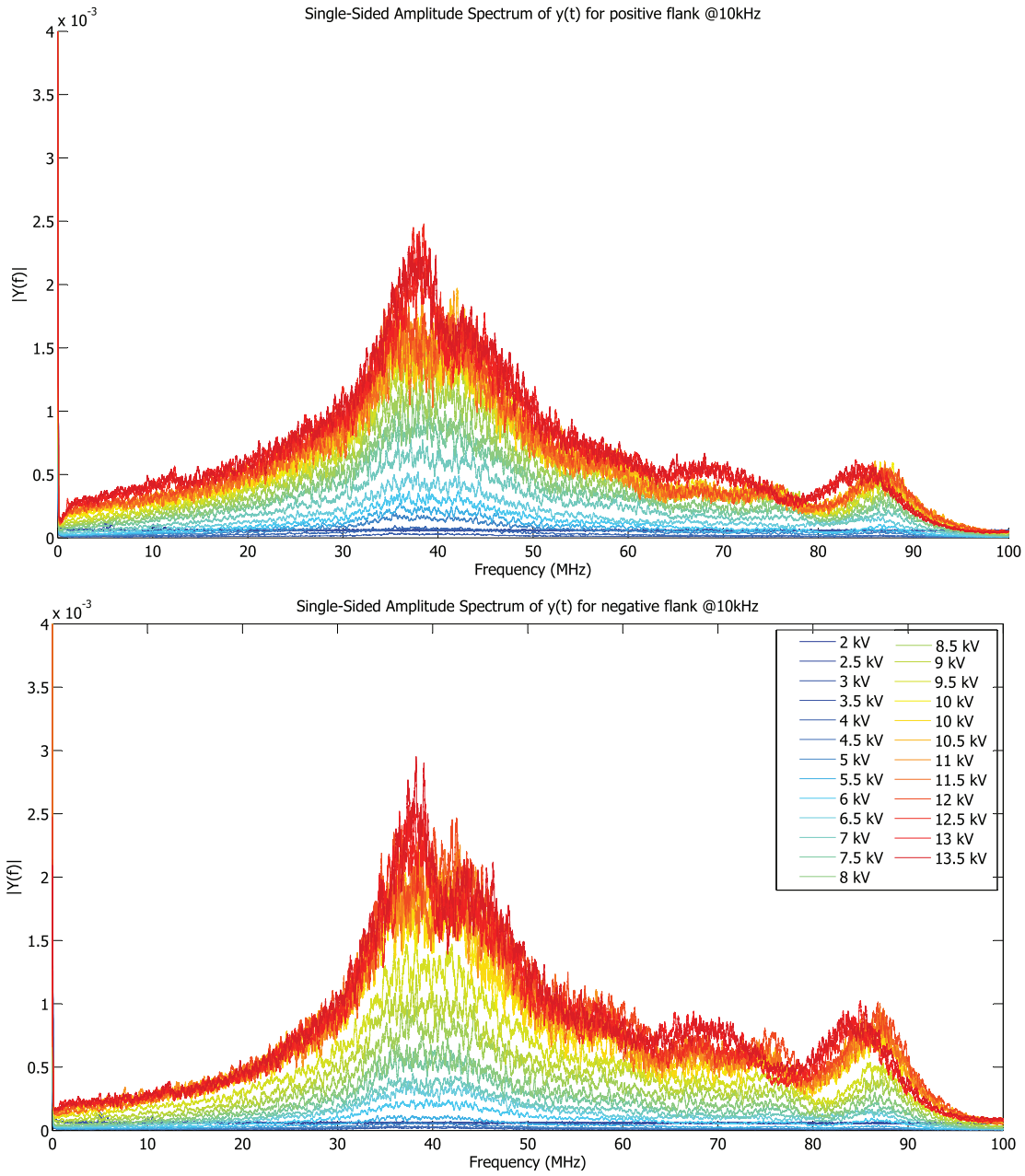

Figure 4.6: Single-sided amplitude spectrum of the positive (top) and negative (bottom) discharge at a frequency of 10 kHz and voltage amplitudes between 2 and 13.5 kV, smoothed with a Savitzky-Golay filter.

It is clearly visible that the peak at 87 MHz moves towards lower frequencies at roughly 70 MHz. In between the two peaks is a plateau of high magnitude. The spectrum almost vanishes above the peak at 70 MHz. Thus, there are no frequencies greater than 70 MHz in the current signal. From these observations it seems likely that the second peak at higher frequencies depends on the chosen voltage generator. The peak thus yields no information on the discharge. It is rather likely that it is a circuit-response to the discharge, such as a reflection of the current signal. Thus, the first peak in the PSD at 38 MHz is more likely to be produced by the discharge. In order to exclude the possibility of an influence by the measurement setup, the *LeCroy oscilloscope* was replaced by a *DSO-X 2004A* by *Agilent Technologies*. The *DSO-X 2004A* has a bandwidth limit

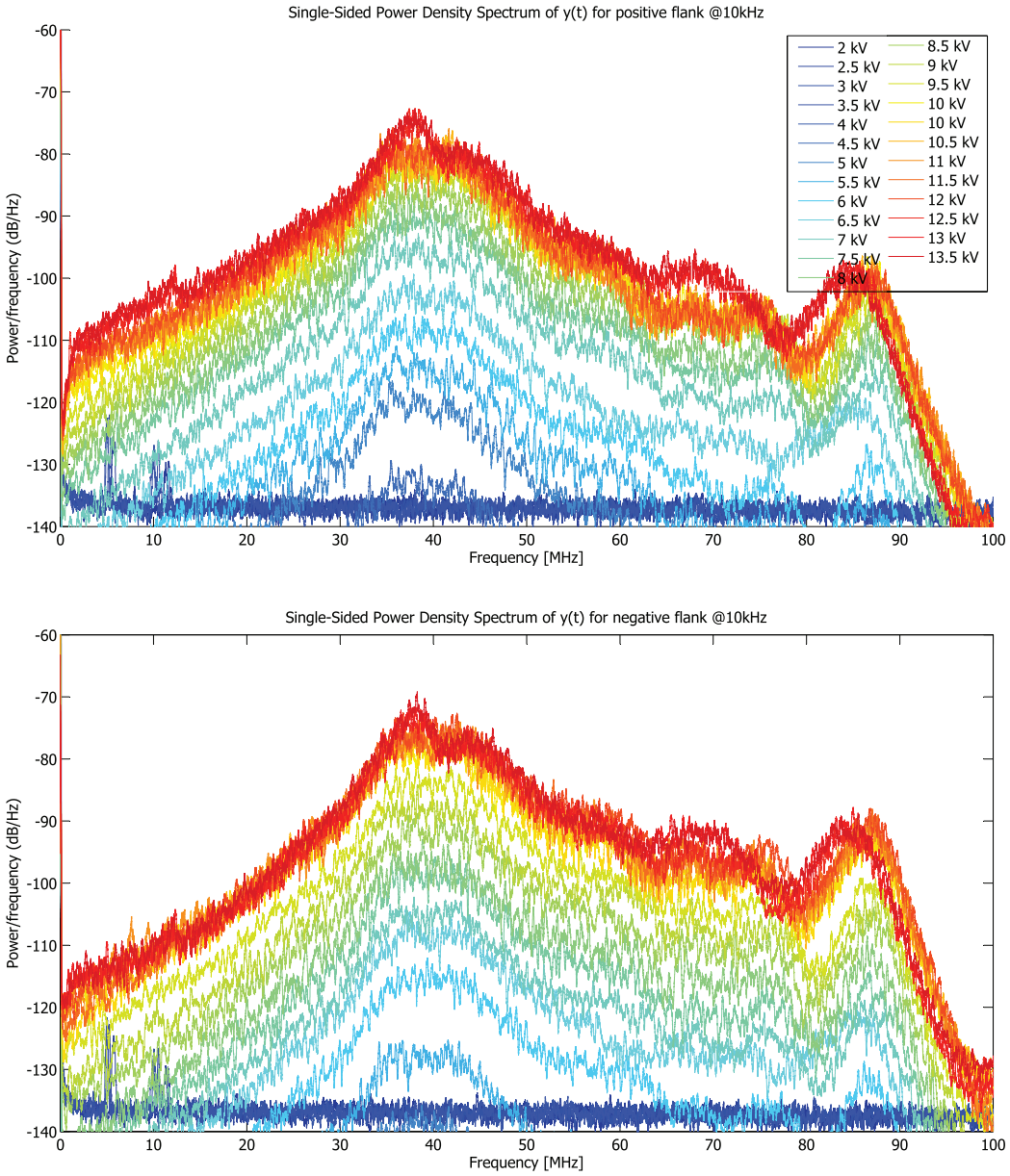

Figure 4.7: Power spectral density of the positive (top) and negative (bottom) discharge at a frequency of 10 kHz and voltages amplitudes between 2 and 13.5 kV, smoothed with a Savitzky-Golay filter.

of 70 MHz, thus it cannot resolve frequencies above 70 MHz. The voltage generation used for this purpose was the original *MiniPuls 6* again. Hence the second peak at 87 MHz should occur again but not be visible, since it is not within the bandwidth of the oscilloscope. The PSD below 70 MHz should be similar to that of figure 4.6

Figure 4.9 shows the results of this measurement for different voltage amplitudes. The frequency peak at 38 MHz is clearly visible, as well as the plateau between 38 MHz and 70 MHz. Above 75 MHz, the density strongly decreases, due to the limit in the bandwidth. The second peak at 87 MHz is thus invisible. The figures show that the PSD and thus the recorded current signal

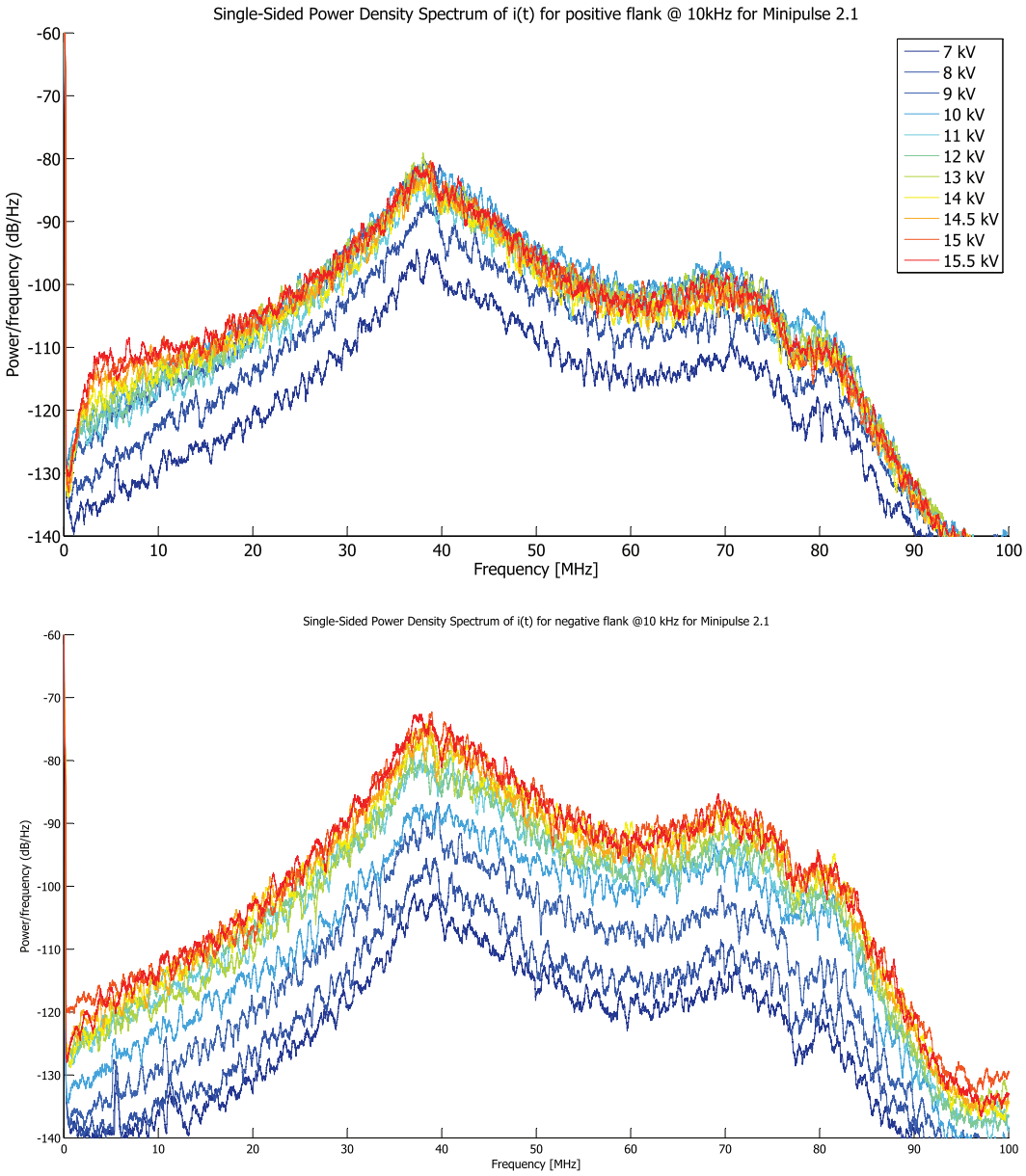

Figure 4.8: Power spectral density diagram of the positive (top) and negative (bottom) discharge at a frequency of 10 kHz and voltage amplitudes between 7 kV and 15.5 kV. In contrast to the previous experiment the voltage generator is a *Minipuls 2.1*.

are independent of the oscilloscope used for the measurement, at least for frequencies below 70 MHz. Since the peak at 38 MHz is independent of the experimental setup, it is likely to be the due to the discharge. That means that the average discharge duration is about $1/(38\ \text{MHz}) = 26$ ns for both half-cycles. Since the time between two discharges without current in the actuator (called *down-time*) is randomly distributed, an "average down-time frequency" is not visible in the PSD or amplitude spectrum. It is of special interest to know on what electric parameters the discharge duration is depending on, and whether or not there is a dependency on the half cycle. Figure 4.7 already indicates that the maximum in the amplitude spectrum at 38 MHz does not change under the variation of the voltage amplitude, since the spectra of all voltage levels have the peak at the

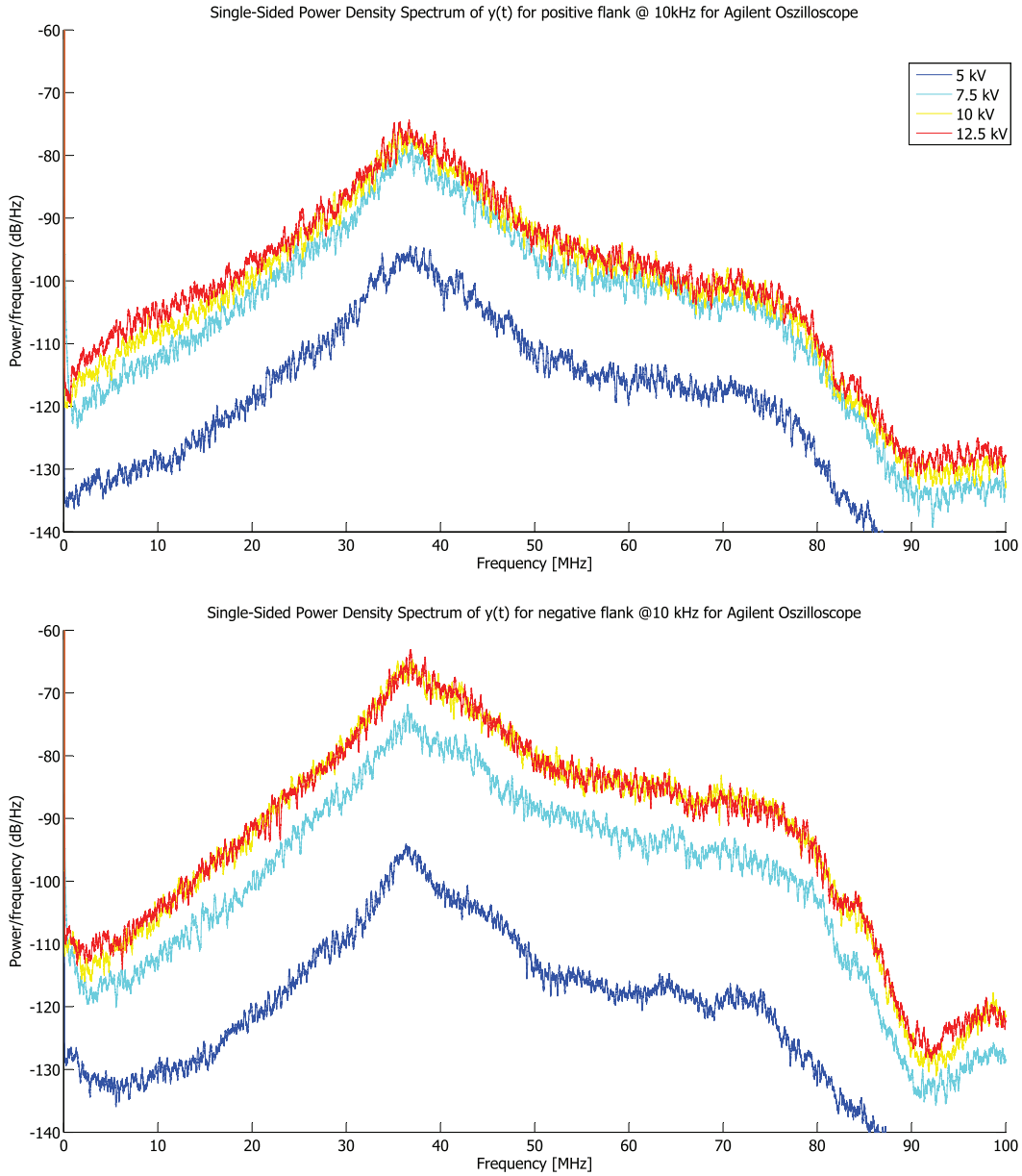

Figure 4.9: Power spectral density diagram of the positive (top) and negative (bottom) discharge at a voltage frequency of 10 kHz and voltage amplitudes between 7 and 12.5 kV. The voltage generator in this experiment is the *MiniPuls 6*. In contrast to the previous experiment the oscilloscope used was an *Agilent DSO-X 2004A*.

same frequency.

Figures 4.7, 5.8 and 5.9 in the appendix 5 show the PSD for discharges at a voltage frequency of 15 kHz und 20 kHz, respectively. The first peak remains at 38 MHz for both frequencies. It is thus evident, that the discharge duration does also not depend on the voltage frequency.

Besides a frequency dependency, it is enlightening to know whether the discharge duration is dependent on the gradients in the voltage. An increase in either voltage amplitude or voltage fre-

quency produces an increase in maximal and the average voltage gradients. Thus, a dependency of the discharge duration on the voltage gradient should already be visible in a variation of the peak with different voltage amplitudes or frequencies. This was obviously not the case, since the maximum of the PSD remained at the same value of 38 MHz. There is the possibility left, that the effects of increasing voltage amplitude and frequency on the discharge duration are reversed by an increasing voltage. In order to exclude this possibility, the data of the measurements of the 10 kHz discharge in figure 4.7 are evaluated separately for different voltage gradients: The discharge cycle is divided into 6 sections, 3 sections for each half-cycle. The sections correspond to phases of 0°- 60°, 60°- 120°, 120°- 180°in the positive and 180°- 240°, 240°- 300°, 300°- 360°in the negative half-cycle. Hence, all sections correspond to different voltage gradients. The current signals are cut into the corresponding six fragments for each of the 20 cycles. Afterwards, an FFT is performed over all 20 cycles together for each section separately. The unavoidable disadvantage of this process is that the signal strength and quality decreases, compared to figure 4.7. This is the case since each fragment contains a smaller number of discharges than the combination of them. The result can be seen in figure 4.10. It is obvious, that the maximum of the PSD remains at 38 MHz (corresponding to a discharge duration of 26 ns) for all voltages and in all sections, even though the voltage gradient is differently for each section. For small voltages, the signal quality is poor due to the fact that only a very small number of discharges occur within that section of the discharge.

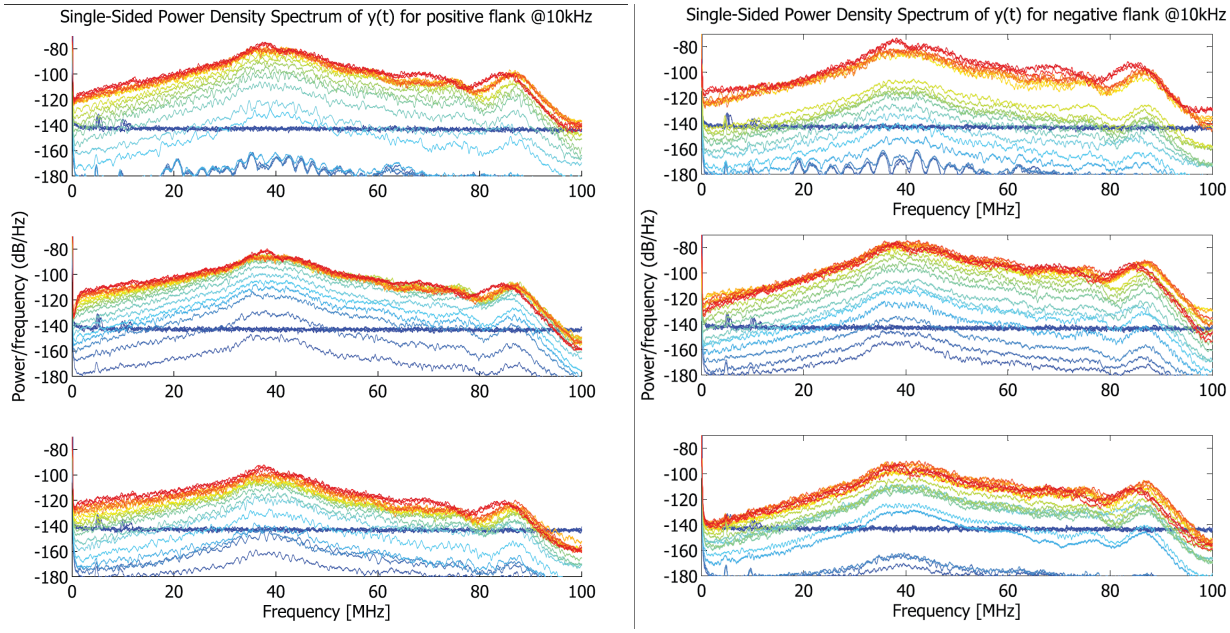

(a) (b)

Figure 4.10: Power spectral density of the discharge in different sections of the cycle at a voltage frequency of 10 kHz. The current signal is divided into 6 sections with different voltage gradients for voltage amplitudes from 2 kV to 14.5 kV. (a) PSD of the sections in the positive half-cycle for a phase of 0°- 60°(top), 60°- 120°(center) and 120°- 180°(bottom) (b) PSD of the sections in the negative half-cycle for a phase of 180°- 240°(top), 240°- 300°(center) and 300°- 360°(bottom).

The peak at 38 MHz persists unvaried for both half-cycles in all experiments. As a result it can be said, that the discharge duration depends neither on the voltage amplitude, nor the voltage frequency, neither the voltage gradient, nor the half-cycle.

Thus a dependency of the discharge duration on any of the voltage parameters is not visible. This fact will be explained in the following:
It can be assumed, that a discharge occurs as soon as the effective electric field, i.e. the difference between the applied electric field E_{ext} and the field of the surface-charge E_{sc}, exceeds the breakdown value $E_{eff} = E_{ex} - E_{sc} > E_{pd}$. This is the same as in the case of a Paschen-breakdown in gases (see section 2.1.2). The discharge increases the electric field of the surface charge by transferring charges. After 26 ns, the effective field is consequently decreased below breakdown value, and the discharge ends since the difference in between the fields is too small to sustain a discharge any longer.
Since the discharge duration is very small, significantly less than the period of the voltage amplitude, the increase of the external electric field within the discharge duration is negligible. Thus, the duration of single discharge does not depend on voltage amplitude, gradient or frequency but on the time necessary to increase the surface-charge field sufficiently only. The number of discharges during one half-cycle and their amplitude should nevertheless depend on the gradients of the external electric field, since the gradients determine how quickly the effective field E_{eff} reaches the breakdown value again after the end of a discharge. This will be discussed in the next subsection.

A variation in the time necessary for building up the surface-charge electric field should thus change the discharge duration. Following that argumentation, a significant change in the actuator geometry should slightly change the discharge duration, since less current needs to be transferred to increase the electric field sufficiently. In a parallel-plate capacitor, the charge transfer necessary to neutralize the externally applied electric field is smaller in a model with low capacitance than for one with high capacitance. Thus, for a plasma actuator with a smaller capacitance, the effective electric field $E_{eff} = E_{ex} - E_{sc}$ should be weakened faster, since less charge needs to be transferred in order to neutralize the external electric field. Following that argumentation, the discharge duration should roughly scale linearly with the passive capacitance of the plasma actuator. The capacitance of a passive plasma actuator can be decreased by increasing the thickness of the dielectric barrier significantly and using a dielectric barrier with lower permittivity. One model of such a plasma actuator is that described by Benard in [16], with thicker (2 mm) dielectric barrier and acryl glass instead of Kapton as dielectric material. Since the barrier is much thicker than that of the asymmetric actuator, the onset voltage for a discharge should be higher. Nevertheless, a higher voltage does not have an influence on the discharge duration, as shown above.
Figure 4.11 shows the PSD of such a plasma actuator. In fact, the discharge duration has decreased, as can be seen in the different position of the maximum. The frequency corresponding to the maximum in the PSD has increased from 38 MHz to 42 MHz, and thus the mean discharge duration decreased to 23.8 ns for all measured voltages.
The capacitance per actuator length of the thin actuator was 100 pF/m, that of the thick actuator 90 pF/m, as measurements with a *HMF2525 LCR-Bridge by Hameg* revealed. Following the argu-

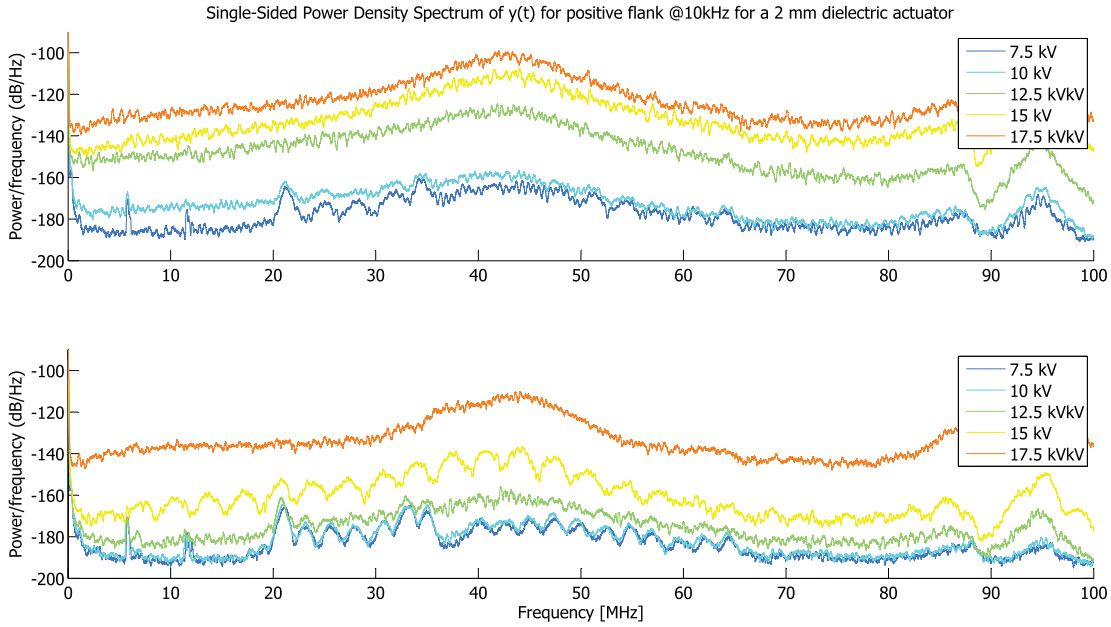

Figure 4.11: Power spectral density diagram of the positive (top) and negative (bottom) half-cycle at a frequency of 10 kHz and voltage amplitudes between 7.5 and 17.5 kV for a plasma actuator with lower capacitance than that of the *asymmetric actuator*

mentation above, the ratio between the two capacitances should be the same as the ratio between the two discharge durations. That is in fact the case, since

$$\frac{C_{thick}}{C_{thin}} = \frac{90\ \text{pF/m}}{100\ \text{pF/m}} = 0.90 \approx 0.91 = \frac{23.8\ \text{ns}}{26\ \text{ns}} = \frac{\Delta t_{thick}}{\Delta t_{thin}}, \tag{4.1}$$

with Δt_{thick} and Δt_{thin} being the discharge duration of the thick and thin barrier actuator design, respectively. The measurements thus support the assumption given above quite well, and it can thus be explained why the maximum in the PSD shifts with significant changes in the actuator design. The independence of the discharge duration on the voltage parameters is thus well explainable.

Nevertheless, it is still surprising that the discharge duration is the same during both half-cycles, independently of voltage amplitude, gradient, and frequency and actuator design. According to the theory of the discharge in DBD plasma actuators, the velocity of the discharge in the positive half-cycle should be about one order of magnitude higher that that of the negative half-cycle. Since the discharge length is approximately the same for both half-cycles, the time for building up the discharge should thus be smaller for the streamer discharge than for the corona discharge. The question is why the discharge durations are indifferent. This could not be completely clarified yet. Nevertheless, a possible explanation is that the velocity of the ion movement is the same during both half-cycles, independently of the discharge regime. Under that assumption, the streamer discharge filament would only built up quicker, but the discharge duration would be the same as in the corona discharge. The same number of charges would need to be transferred to cease the discharge during both half-cycles and thus the discharge duration would be the same, as described

above. Further research is necessary to clarify this correlation.

As shown above, the discharge duration is independent of voltage amplitude, frequency and gradient. Since the power consumption of a plasma actuator is dependent on all these parameters (see Kriegseis [8]), the number of discharges and their amplitude should depend on the voltage parameters, too. During the next subsection, this dependency will be studied.

Current peak analysis

The discharge duration is not the only parameter of interest of the current measurements. The current measurements also allow to identify the moment of discharge and the current amplitude released hereby for all discharges individually, as described in section 3.2.3.

Figure 4.12 shows the mean number of discharges per cycle, their mean amplitude and the time

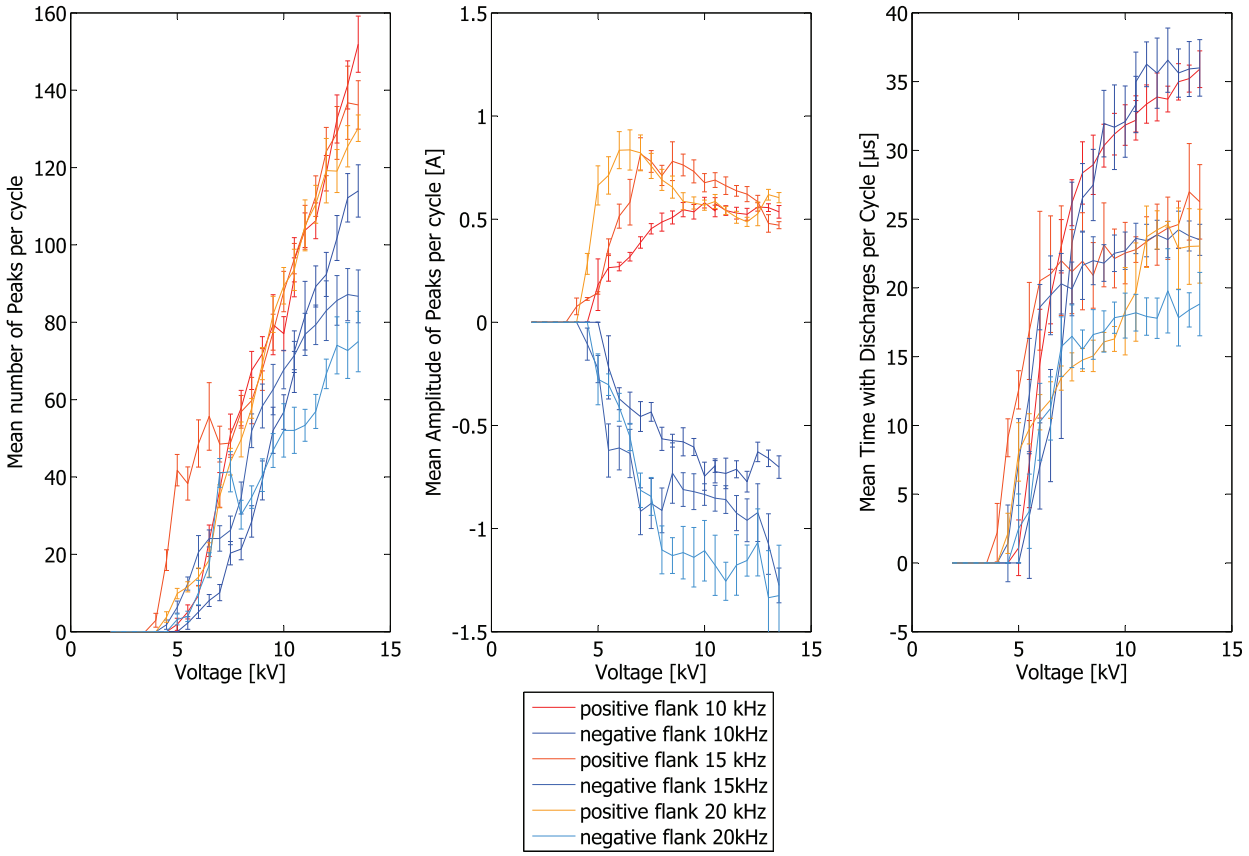

Figure 4.12: Mean number of discharges per half-cycle (left), mean amplitude (center) and time elapsed from the first to the last discharge within a half-cycle for both discharges between 2 kV and 14.5 kV voltage amplitude and frequencies of 10 kHz, 15 kHz and 20 kHz.

elapsed from the first to the last discharge for both half-cycles. These parameters were measured for voltage amplitudes between 2 kV and 14.5 kV and frequencies of 10 kHz, 15 kHz and 20 kHz.

The error-bars in the figure indicate the standard deviation of the parameters within 20 cycles, not the measurement error. For each data-point, the current was recorded over 20 cycles. This number was necessary for a good signal-reliability and a constant standard deviation of the measurements. This is shown in figure 4.13 for an exemplary voltage amplitude of 10 kV and frequency of 10 kHz. The current amplitudes of different discharges are particularly random, as can be seen in the figure, and at least 15 measurements are necessary to receive a constant standard deviation of this parameter. For this reason it is necessary to record at least 20 cycles and average the results over those. The physics of the amplitude distribution will be discussed later. As can be seen in figure 4.13, the standard deviation is quite high due to the random character of the discharge. As figure

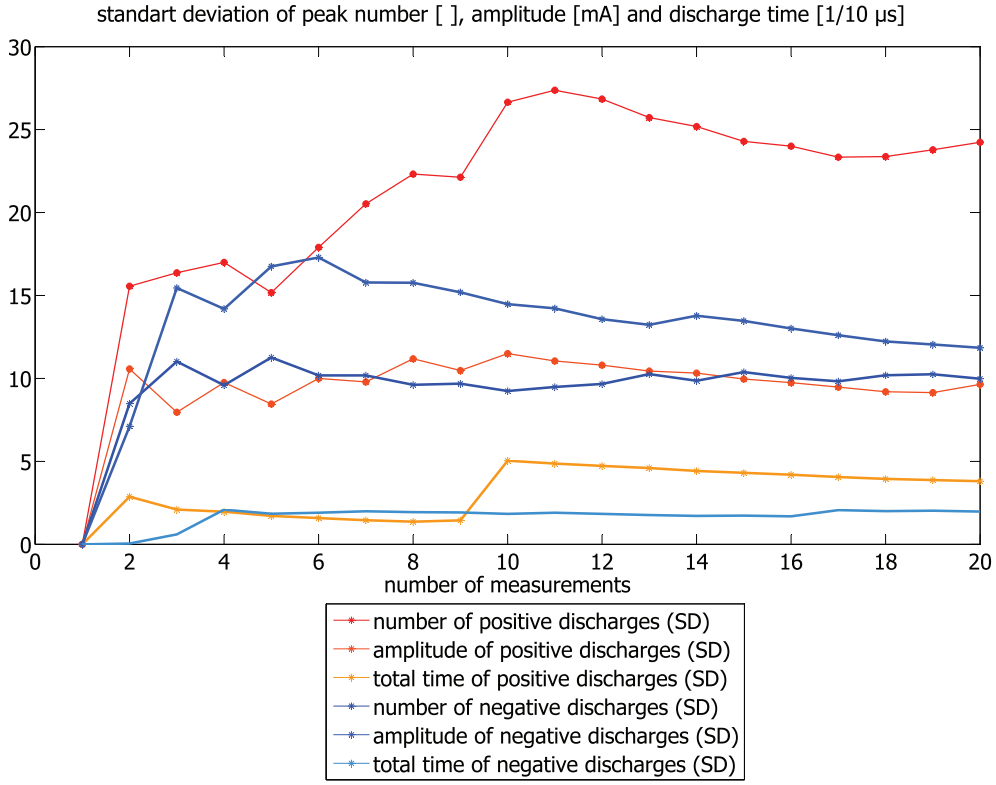

Figure 4.13: Standard deviations of mean discharge number, amplitude and time elapsed from the first to the last discharge within one half-cycle. The voltage amplitude of this exemplary case is 10 kV, the frequency 10 kHz.

4.12 shows, the number of discharges within one half-cycle is strongly rising with increasing voltage amplitude, independently of the frequency. The number of discharges in the positive half-cycle seems to be independent of the voltage frequency, whereas the number of discharges within one negative half-cycle decreases at higher frequencies. The mean number of positive discharges per half-cycle does not show an asymptotical behavior, at least not for the measured voltage amplitudes. The number rises roughly linearly with the voltage. The number of negative discharges, however, has a limit, dependent on the frequency, and is always less than the number of positive discharges for same amplitudes and frequencies. Additionally, it is evident that the onset voltage amplitude for negative discharges is slightly higher than that of positive discharges, as already shown in the previous section.

The absolute value of the mean current amplitude is smaller in the positive half-cycle compared to that of the negative half-cycle. The amplitude of discharges in the negative half-cycle is strictly monotonically increasing with both voltage amplitude and frequency. The amplitude discharges in the positive half-cycle seems to have a frequency-dependent maximum. At 20 kHz, this maximum is distinct and at roughly 6 kV. At lower frequencies, it moves towards higher voltage amplitudes and becomes less distinct. At voltage amplitudes above the maximum the current amplitude seems to have an asymptotical behavior towards 0.5 A for all frequencies. The current in a 20 kHz negative discharge can be thrice as high as that value. Thus, the current amplitude of the negative discharge usually exceeds that of the positive discharge.

Figure 4.12 also shows the mean time elapsed between the first and the last discharge within one half-cycle. It is roughly the same for both half-cycles, but has a dependency on voltage amplitude and frequency. It seems, that the mean elapsed time asymptotically goes to a frequency-dependent upper limit.

More insightful results are achieved when the mean time between the first and last discharge is

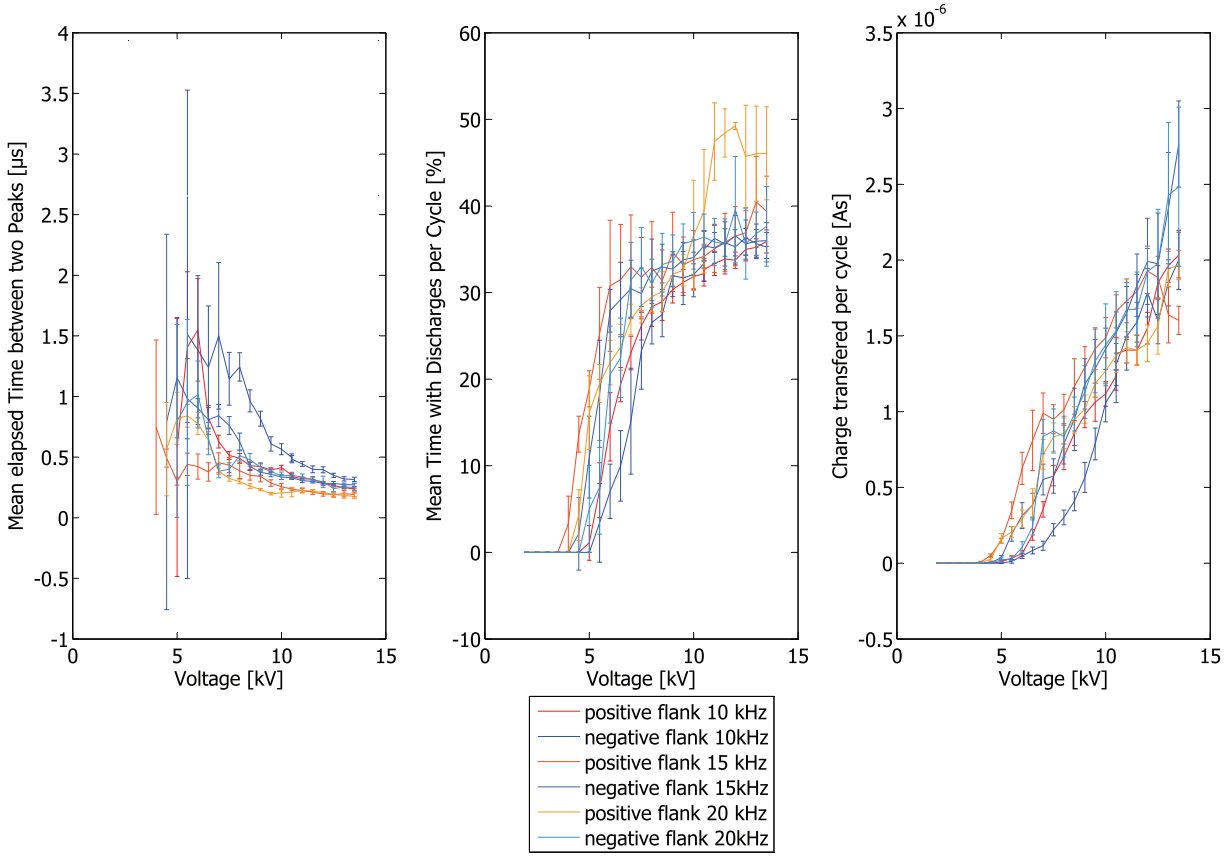

Figure 4.14: Mean elapsed time between two discharges (left), mean duty cycle duration per half-cycle (center) and charge transferred per half-cycle (right) for both half-cycles and voltage amplitudes between 2 kV and 14.5 kV for frequencies of 10 kHz, 15 kHz and 20kHz.

divided by the number of discharges. The result is the mean time between two discharges, the down time, and can be seen for all voltages and frequencies in figure 4.14. The down time seems

to strictly go to a minimal value, the lower limit of down time. This is surprising, since each discharge stochastically occurs at a certain time, but the mean time in between them is obviously independent of half-cycle and voltage frequency at higher voltage amplitudes. The asymptote is given by 0.3 μs for all frequencies. That means that each discharge is followed by a down time of roughly 12 times the discharge duration, on average.

When the time elapsed between the first and the last discharge within a single half-cycle is divided by the duration of this cycle, the mean time with discharges per half-cycle is received. As can be seen in the figure, that value has an asymptotic dependency with an upper limit. The asymptote is roughly 38% cycle duration for both, the negative and the positive half-cycle. Hence, discharges occur in roughly 75% of the cycle time for high voltages, and the dead time is about 25%. The same results were obtained in section 4.1.1, with the help of the streak camera.
Figure 4.14 also shows the absolute value of the charge transferred during one half-cycle. The charge transferred is roughly the amplitude of a single discharge multiplied with the average discharge duration of 26 ns and the number of discharges per half-cycles. As can be seen, the charge transferred is roughly the same for both half-cycles and strongly strictly monotonically increasing with voltage. The transferred charge is, however, roughly independent of frequency, or the frequency-dependency is rather small. These facts explain why Kriegseis [8] did not observe significant differences in the Lissajous-figure of the positive and negative half-cycle. Since the transferred charge per half-cycle is the same for both discharges, no differences of the Lissajous-figures of both discharges occur.

As results of this investigation, it can be said the down time is the same for all discharges at higher voltages, and that discharges occur in 75% of the cycle time. There are more discharges in the positive half cycle, but with a lower amplitude. The charge transferred per cycle is roughly the same for both half- cycles.

Amplitude analysis

As described above, the amplitude of the discharge is highly random. It is interesting to know where this discontinuity comes from. For this purpose, histograms of the amplitude for all voltages amplitudes and both-half cycles were made at first. Figure 4.15 shows a histogram of the discharge amplitude, exemplarily for the positive half-cycle and a voltage amplitude of 10 kV at a frequency of 10 kHz. The amplitude was divided into 30, 60 and 90 bins respectively. The bin size was constant and 1/30, 1/60 or 1/90 of the maximal amplitude length, respectively, for the three histograms. As can be seen, the histogram shows a strictly exponentially decreasing behavior, independently of the total number of bins. The small exaggeration at high current amplitudes of $1.2A$ results from the limitation of the oscilloscope. All discharges with higher amplitude are cut-off at this level, thus the histogram has more values in the highest bins than an exponential behavior would suggest. For this reason, the last values are ignored later on. The slope of the exponential function in the histogram, however, is dependent on the total number of bins, since a higher total number of bins results in a lower number of discharges in each of them.
In order to find a physical explanation of the exponential behavior, the influence of the total number of bins has to be excluded first. Most suitable for this purpose is the *cumulative distribution*

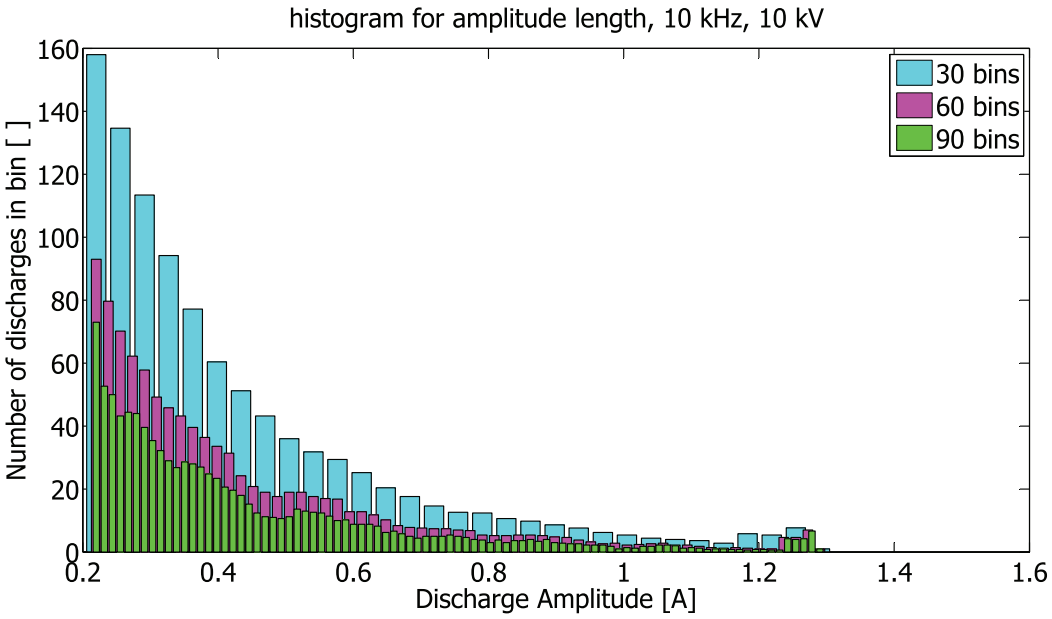

Figure 4.15: Histogram of the current amplitudes of a positive 10 kHz, 10 kV discharge, measured over 20 cycles. The different colors correspond to different total numbers of bins. The bins are constantly distributed from zero amplitude to the highest occurring amplitude.

function (CDF). The CDF describes the probability, that a random variable A with a given probability distribution will be found at a value less than or equal to a, which is the amplitude of the discharges in this case.

$$F_N(a) = P(A \leq a) \tag{4.2}$$

In order to obtain the CDF from the histogram, the numbers of discharges in each bin are summed up. Thus, for a given bin number k with the corresponding amplitude a(k) and number of discharges within that bin N(k), the CFD strength at amplitude A(k) is

$$F_N(A(k)) = F_N(A(k-1)) + N(a(k)). \tag{4.3}$$

Figure 4.16 shows the CDF of the amplitudes of the 10 kV, 10 kHz case. The three lines correspond to the CFDs of the three different histograms. As can be seen, the CDF is independent of the number of bins in the histogram they have been calculated from. Obviously, the CDF has an exponential dependency as well. The dependency can be explained when making the following assumption on the physics of the amplitude in the discharge:

- *For any arbitrary infinitesimal change of the amplitude (dA), has every of the remaining discharges (N(A)), which have not yet ceased at amplitude level A, the same probability λ to end. The number of remaining discharges would thus be reduced by dN.*

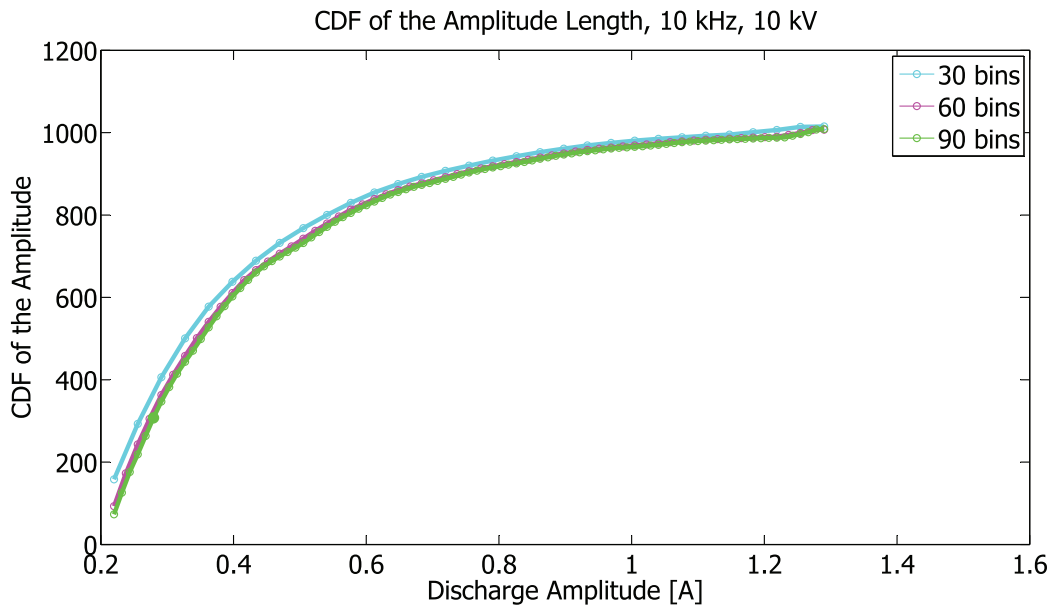

Figure 4.16: CDF of the amplitudes of a 10 kHz, 10 kV discharge for different total number of bins.

That means, that all discharges have the same probability to end within dA, independently of the amplitude the have already reached. Following that argumentation, the reduction of discharges yields to:

$$dN = -\lambda N dA \tag{4.4}$$

This linear differential equation can be solved with the method of separating the variables.

$$\begin{aligned} \frac{dN}{N} &= -\lambda dA \\ \Rightarrow \int_{N_0}^{N} \frac{dN}{N} &= \int_{0}^{A} -\lambda dA \\ \Rightarrow ln\left(\frac{N}{N_0}\right) &= -\lambda A \\ \Rightarrow N(A) &= N_0\, exp(-\lambda A) \end{aligned}$$

The number of discharges thus has an exponential dependency on the amplitude. The corresponding CDF can be derived by integration of the function up to amplitude A:

$$\begin{aligned} F_N(A) = \int_{A=0}^{A} N(A)dA &= \int_{A=0}^{A} N_0\, exp(-\lambda A)dA \\ &= -\frac{N_0}{\lambda}\, exp(-\lambda A) + \frac{N_0}{\lambda} \\ &= \frac{N_0}{\lambda}\,(1 - exp(-\lambda A)) \end{aligned}$$

For discrete values, the CDF is thus

$$F_N(A(k)) = \frac{N_0}{\lambda}\,(1 - exp(-\lambda A(k))) \tag{4.5}$$

That is exactly the behavior of the CDF as can be seen in figure 4.16.
The parameter λ or more precisely its inverse $\tau = 1/\lambda$ is of special interest, since it describes the tendency of the discharge to break off at a certain current amplitude. Small values of τ correspond to low average current amplitudes of the discharges, high values to high average current amplitudes of the discharge. Presumably, τ depends on multiple parameters, like

- voltage amplitude, gradient and frequency
- the half-cycle (positive or negative discharge)
- pressure and temperature of the neutral gas
- velocity of an eventually existing flow of the neutral gas

Thus τ is a parameter to directly investigate the plasma in the discharge, since changes in the parameters above should directly result in changes of the τ- values.
An exponential least-square fit of the CDF yields the value of τ. Figure 4.17 shows τ as a function of voltage amplitude for both half-cycles. The discharge is performed in air under ambient pressure and temperature with an asymmetric actuator design. Since τ is always greater for the negative

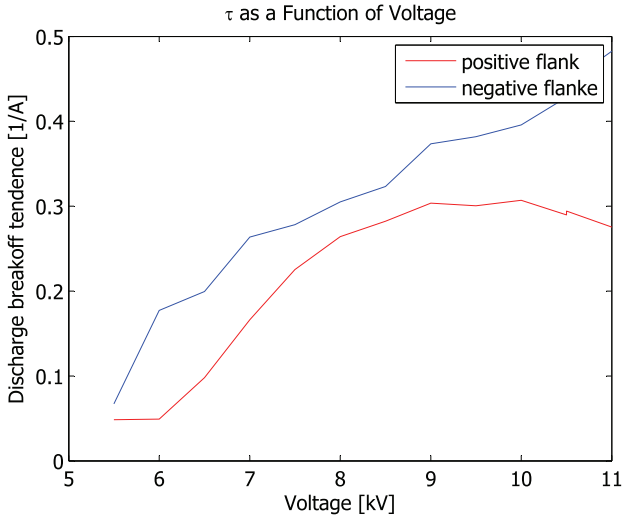

Figure 4.17: τ as a function of voltage for a voltage frequency of 10 kHz.

discharges than for positive, the average current amplitudes in the negative discharge are greater than in the positive.
The dependency on the half-cycle is probably due to the fact that some species in the gas, probably positive ions, supports the discharge in the positive half cycle. The negative discharges have less of such a support, thus the discharge appears less often but with higher amplitude. Further investigations are necessary in order to explain this behavior more precisely.

4.1.3 Conclusions

Both experiments, high-speed streak camera images and current-measurements, showed good agreement with the theory of the dielectric barrier discharge during the positive and negative half-cycle. The discharge is not continuous, but made out of multiple current pulses of a short du-

ration with a down time in between. They only occur at times of increasing or decreasing voltage amplitudes. Time of durations in one cycle is limited to roughly 75%, as both experiments revealed

4.2 Results of experiments on large-scale filaments

Several experiments reveal characteristics large-scale of the filaments. They also support the theory of the filaments being thermal instabilities by confirming eqn. 2.20. The details of the experiments and their results will explained in this section. In the first subsection, the influence of the instabilities on the power consumption is studied. The second subsection describes the changed heat-generation in a plasma actuator through the occurrence of large-scale filaments. In the third subsection. the influence of an external air flow on the large-scale filaments is studied and compared to the theory. An increase in the velocity of the ionic wind in the vicinity of the instabilities is described in the fourth subsection

4.2.1 Power-voltage characteristics

From the theory described in section 2.3 it is assumable that the transition between a stable glow regime and the unstable filamentary discharge (development of filaments) has an influence on the power-voltage characteristics of the discharge, since the process that leads to the instabilities contains a local increase of the electric power density. Thus, the power consumption has to increase at least locally.
Kriegseis [22] observed, that the power consumption of plasma actuators during the stable discharge follows a power law $P = a \cdot U^b$. The exponent b was experimentally determined to be roughly 3.5, independently of the actuator design. Figure 4.22 shows the power-voltage characteristics of a plasma actuator in the asymmetric actuator design for a voltage frequency of 10 kHz. The transition to the unstable discharge occurs at voltages amplitudes above roughly 11.5 kV. An influence is not evident in the characteristics, since the consumption is linear in the double- logarithmic plot during the transition. The slope of the power law in a logarithmic plot is about 3.66 and thus in good agreement with the value given by Kriegseis. According to this measurement, the power consumption dependency on the voltage is not increased during the unstable discharge compared to the stable discharge. Nevertheless, the theory demands that the power released in the filaments is increased and observations show, that the discharge in the instabilities is significantly brighter than in the stable glow. It is thus surprising where the additionally consumed power comes from, since the overall power consumption is not influenced by the instabilities. During the next subsection, this fact will be studied more closely.

4.2.2 Heat generation in instabilities

Measuring the spatial temperature distribution on the dielectric surface in the actuator gives a good insight into the local power consumption, since most of the electric power consumed by a plasma actuator is released into heat, according to Roth [3]). The dissipated power increases the local temperature. In the experiment, the surface temperature of the actuator in quiescent air

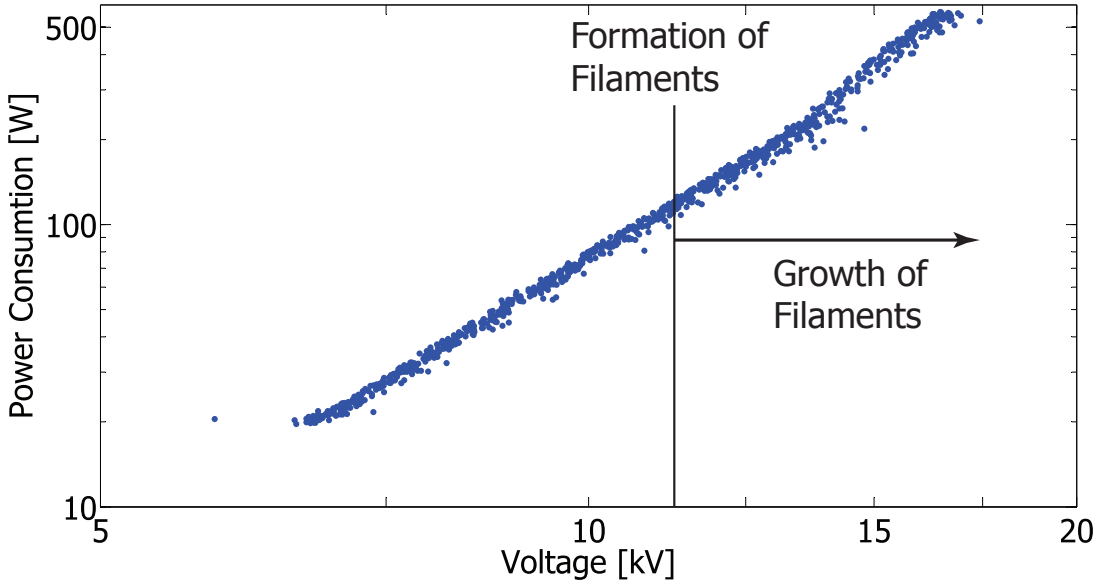

Figure 4.18: Power-voltage characteristics of a plasma actuator in quiescent air for the asymmetric actuator configuration. The discharge becomes unstable at voltages higher than 11 kV.

was captured for different voltage amplitudes. The surface temperature is dominated by the gas temperature, since the heat released within the discharge is the dominant heat source and the heat conduction below the surface is negligible due to the low conductivity of the barrier material. As can be seen in figure 4.19, the instabilities are visible in the heat distribution through a local increase of the temperature. In both the optical and the infrared spectrum, the formation of filaments starts at approximately 11kV.

As can be seen in fig. 4.19 and 4.20, the filaments become hotter, thicker and longer with in-

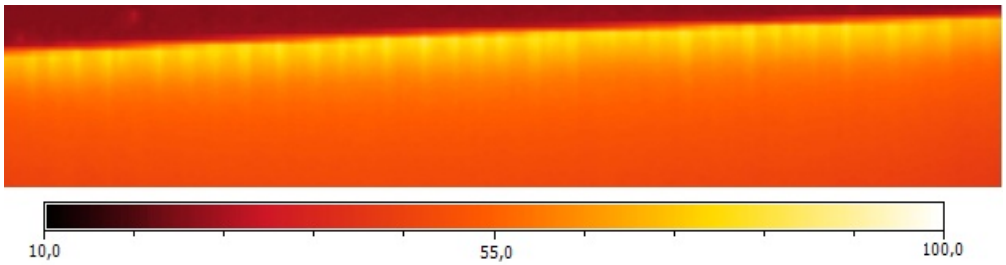

Figure 4.19: Steady state temperature distribution of the actuator surface with a voltage amplitude of 11 kV in quiescent air.

creasing voltage amplitude. The gas temperature within the filaments increases up to 140°C for U=14 kV. The average temperature of the discharge also rises due to the higher consumed power. Fig 4.21 shows the steady state surface temperature difference between the actuator surface and the ambient gas as a function of the voltage amplitude. The surface temperature is constant along the discharge zone for voltage amplitudes below 10 kV, where the discharge is stable. Above 10 kV, the temperature of both the filaments and in the zone of glow discharge in between the filaments is

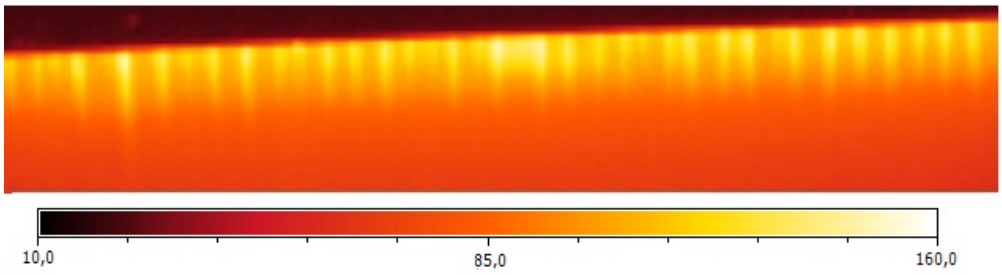

Figure 4.20: Steady state temperature distribution of the actuator surface with a voltage amplitude of 14 kV in quiescent air.

measured separately. Obviously, the temperature is strictly monotonically increasing and the temperature of the filaments always exceeds that of the glow in-between. The temperature difference between the instabilities and the glow zone in-between is increasing with the voltage amplitudes. The surface temperature of the stable glow is extrapolated towards voltage amplitudes with unstable discharges using an exponential fit in figure 4.21. The exponential extrapolation shows a good agreement with the data during the stable discharge, thus an exponential function seems to be appropriate. Extrapolating the function towards higher voltages shows the surface temperature for a discharge without a change in the physics and thus without instabilities. A discharge without instabilities under these voltage amplitudes is only possible if all small perturbations that trigger the unstable process (sharp points in the electrodes, scratches in the dielectric barrier, etc.) are suppressed. Since the perturbations cannot be suppressed in experiments, only in theory, instabilities begin to develop at voltages above 10 kV and the two branches for instability and glow temperature occur. Obviously, the temperature within the filaments always exceeds the value of a hypothetically undisturbed system, whereas the temperature in between the filaments is always lower. The average temperature of the whole surface is approximately equal to the temperature of the undisturbed system for all voltages during the unstable discharge.

As observed in subsection 4.2.1, the power-consumption to voltage amplitude dependency of the discharge does not change during the development of instabilities. The reason for this is now evident: On one hand, instabilities consume more electric power per unit volume than the homogeneous glow through a higher electric current density, as described in section 2.3.3. On the other hand, the electric current density decreases in the space in between the filaments due to lower electron density and the thus higher electric resistance. Therefore, the power consumption and thus the heat generation in between the instabilities are lower than in an undisturbed system. The steps of the unstable process work reverse in the discharge between the filaments.

The discharge concentrates within the instabilities and thus consumes more power, whereas the discharge is decreased in between the instabilities. Thus, no net difference of the power consumption is evident. This effect is becoming more important at higher voltage amplitudes.

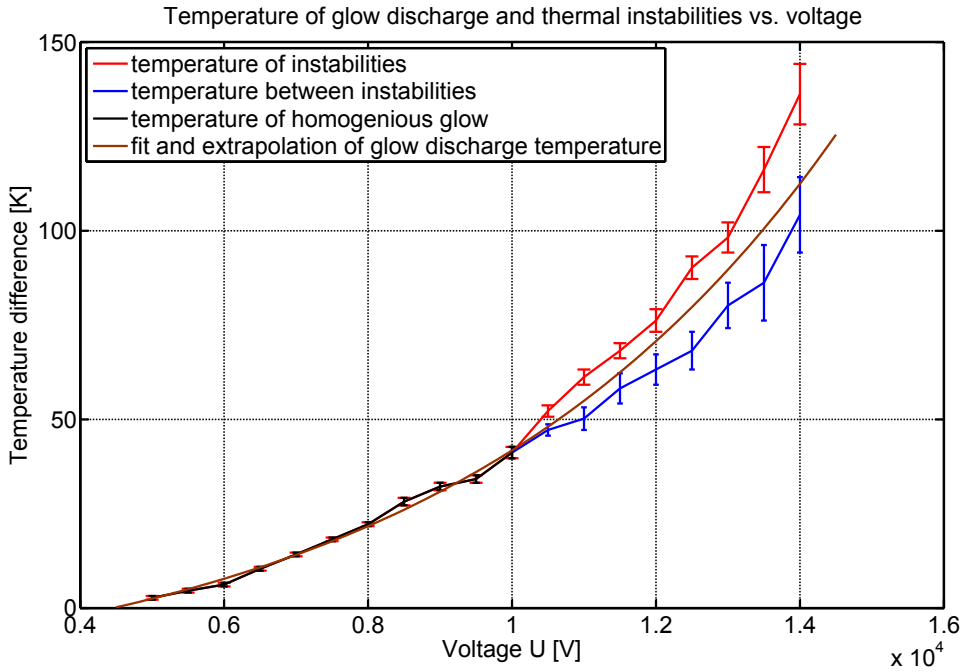

Figure 4.21: Temperature difference between the surface of the actuator and the ambient quiescent air for different voltage amplitudes. Between 4 kV and 10 kV, the glow is stable and homogenous, for higher voltages the temperature was recorded in the filaments and in the space in between. The surface temperature of the stable discharge is extrapolated from 10 kV to 14.5 kV using an exponential least-square extrapolation.

4.2.3 Influence of air flows on instabilities

It is insightful to know whether an external air flow can have an influence on the large-scale filaments. Subsection 4.2.1 showed that the occurrence of an unstable discharge does not have an influence on the voltage dependency of the power consumption of a plasma actuator in quiescent air. The same fact holds for nonzero flow velocities, as can be seen in figure 4.22. Nevertheless, the onset voltage amplitude for an unstable discharge depends on the flow velocity, as the instability equation 2.20 of section 2.3.3 predicts.

$$n_e E^2 > \nu_{dc}/(1+\nu^*)Nc_pT \tag{4.6}$$

The dependency is not evident, but, since the heat removal frequency $\nu_{dc} = \chi/\Lambda_T^2 + 2\cdot u/\Delta x$ is linearly dependent on the flow velocity, the critical electric field is also dependent on the flow velocity. Thus an increase in flow velocity increases the threshold for an unstable development. The threshold follows the law

$$E = \sqrt{\frac{(\chi/\Lambda_T^2 + 2\cdot u/\Delta x)/(1+\nu^*)Nc_pT}{n_e}} \tag{4.7}$$

Most of the coefficients, such as χ, λ and n_e are unknown for the given discharge. Nevertheless, the voltage threshold characteristic should follow a

$$E = a\cdot\sqrt{b+u} \tag{4.8}$$

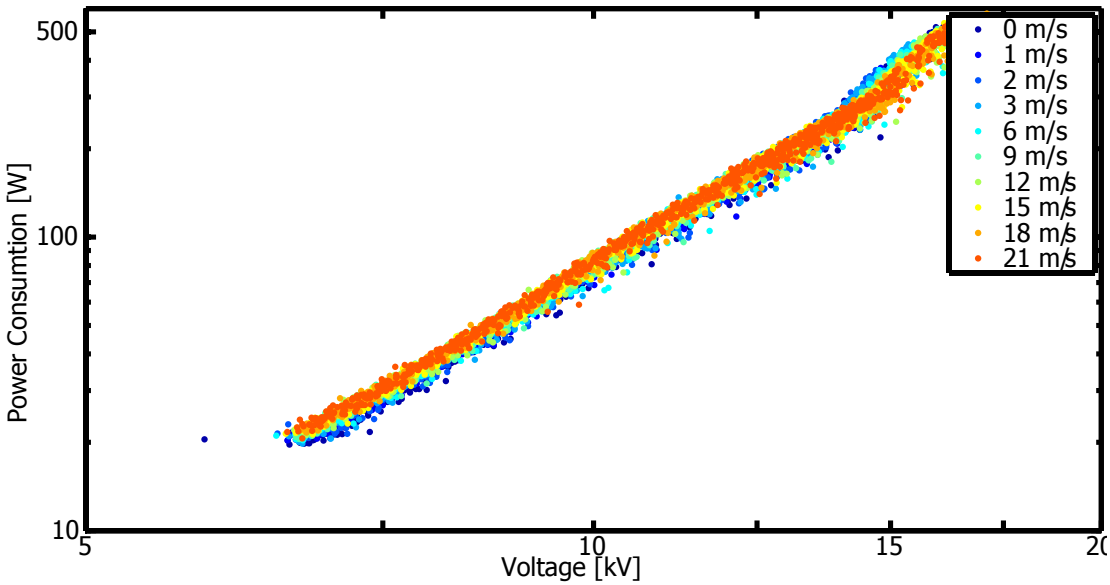

Figure 4.22: Power-voltage characteristics of a plasma actuator in an external flow with various flow velocities. The onset voltages for an unstable discharge range from 11 kV to 15 kV for the different flow velocities.

dependency, with a and b being unknown coefficients. Most importantly, those coefficients are approximately constant for constant actuator geometry and small variations in the temperature and pressure.
When the convective cooling is dominant compared to the diffusive cooling, as it is the case for $u/\Delta x >> \chi/2\Lambda_T^2$, equation 4.8 simplifies to

$$E \approx a \cdot \sqrt{u} \tag{4.9}$$

Fig. 4.23 shows the dependency of the onset voltage for instabilities on the flow velocity for different sizes of instabilities. The actuator electrodes are mounted perpendicular to the flow in this experiment, such that the induced flow of the actuator and the external flow move in the opposite direction. Additional experiments showed the same dependency for different flow orientations. It is hard to define a precise onset voltage for the development of filaments, since the filaments do not appear at a certain voltage, but start to grow from a very small length. Therefore, three different types of instabilities are defined, dependent on their length. Small instabilities have a length less than 2 mm and are very thin, medium instabilities have a length of about 2-6mm and long instabilities a length greater than 6mm. The onset voltage of medium size instabilities is assumed to be the onset voltage of the unstable process, in order to have a more precise definition of the onset voltage. Small-size and long instabilities are assumed to indicate the error of the measurement.
A closer look at the onset voltage-flow velocity characteristic in figure 4.23 shows, that for high flow velocities and thus high convective cooling rates the slope of the function in a logarithmic plot stays almost constant. That means that the exponent of the function is constant.

The exponent has a value of 0.360 $\pm$ 0.088 and is thus in a good agreement with the theory, since equation 4.9 proposes a value of 0.5. Considering that the theory is obtained under strong simplifications, such as assuming the electric field to be homogeneous or the ionic wind velocity

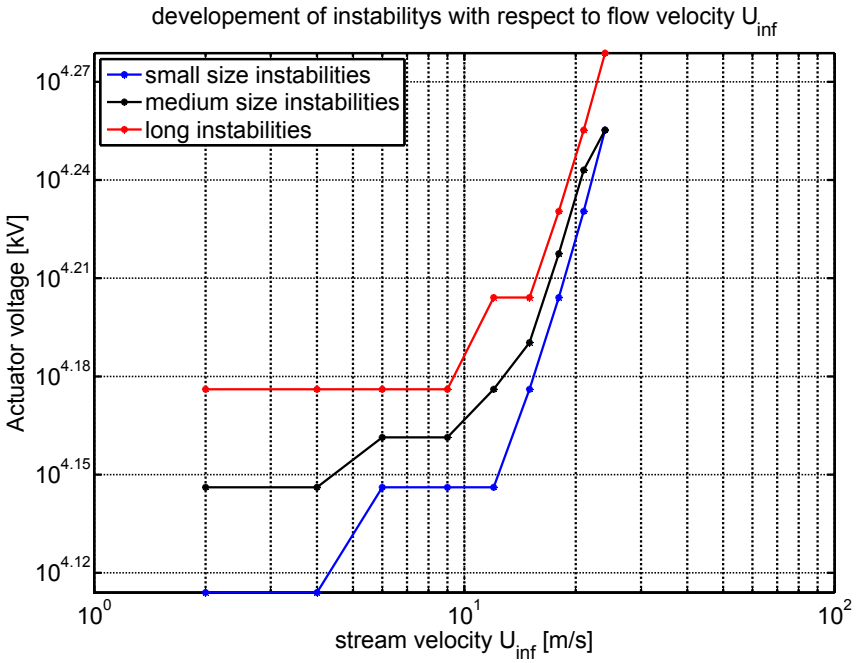

Figure 4.23: Dependency of the onset voltage amplitude for an unstable discharge on the flow velocity in a logarithmic plot

negligible.
This dependency shows a strategy to prevent the most undesired effect of the instabilities when necessary: the fatigue in the dielectric barrier due to high temperature and the highly energetic ions in the instabilities. It is desirable to prevent the instabilities in order to increase the actuator lifetime. According to the measurements, the drop in the lifetime can be prevented when the actuator is only used in external flows with a high wind velocity, such that the instabilities are prevented.

In the following subsection, the dependency of the ionic wind velocity on the instabilities will be measured.

4.2.4 Influence of instabilities on the ionic wind

The velocity of the ionic wind was measured in instabilities and the glow zone in between the instabilities separately using a *Setra Static Pressure Probe, Model 267*, as described in subsection 3.3.3. The voltage amplitude was set to 15 kV at 10 kHz frequency. After several measurements it turned out, that the velocity of the ionic wind in the glow zone between the instabilities ranges from 5.2 m/s to 6.1 m/s, whereas it ranges from 6.7 m/s to 7.2 m/s within the instabilities. The ionic wind velocity thus clearly exceeds that of the space in between. Therefore, the flow produced by a plasma actuator with an unstable discharge is three dimensional. This has to be taken into account in future flow-control strategies.

4.2.5 Conclusions

The experiments on the nature and behavior of large-scale filaments in the discharge of plasma actuators showed a good match to the theory. As the theory predicted, the current density and thus the power dissipation in the vicinity of the filaments is increased, whereas it is decreased in the space in between. Since the overall power consumption dependency remains untouched from the instability process, it is assumable that both effects cancel each other out.
Experiments proved that an external flow can delay the unstable process towards higher voltage amplitudes. The dependency basically follows that predicted by the theory. It was also shown, that instabilities increase the velocity of the ionic wind. This has to be taken into account in flow control and might open up new flow control strategies, such as boundary control by vortices.

5 Conclusions and outlook

This work clearly shows that the discharge in DBD plasma actuators is made out of two kinds of filaments, micro-scale and large-scale filaments. Theoretical models for both filaments were developed and presented. Experiments supported and expanded these models.
For micro-scale filaments, high-speed streak camera images and current measurements were taken. These experiments showed good agreement with the theory of the dielectric barrier discharge during the positive and negative half-cycle. The discharge is not continuous, but made out of multiple current pulses of a short duration with a down time in between. They only occur at times of increasing or decreasing voltage amplitudes. The total number and current amplitude of those individual discharges are highly random, but can be measured over a high number of measured discharge-cycles. The general tendency is that number and amplitude rise with increasing voltage, but the down time in between two discharges and the maximal transferred charge are limited. Also, the relative duty cycle of the discharges is limited to roughly 75% cycle duration, as both experiments revealed. A newly developed model of the current amplitude distribution showed significant differences in the behavior of the negative and positive discharge, most likely due to the different kinds of species generated during the discharge. These are mostly N_2^+ ions in the positive and O^- ions in the negative discharge.
Large-scale filaments were identified as thermal instabilities that occur through an unstable process chain. It was shown that the measured spatial structure of the heat generation in the discharge matches the predicted stucture, estimated by the process chain, quite well. The power dissipation and thus the temperature in the vicinity of the filaments are increased, whereas decreased in the space in between. The overall power consumption remains independent of the filaments in quiescent air as well as exposed to external airflow. The model led to an instability criterion. The dependency of the criterion on the flow velocity was compared to experimental results and revealed to be in good agreement. Finally, it was shown that the velocity of the ionic wind in the wake of the filaments exceeds that of the stable glow discharge.

It is planned to continue the investigations on large-scale filaments in a second master thesis. The aims hereby are to investigate the dependency of the onset voltage amplitude on pressure and temperature as well as frequency. Also, the dependency of the typical distance in between the filaments on these parameters will be studied. For this purpose, new actuator designs have to be developed in order to withstand the fatigue of the barrier through the discharge as well as high and low temperatures. It is also planned to study the applicability of large-scale filaments to future flow-control strategies.
In future work, the influence of environmental conditions on micro-scale filaments should also be studied in further detail.

Bibliography

[1] Fomin, de Roquefort, Lebedev and Ivanchenko, *Supersonic flows with longitudinal glow discharge*, Proceedings of the 3rd Workshop on Magneto-plasma Aerodynamics, Moscow (Russia), 2001

[2] Roth,Xin Dai, *Optimization of the Aerodynamic Plasma Actuator as an Electrohydrodynamic (EHD) Electrical Device*, 44th AIAA Aerospace Sciences Meeting and Exhibit, AIAA 2006-1203, Reno, Nevada, USA 2006

[3] J. R. Roth, R. C. M. Madhan, M. Yadav, et al, *Flow field measurements of paraelectric, peristaltic and combined plasma actuators based on the one atmosphere uniform glow discharge plasma (OAUGDP TM)*, Proceedings of the 42th Aerospace Sciences Meeting and Exhibit, Reno (USA), 2004

[4] Kogelschatz, U., Eliasson, B., Egli, W., *From ozone generators to flat television screens: history and future potential of dielectric-barrier discharges*, Pure Appl. Chem., Vol. 71, No. 10, pp. 1819-1828, 1999

[5] Li, Y., Zhang, X., Huang, X., *The use of plasma actuators for bluff body broadband noise contro*, Experiments in Fluids, 2010

[6] Jukes, N., Choi, K., Johnson, G.A., Scott, S. J., *Turbulent drag reduction by surface plasma through spanwise flow oscillation*, 3rd AIAA Flow Control Conference, volume 3, San Francisco, California, June 2006

[7] H. Kegel *Plasmaphysik: Eine Einführung*, ISBN-10: 354063701X, Springer Berlin Heidelberg, 1. Auflage, Germany, 1998

[8] Kriegseis, Jochen; "*Performance Characterization and Quantification of Dielectric Barrier Discharge Plasma Actuators*", Dissertation, Germany, 2011

[9] Raizer, Yuri P. *Gas Discharge Physics*, Springer-Verlag, Germany, 1991

[10] Paschen, Friedrich, *Ueber die zum Funkenübergang in Luft, Wasserstoff und Kohlensäure bei verschiedenen Drucken erforderliche Potentialdifferenz*, Dissertation, Ann. Phys., 273: 69 - 96. doi: 10.1002/andp.18892730505, 1889

[11] Penning, Frans M., *Über den Einfluss sehr geringer Beimischungen auf die Zündspannung der Edelgase*, Zeitschrift für Physik 46,335, Germany, 1928

[12] Roth, J.R., *Industrial Plasma Engineering; Volume 1: Principles*, IOP, 1995

[13] Becker, Kogelschatz,Schoenbach and Baker, *Non-equilibrium Air Plasmas at Atmospheric Pressure*, Series in Plasma Physics- Institute of Physics Publishing, 2005

[14] Meek,J. M., Craggs, J. D. , *Electrical breakdown of gases*, Clarendon Press, 1953

[15] Pavon, Dorier, Hollenstein, Ott, Leyland *Effects of high-speed airflows on a surface dielectric barrier discharge*, J. Phys. D: Appl. Phys. 40 1733 - 1741, Switzerland, 2007

[16] Bernard, N., Moreau, E., *Effects of Altitude on the Electromechanical Characteristics of a Single Dielectric Barrier Discharge Plasma Actuator*, AIAA Plasmadynamic and Laser Conference Paper, USA, 2010

[17] Orlov, Font, Edelstein, *Characterization of Discharge Modes of Plasma Actuators*, AIAA Journal, 46(12):3142 - 3148, USA, 2008

[18] Korolev, Mesyats, *Physics of pulsed breakdown in gases*, UROPress, 1998

[19] Moreau, Eric *Airflow control by non-thermal plasma actuators*, J. Phys. D: Appl. Phys. 40 605, 2007

[20] Pavon, Samantha *Interaction Between a Surface Dielectric Barrier Discharge and Transonic Airflows*, PhD - Thesis N° 4201, EPFL, Switzerland, 2008

[21] http://www.mpg.de/656933/zoom.jpeg , date: 3/19/2012, 16:03

[22] Kriegseis, Benjamin, Grundmann,Tropea, "*Capacitance and power consumption quantification of dielectric barrier discharge (DBD) plasma actuators*", Journal of Electrostatics 69 (2011) 302e312, 2011

[23] Wu, Yun; Li, Yinghong; Jia, Min et al "*Influence of operating pressure on surface dielectric barrier dischaerge plasma aerodynamic actuation characteristics*", Air Force Engineering University Xi'an and Tshinguan University, Bejing, Peoples Republic of China, Applied Physics Letters 93,031503, 2008

[24] Soloviev, V.R., "*Analytical estimation of the thrust generated by a surface dielectric barrier discharge*", Moscow Institute of Physics and Technology, IOP Publishing, Russia, IOP Publishing, doi 10.1088/0022-3727/45/2/025205, 2012

[25] Choi, Jai Hyuk; Lee, Tae Il; Han, Inho et al. "*'Investigation of the transition between glow and streamer discharges in atmospheric air*"', Yonsei University, Seoul, Institute of Physics Publishing, Plasma Sources Science and Technology, doi 10.1088/0963-0252/15/3/017, 2005

[26] Benard, Nicolas; Pons, Jerome; Audier, Pierre et al. "*'Filaments in a Surface Dielectric Barrier Discharge operating in Altitude Conditions*"' IEEE Transactions on Plasma Science, Volume 39, No. 11, November 2011

[27] Forte, M; Jolibois, J; Pons, jerome et al. "*'Optimization of a Dielectric Barrier Discharge Actuator by stationary and non- stationary Measurements of the induced flow Velocity; application to airflow control*"'Exp. Fluids No. 43, 917-28, 2007

[28] Leonov, S.; Opaits, D.; Miles, R and Soloviev, V "*'Time resolved measurements of plasma induced momentum in air and nitrogen under dielectric barrier discharge actuation*"', Phys. Plasmas No. 17, 113505, 2010

[29] Brauer, I.; Punset, C.; Purwins, H.-G,; Boef, J.P., "*'Simulations of self-organized filaments in a dielectric barrier glow discharge plasma*"', journal of applied physics Volume 85, Number 11, 1999

[30] Meek, J. M.; Craggs, J.D., "*'Electrical Breakdown of Gases*"', John Wiley & Sons Ltd, ISBN - 10: 0471995533, 1978

[31] Velikhov, E. P.; Golubev, V. S.; Pashkin, S. V., "*'Glow discharge in a gas flow*"', Sov. Phys. Usp. 25 340-358, 1982

[32] Chirokov, Alexandre V., "*'Stability of Atmospheric Pressure Glow Discharges*"', PhD Thesis, Drexel University, 2005

[33] Lagmich, Callegari, Pitchford and Boeuf, "*'Model description of surface dielectric barrier discharges for flow control*"', J. Phys. D: Appl. Phys. 41 (2008) 095205 (10pp), 2008

[34] Ashpis, David; Laun, Matthew and Griebeler, Elmer "*'Progress toward Accurate Measurements of Power Consumtion of DBD Plasma Actuators*"', AIAA 2012–0823, 2012

[35] Grundmann, Sven and Tropea, Cameron, "*'Experimental transition delay using glow- discharge plasma actuators*"' Technische Universität Darmstadt, Germany, Experiments in Fluids Volume 42, Number 4 (2007), 653- 657, DOI: 10.1007/s00348- 007- 0256- 8, 2007

[36] Kriegseis, Jochen; Schröter, D; Grundmann, Sven and Tropea, Cameron, "*'Online-characterization of dielectric barrier discharge plasma actuators for optimized efficiency of aerodynamical flow control applications*"' Technische Universität Darmstadt, Germany, Journal of Physics: Conference Series No. 301, doi:10.1088/1742-6596/301/1/012020, 2011

Appendix

Appendix A: Determination of the power consumption of plasma actuators

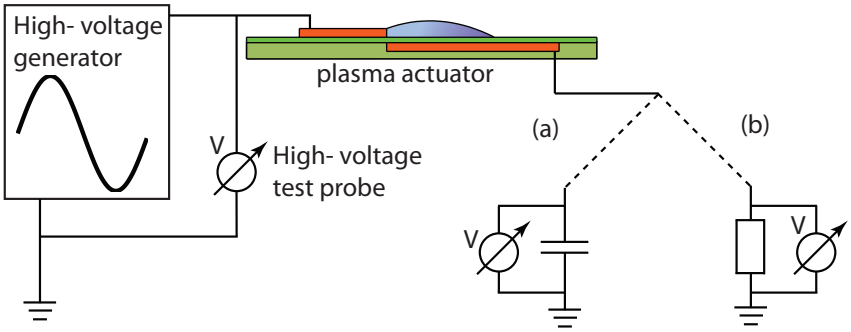

Figure 5.1: Circuit diagram for power consumption determination with (a) measuring the charge flowing through the actuator in a capacitor or (b) measuring the current through the actuator with a test resistor.

The power consumption of the DBD plasma actuators is an essential parameter to compare different operation states. Nevertheless, it cannot be measured directly. The common way to determine the consumption is to measure the electrical input power of the actuator. One possible option is to measure the input- voltage $U_{HV}(t)$ with a high-voltage test probe and the current $I_p(t)$ through the actuator. The current is determined with the help of a probe resistor in series with the actuator by measuring the voltage drop $U_p(t)$ across the resistor (see fig. 5.1 (b)). The power consumption can then be determined by

$$P(t) = U_{HV}(t) \cdot I_p(t) = U_{HV}(t) \cdot \frac{U_p(t)}{R_p}, \tag{5.1}$$

with R_p being the resistance of the probe resistor. Unfortunately, the discharge is made out of short pulses of high current with a duration of a few nanoseconds, as shown in section 2.2. Only expensive oscilloscopes have a sample rate sufficiently high to resolve those current peaks. Without those oscilloscopes, major errors in the current measurement occur. Additionally, reflections of the high-current pulses within coils and wires lead to large errors in the determination of the power consumption. The common way is thus to measure the voltage drop across a probe capacitor instead of an resistor (see fig. 5.1 (a)). The voltage (multiplied with the probe capacity) then gives the charge Q(t) that flowed through the actuator. Since

$$Q(t) = \int_{-\infty}^{t} I_{pr}(\bar{t}) d\bar{t} \tag{5.2}$$

the capacitor integrates over all peaks, a high sample rate and band width oscilloscope is unnecessary. For further information on the comparison of the resistance and capacitance measurements see Ashpis [34].

The power consumption of a DBD can be determined in two different ways: One described by Grundmann [22] with the help of Lissajous figures, and a newly developed, direct method. Both have different advantages and disadvantages but yield the same results for a constantly sinusoidal voltage.

Lissajous figur method:

This method is described by Grundmann *et al.* in [36]. In order to calculate the power consumption, the charge and voltage measurements are plotted in a Q(t)-V(t) cyclogram. The trace of charge-voltage gives the so called Lissajous figure of the discharge. One example of such a figure is given in figure 5.2.

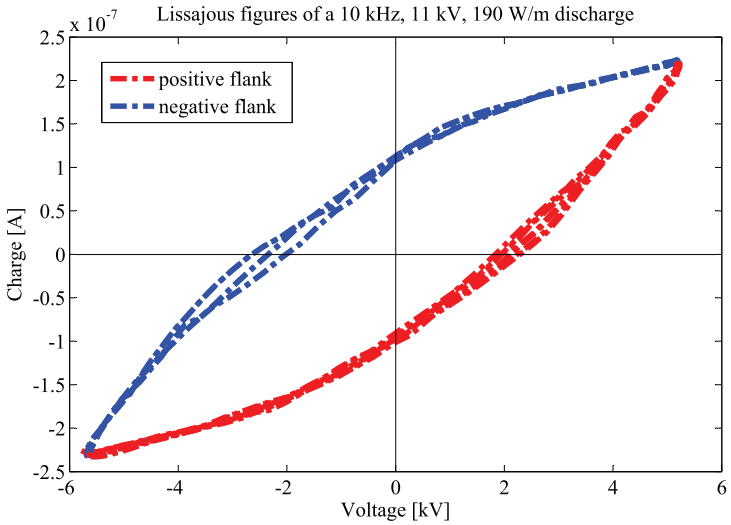

Figure 5.2: Lissajous figure of a sinusoidal voltage

The electrical energy E_k which is consumed per discharge-cycle is defined by the area enclosed by the cyclogram and can be calculated by

$$E_k = \oint_k C_p \cdot V_p(t) dV = \oint_k Q(t) dV \tag{5.3}$$

Subsequent multiplication of E_k with the voltage frequency f and averaging over K discharge-cycles leads to the consumed actuator power

$$P_A = Ef = \frac{f}{K} \sum_{k=1}^{K} E_k = \frac{f}{K} \sum_{k=1}^{K} \oint_k Q(t) dV \tag{5.4}$$

The yielded standard deviation of the calculated power corresponding to an measurement of K ≈ 800 cycles lies below 3% in all cases, according to Kriegseis [8].

The method is quite challenging in the post- processing, since the area enclosed in the cyclogram needs to be calculated. Commonly this is done by first smoothing the data with a Savitzky-Golay filters and afterwards fitting the path in the Lissajous figure for the positive and negative half-cycle separately. A polynomial fit is used for this purpose, with the fit-parameters giving rise to the enclosed area.

The main advantage of this method is the good insight into the physics of the discharge. The gradient of the Lissajous figur on the extremes, for instance, yield to the passive and effective capacitance of the Plasma actuator, C_0 and C_{eff}, respectively. Effective capacitances for both positive and negative half- cycles can be derived, as in Kriegseis [8]. Also, the Lissajous figures easily show a variance between different discharge cycles, like phase-shift or growth.

Direct method:

Within this work and following research, a newly method has been developed, originally in order to be able to determine the power consumption of a plasma actuator with a sinusoidal and pulsed high voltage. Since it yields a precision similar to Lissajous figure method, but requires significantly less post-processing time, it has soon been established in different fields.
The time- dependent electric power can be written as

$$P_{el}(t) = U(t) \cdot I(t). \tag{5.5}$$

With the help of I(t)=dQ(t)/dt it can be rewritten as

$$P_{el}(t) = U(t) \cdot I(t) = U(t) \cdot \frac{dQ(t)}{dt} \tag{5.6}$$

For a set of discrete voltage and charge measurements with a sample rate of $1/\Delta t$, the equation can be formed to

$$P_i = U_i \cdot \frac{\Delta Q_i}{\Delta t}, \tag{5.7}$$

and with the help of the rectangle method

$$P_i = U_i \cdot \frac{Q_{i+1} - Q_{i-1}}{2\Delta t}, \tag{5.8}$$

Averaging the power over N samples gives the mean power

$$\overline{P_i} = \frac{1}{N} \sum_{i}^{N} U_i \cdot \frac{Q_{i+1} - Q_{i-1}}{2\Delta t}, \tag{5.9}$$

with $Q_i = C_{probe} \cdot U_{i,c}$, when C_{probe} is the capacitance of the probe capacitor and $U_{i,c}$ the voltage drop measured across it.

This equation holds for all time-dependent voltage-charge systems. This is different from the

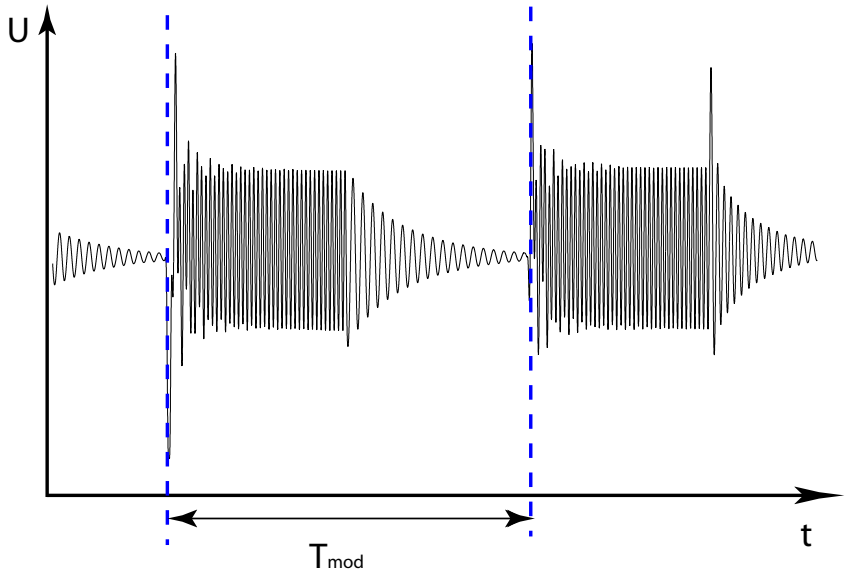

Figure 5.3: Pulsed sinusoidal high-voltage signal.

Lissajous figure method that is only valid for sinusoidal systems. For a sinusoidal system with voltage frequency f, the number of samples N has to be chosen such as $N \cdot \Delta t = K/f$, with K the number of cycles to average over ($K \in 1,2,3...$).
The method is of special use for puled sinusoidal high-voltage signals as in fig. 5.3. The sinusoidal base signal is varied with a modulation frequency $f_{mod} = 1/T_{mod}$, with T_{mod} being the modulation period. For a given time of the modulation period the high voltage generation is turned on, for the remaining time turned off. Since the generator is built out of inductors, capacitors and resistors, it forms an oscillating circuit. Thus the voltage does not vanish after turn-off; the sinusoidal signal is damped instead. The Lissajous figure corresponding to the damped oscillation can be seen in fig. 5.4.

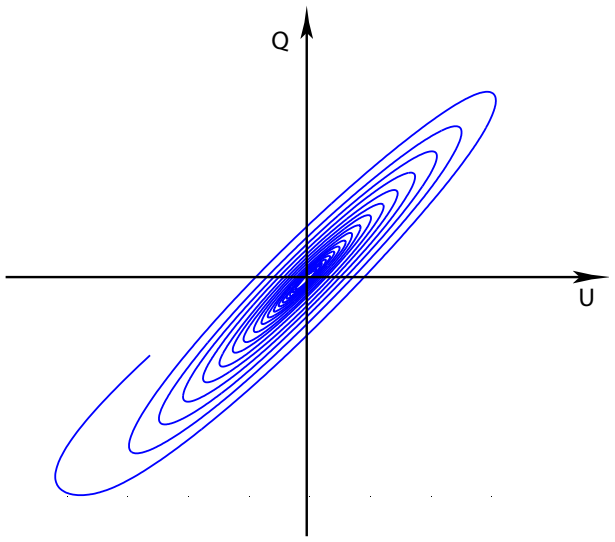

Figure 5.4: Lissajous figure of a damped sinusoidal voltage

Since the cyclogram is not closed, the power consumption cannot be determined with Lissajous figure method, since no area within the loop can be derived. This is the advantage of the direct method. The time- dependent power consumption of the damped oscillations can be seen in fig. 5.5.

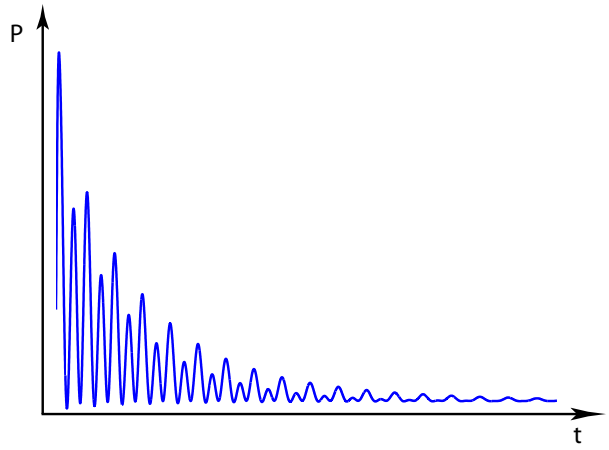

Figure 5.5: Power consumption of the damped system

The number of samples N to average the power over has to be chosen carefully. Dependent on it, the method can derive the mean power consumption of a duty cycle, the mean power consumption of a damped oscillation or average the power consumption over one modulation period.

One key benefit of the method besides the applicability for modulated signals is that it requires significantly less post-processing time, compared to the Lissajous figure method. The only required mathematical operations are addition and vector- multiplication, rather simple operations for modern computers. The Lissajous figure method uses polynominal fits and Savitzky-Golay filters, that require high calculation power. This benefit makes the direct method of special interest for *online monitoring*, where the power consumption of the actuator is controlled with a closed loop design (see Kriegseis [35]).

Comparison of the two methods

Figure 5.6 shows a direct comparison of the power calculated with both the direct and Lissajous figure method. The power levels were calculated with both methods from identical data. It is obvious that they match quite well. The deviation between the calculated power consumption is between 0.3% for low and 3% for high power levels.

This discrepancy is probably due to the fitting and smoothing in in the Lissajous figure method. These operations remove small variations in the data and thus change the determined power consumption by changing the calculated area enclosed in the cyclogram.
It cannot be said which method is the more accurate one, since they cannot be compared with other, more precise methods, since none have been developed. All in all, the direct method is applicable on a lager variety of measured data, and the post-processing complexity is significantly smaller.

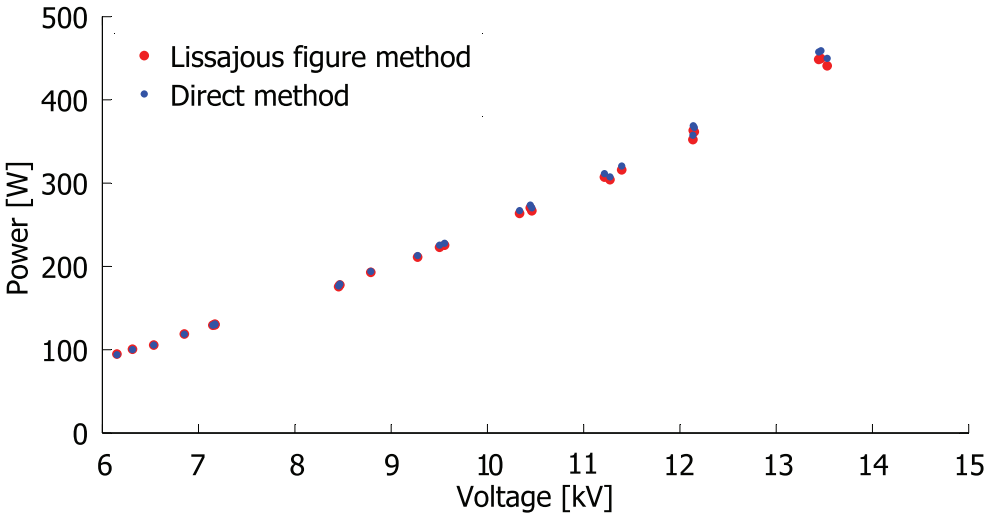

Figure 5.6: Comparison of the two methods of determining the power consumption of a DBD plasma actuator

Appendix B: Sorce code of the post-processing filter for discharge evaluation

```
function [PeakNumber,PeakAmp,DischargeLength]=countpeakss2(data,Threshold,Fs)
    %data:      vector with the current measurements
    %Threshold: positive scalar with the threshold of signal noise
    %Fs:        Frame rate of the measurement

    %Peaknumber:    Scalar of with the number of discharges in one cycle
    %PeakAmp:       Scalar with mean amplitude of discharge in one cycle
    %DischargeLength: Scalar with the elapsed time from the first to the last
    %                 discharge

    %Find all maxima and minima in the current above the threshold, with the
    %help of the program findpeakss
    %minimal distance to the next extremum 20 measurment data

    [negpeakloc,negpeakamp]=findpeakss(data,2,20,Threshold);
    [pospeakloc,pospeakamp]=findpeakss(data,1,20,Threshold);

    %For data without peaks above threshold: return zeros
    if length(pospeakamp)==0 | length(negpeakamp)==0
        PeakNumber=[0];
        PeakAmp=[0];
        DischargeLength=[0];
    else



    DischargeAmp=pospeakamp(1);
    DischargeLoc=pospeakloc(1);

    %Go through all maxima

    l=2;
    for k=2:length(pospeakloc)
        %Was the last extremum a minimum or maximum, where in the data
        %vetor is it?

        LastPos=pospeakloc(k-1);
        LastNeg=find(negpeakamp<pospeakloc(k-1),1,'last');
        if LastPos>LastNeg
            Last=LastPos;
        else
            Last=LastNeg;
        end

    %Was the last maximum smaller? (Criterion (b)) If yes, it was a discharge
        if pospeakamp(k)> (pospeakamp(k-1))*1.25

            DischargeAmp(l)=pospeakamp(k);
            DischargeLoc(l)=pospeakloc(k);
```

```
            l=l+1;
        %If not, was the last absolute value of the last extremum greater than
        %the maximum? (Criterion (a)) Is yes, it was a dicharge
            else
                if pospeakloc(k)>Last+75
                DischargeAmp(l)=pospeakamp(k);
                DischargeLoc(l)=pospeakloc(k);
                l=l+1;
                end
            end
        end
        %Return the mean amplitude, Number of peaks and elapst time between
        %first and last dicharge
    PeakNumber=l;
    PeakAmp=mean(DischargeAmp);
    DischargeLength=(DischargeLoc(end)-DischargeLoc(1))/Fs;
        end
```

Appendix C: High-speed streak camera image of the discharge in streamwise direction

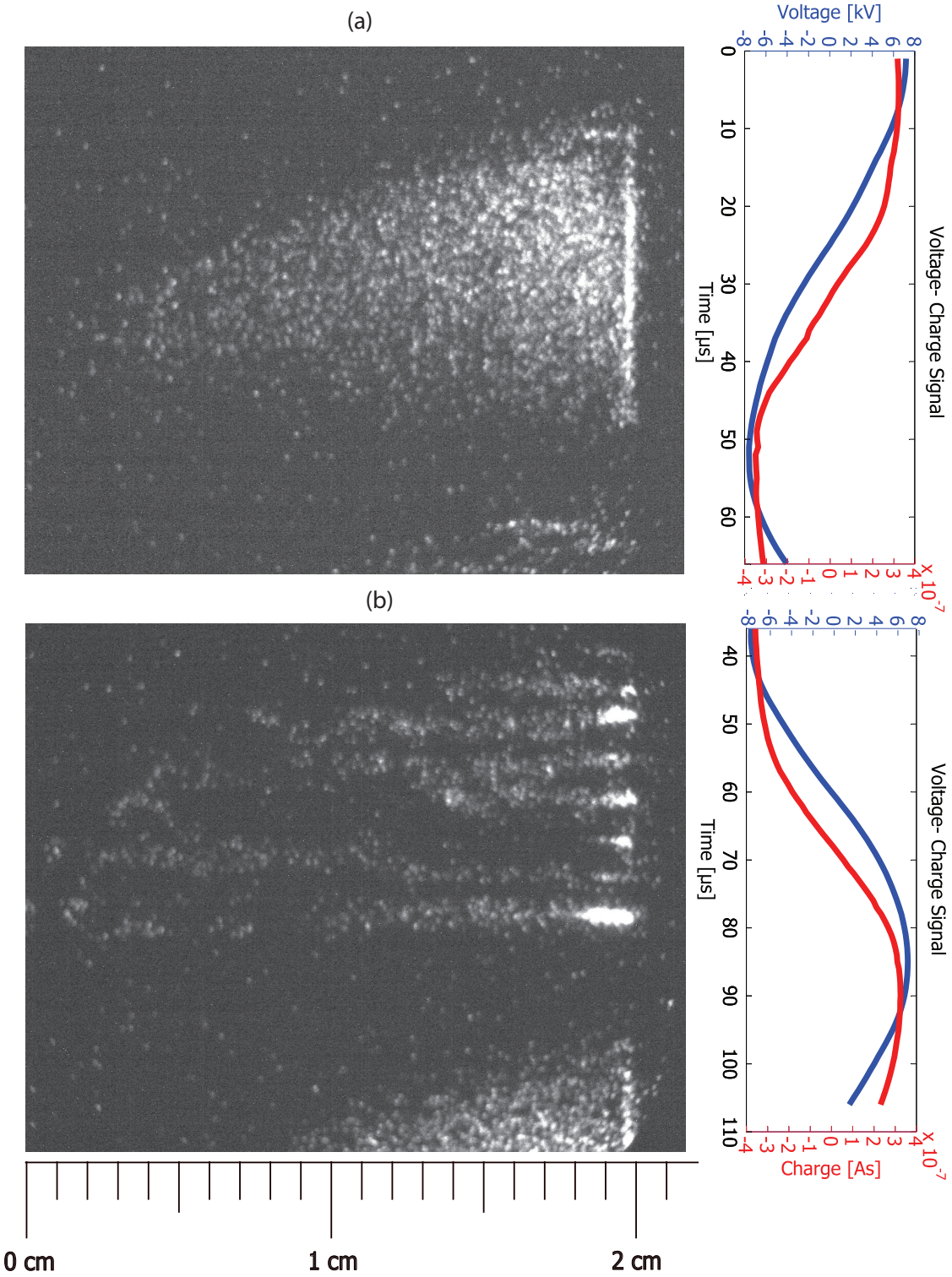

Figure 5.7: Streak camera image of the discharge, slot streamwise. The frequency was 10 kHz, the power consumption 440 Watt. The streak- time is 100 μs, corresponding to an effective streak time of 70 μs. (a) negative discharge in presumably pseudo- glow/corona regime (b) positive discharge in presumably streamer regime.

Appendix D: Single sided amplitude spectrum and power-spectral density

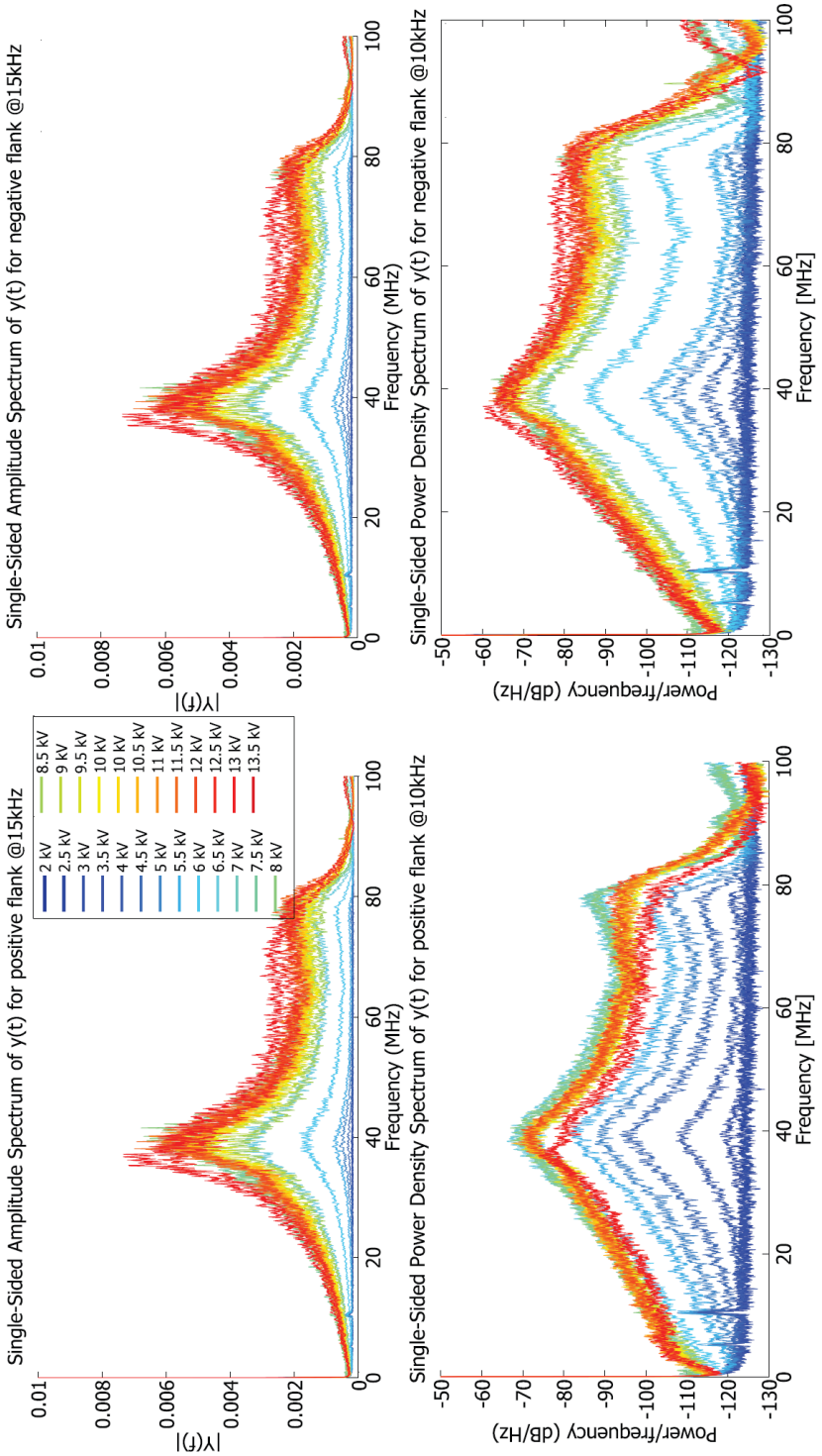

Figure 5.8: Single sided amplitude spectrum (top) and power spectral density (bottom) of the positive (left) and negative (right) discharge at a frequency of 15 kHz and exemplaric voltages between 2 and 13.5 kV.

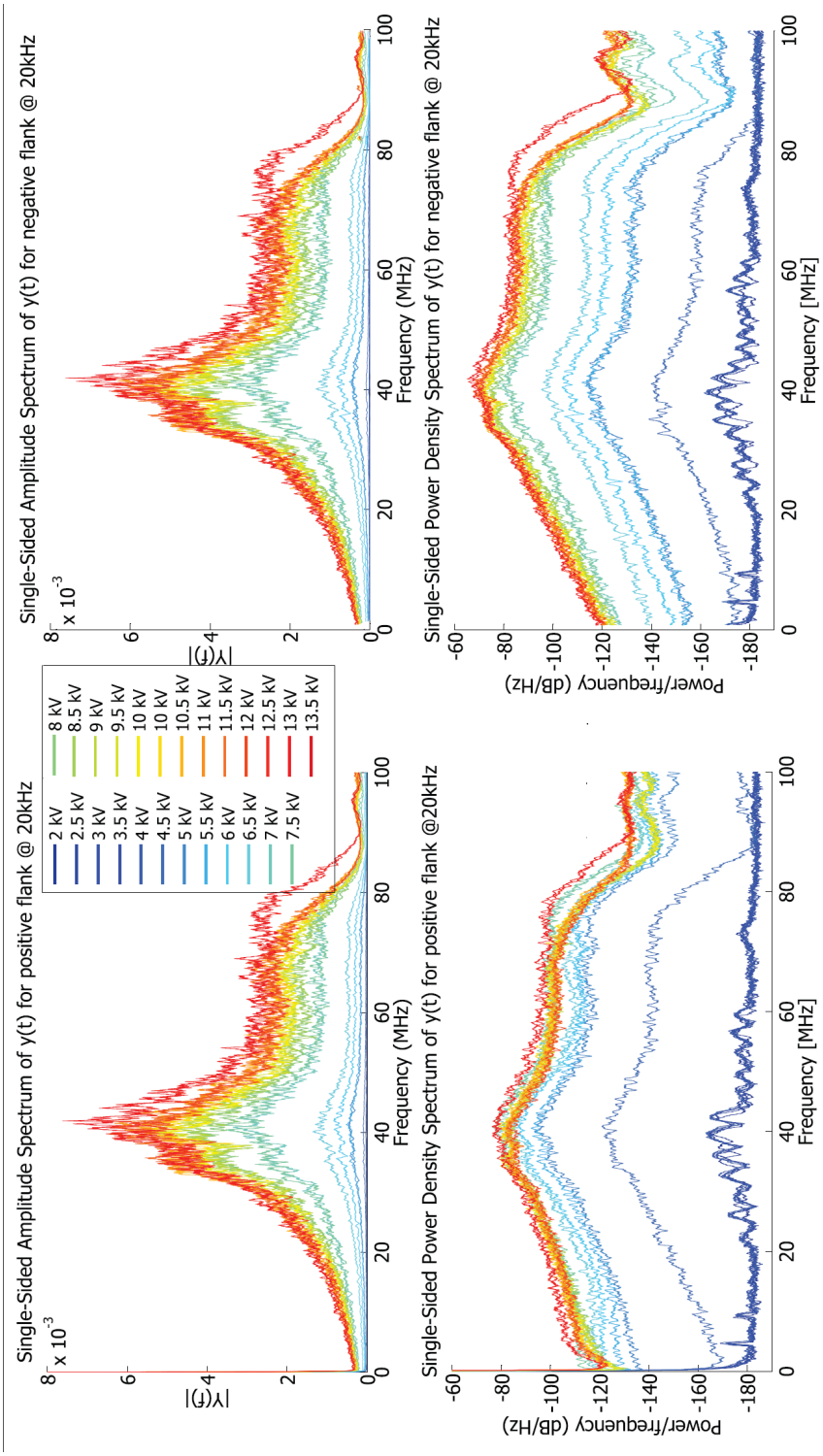

Figure 5.9: Single sided amplitude spectrum (top) and power spectral density (bottom) of the positive (left) and negative (right) discharge at a frequency of 20 kHz and exemplaric voltages between 2 and 13.5 kV.